Searching for Rare and Forbidden Exclusive Higgs Boson Decays with the ATLAS Detector

G. S. Virdee

Thesis submitted for the degree of Doctor of Philosophy

Particle Physics Group,
School of Physics and Astronomy,
University of Birmingham.

March 26, 2022

ABSTRACT

Searches for Higgs and Z bosons decaying to an ω meson and a photon, and for Higgs bosons decaying to a K^* and a photon are discussed using proton collision data recorded by the ATLAS experiment at $\sqrt{s} = 13$ TeV between 2016 and 2018. The observed events are consistent with the expected background. The obtained 95% confidence level upper limit on the branching ratio for the $H \to \omega\gamma$ decay using 89.5 fb^{-1} of data is 1.0 $\times 10^{-4}$ assuming a Standard Model Higgs Boson production. The analogous limit obtained for the $Z \to \omega\gamma$ decay is 3.5 $\times 10^{-7}$. The obtained upper limit for the $H \to K^*\gamma$ decay is 8.9 $\times 10^{-5}$, using 134 fb^{-1} of data. The search for $H \to K^*\gamma$ represents the first search for a flavour-violating exclusive decay of the Higgs boson.

DECLARATION OF AUTHORS CONTRIBUTION

This thesis represents work which the author has undertaken during post-graduate studies, which has built upon the considerable and continued efforts of the many scientists, engineers and technical staff within the CERN community.

Chapters 1 and 2 detail the relevant background and context of the work for this thesis from a theoretical perspective.

Chapter 3 is a description of the experimental background for the work presented.

Chapter 4 details the validation of τ-lepton triggers in the High Level Trigger, which was largely the work of the author, with support given from the members of the τ-trigger working group. The initial development stages of the machine learning algorithms development were done in collaboration with members of the τ working group, and the work presented is largely that of the author, and any subsequent work has been built on with the continued efforts of others within the collaboration.

Chapters 5 and 6 detail the the searches for $H/Z \to \omega\gamma$ and $H \to K^*\gamma$. For these analyses, the author worked in a small analysis group from the University of Birmingham, with significant collaboration. The author's work built upon the tools developed by the analysis team, and benefited enormously from the guidance and support of the analysis team. The work presented is largely the work of the author - including the analysis selection optimisations, the background modelling, statistical analysis and systematic uncertainties. A considerable body of work, both technical and otherwise, has been built by the analysis teams working on the decays of the Higgs and Z bosons to a meson and a photon, and work done by the author benefitted enormously from this.

During data-taking operations in 2018, the author undertook Data Quality mon-

itoring shifts during multiple runs, corresponding to part of the data used in the analyses presented in this thesis. As well as this, the author was the on-call expert for the Tau Trigger group for a short period, with the responsibility of ensuring the correct functioning and output of the Tau trigger subsystems.

Dedicated to my family, for all the love

"I knew exactly what to do.
But in a much more real sense, I had no idea what to do."
- Michael Scott

ACKNOWLEDGEMENTS

I did not expect writing these acknowledgements to be such a deep reflection on the journey of completing this PhD. It is a running joke with those that know me that I struggle to summon up sentimental words when prompted, however I will give it my best effort, as there are far too many people to thank for all of the support during the last four(+) years. A dedication for each of you separately is probably worthwhile, however it would likely make me surpass the word limit for this document so I will have to keep it brief.

I would firstly like to thank the ERC for the funding and financial support given, without which my PhD would not have been possible.

I must thank deeply all the members of my analysis team, past and present, notably Kostas, Andy, and Rhys. Not only have they been a constant guiding hand throughout the PhD, they have demonstrated considerable patience, and the vast body of my work has built upon the foundations which they have put in place. Considerable thanks must go also to Kostas and Andy, who took on the role of supervising me, and all that entails. I have known Kostas since the early days of my master's degree, and his expertise and guidance through my work has always been a driving force, for which I am indebted to him. Not only this, but I thank him for all the opportunities he made available for me since the very beginning. As for Andy, I cannot describe adequately the mountain of support he's provided me with, and his astounding ability to deal with an unrelenting barrage of questions and concerns. His patience and reassurance have always been a welcome presence and an inspiration, and I thank him for that deeply. I would also like to thank all those members of staff, both at the University of Birmingham and at CERN, who have assisted me during the PhD.

As for those with whom I have shared an office (or a zoom room, or indeed a

building), I would like to extend many thanks for being what I could only describe as an “entertaining source of productivity” - Jamés, Andy, Al, Tim, Briglin, Kendrick, Elliot, Jack, Russell, Rob V, Daniel, Nandish, Robbie, Jon P, Patrick, Rob W, Júlia, and Jon M, thank you all. Particular thanks go to Jamés and Andy, who somehow managed to handle finishing their studies and also bestowing upon us the collective wisdom of generations of PhD students that have come before, in both productive and non-productive ways, both of which I consider “sweet techniques” to this day.

It would not be right if I didn’t dedicate a paragraph to the two closest friends I have had the pleasure of knowing through this PhD - Nandish and Daniel. Nandish, Crispy, it’s been almost a decade that I’ve known you, and I have to extend my thanks for being a brother to me through all the years, and for putting up with my endless spouting of questionable jokes with your light-hearted nature. Daniel, thank you for being a devoted and loving work-wife since the day we met, and for helping create a unique and special space to express ourselves. I look forward to being made fun of for this sentimental display.

To all those friends outside of the PhD who have given me their endless support and love throughout this journey, whose names are too many to mention, I thank you all. The memories we’ve made through this time will stay with me forever.

To my family - Mum, Dad, Serina, Priya, Hena, Vinesh, Krishan and Dylan, for having seen me through all the good times and bad with never-ending love and support. This thesis and all the work I have done so far is dedicated to you all and I have endless gratitude and love for you in my life.

Contents

List of Tables

List of Figures

DEFINITIONS OF ACRONYMS

ALICE A Large Ion Collider Experiment

AOD Analysis Object Data

ATLAS A Toroidal LHC ApparatuS

BDT Boosted Decision Tree

BEH Brout-Englert-Higgs

BR Branching Ratio

BSM Beyond the Standard Model

CERN European Organisation for Nuclear Research

CL Confidence Level

CMS Compact Muon Solenoid

CP Combined Performance

CR Control Region

CSC Cathode Strip Chambers

CT Conversion Tracks

ECAL Electromagnetic Calorimeter

EM Electromagnetic

FT Fake Tracks

GR Generation Region

HCAL Hadronic Calorimeter

HL-LHC High Luminosity Large Hadron Collider

HLT High Level Trigger

IBL Insertable Beam Layer

ID Inner Detector

IP Interaction Point

IT Isolation Tracks

KDE Kernel Density Estimate

L1 Level 1

LAr Liquid Argon

LC Local hadron Calibration

LEP Large Electron-Positron Collider

LHC Large Hadron Collider

LHCb Large Hadron Collider beauty

LINAC LINear ACcelerator

LO Leading Order

LSTM Long Short-Term Memory

MC Monte Carlo

MDT Monitored Drift Tube

MFV Minimal Flavour Violation

MS Muon Spectrometer

MVA MultiVariate Analysis

NLO Next-to-leading Order

NNLO Next-to-next-to-leading Order

NP Nuisance Parameter

PDF Parton Distribution Function

PDF Probability Density Function

PS Parton Shower

PS Proton Synchrotron

PSB Proton Synchrotron Booster

QCD Quantum Chromodynamics

QED Quantum Electrodynamics

QFT Quantum Field Theory

RF Radio Frequency

RNN Recurrent Neural Network

RoI Region of Interest

RPC Resistive Plate Chambers

SCT SemiConductor Tracker

SM Standard Model

SPS Super Proton Synchrotron

SR Signal Region

TDAQ Trigger and Data Acquisition

TES Tau Energy Scale

TGC Thin Gap Chambers

TRT Transition Radiation Tracker

TT Tau Tracks

VR Validation Region

CHAPTER 1

Introduction

The challenge of producing a mathematical framework that is complete and robust enough to accurately describe the subatomic universe is no small feat. However, the drive of theoretical and experimental physicists has been sufficient to tackle this challenge, culminating in the Standard Model (SM) of particle physics. Comprising of three of the four fundamental forces, and listing all elementary particles, the SM is robust and complete enough to withstand decades of experimental testing. The SM describes the elementary particles that constitute matter, and the forces (excluding gravity) that dictate the interactions between them. The SM states that matter is composed of elementary spin-$\frac{1}{2}$ fermions, whose interactions are mediated by bosons of integral spin. The electromagnetic (EM), weak and strong forces are mediated by the photon (γ), $W^{\pm}/Z^0$ and gluons (g) respectively. Additionally, a scalar particle named the Higgs boson provides the masses of the elementary particles and sheds light on the separation between the EM and weak forces. Further classifying elementary fermions leads to quarks and leptons. Quarks are able to interact through

all fundamental interactions, whereas leptons do not interact through the strong force due to a lack of 'colour' charge. There are three generations of leptons and quarks. Left-handed fermion fields take the form of isospin doublets, whereas the right-handed fields take the form of isospin singlets. For the quarks this takes the form of an up- and down- type quark per generation, and for the leptons a charged lepton and a neutrino. A representation of the SM, including the various properties of the elementary particles, is shown in Tables 1.1 and 1.2.

Fermion	Approximate mass (MeV/c^2)	EM Charge (e)
u	2.4	+2/3
d	4.8	-1/3
c	1.27×10^3	+2/3
s	96	-1/3
t	173.1×10^3	+2/3
b	4.2×10^3	-1/3
e	0.511	-1
ν_e	$<2.2\times10^{-6}$	0
μ	106	-1
ν_μ	$<1.7\times10^{-1}$	0
τ	1.77×10^3	-1
ν_τ	<15.5	0

Table 1.1: Summary of the fermions in the Standard Model [1].

Boson	Mass (GeV/c^2)	Field
γ	Massless	EM
$W^\pm$, Z^0	80.379 ± 0.012, 91.188 ± 0.002	Weak
g	Massless	Strong
H	125.09 ± 0.21(stat.) ± 0.11(syst.)	Higgs

Table 1.2: Summary of the bosons in the Standard Model [1].

Quantum field theory is the basis of the SM, describing the nature of the particles and their interactions using gauge fields. These gauge fields must obey invariance under sets of transformations known as symmetry groups, where each group has an associated conserved quantity. Introducing the Lagrangian formalism allows one to capture the dynamics of a gauge field. For example, a Lagrangian can take the form:

$$\mathcal{L} = \mathcal{L}_{kin} + \mathcal{L}_{mass} + \mathcal{L}_{int} \tag{1.1}$$

where the three terms describe the kinematics, mass, and interactions respectively within the gauge field.

To describe the manifestation of the Higgs boson, we must look at electroweak theory [20][21] and spontaneous symmetry breaking. Electroweak theory treats the electromagnetic and weak forces as aspects of the same underlying force. This is achieved by requiring invariance under the $SU(2)_L \times U(1)_Y$ group of local gauge transformations. However, this regime predicts that the gauge bosons responsible for propagating the forces for weak interactions should be massless (corresponding to a lack of quadratic terms of the gauge fields in the Lagrangian), which disagrees with measurements showing relatively massive propagators. The gauge bosons corresponding to these groups are the W_1, W_2 and W_3 bosons from the $SU(2)$ group, and the B boson of the $U(1)$ group. Simply adding a mass term to the Lagrangian would break gauge invariance. To rectify this, the symmetry must be spontaneously broken - this is achieved through the Brout-Englert-Higgs mechanism (see Section 2.1).

Although proven to have great strengths in predicting the structure of the subatomic world, for example the discovery of the Higgs boson in 2012 [22][23], the SM leaves many unanswered questions. These include the nature of dark matter, the neutrino mass problem, and the matter/antimatter asymmetry in the universe, as well as not incorporating gravity. These unanswered questions lie at the heart of current particle physics endeavours - the most prominent of which is the Large Hadron Collider (LHC) [24].

The LHC creates unprecedented centre-of-mass energies at the highest instantaneous luminosity attained thus far in hadron colliders. At the time of writing this thesis, the LHC is in the midst of upgrades to improve performance in-between data taking periods, known as Run-2 and Run-3.

The material presented in this thesis represents work undertaken within the context of the ATLAS experiment during 2016-2018 data taking. The work takes the form firstly of developing some of the necessary tools for the triggers used to collect the data within ATLAS relevant to the analyses performed, and secondly the analyses themselves.

Rare Higgs boson decays to light mesons and quarkonium ($q\bar{q}$) states may provide a window into the Higgs boson couplings to light quarks ($Hq\bar{q}$). There are currently very few experimental constraints for these couplings. Chapters 2 and 3 lay out the theoretical, phenomenological and experimental background necessary to provide context to the studies of these decays.

In order to perform these measurements, tools must be developed in order to distinguish the unique signatures left behind by the different species of particles in the ATLAS detector. An example of this is the High Level Trigger (HLT), which utilises fast-computing algorithms to identify particle topologies. This falls under the overall trigger system, which aims to collect interesting events. The searches for rare Higgs boson decays to a meson and a photon use modified versions of the algorithms used for τ-lepton identification, and the connection between them must be understood. Chapter 4 describes the validation of the algorithms used to identify τ-lepton decays during Run-2, which are exploited in many physics searches and measurements (including for the searches presented in this thesis).

Chapters 5 and 6 describe in detail the analyses searching for the decays $H \to K^*\gamma$ and $H/Z \to \omega\gamma$ respectively. This includes the event selection strategy, background modelling, systematic uncertainties, statistical treatment and finally the results.

Chapter 7 summarises the material presented in the thesis, and provides commentary on future prospects.

CHAPTER 2

The Standard Model and the Higgs Boson

This chapter provides the theoretical and phenomenological background needed to understand the searches for the rare exclusive decays of the Higgs boson to a meson and a photon. Kinematic studies for a wide range of rare exclusive Higgs and Z boson decays are also discussed.

Measurement of the Higgs boson couplings to the three generations of quarks is a key test of the Standard Model, however direct evidence only exists for the third generation of quarks (t, b) [25, 26, 27, 28]. In order to measure the coupling of the Higgs boson to the first and second generation of quarks, the production of quarkonium $(q\overline{q})$ states can be examined in the decays of Higgs bosons. The following section describes the theory, current status, and next steps for searches for the Higgs boson to light quarkonium states, which are complementary to direct searches such as $H \to c\overline{c}$ [29], where jet charm tagging techniques are employed.

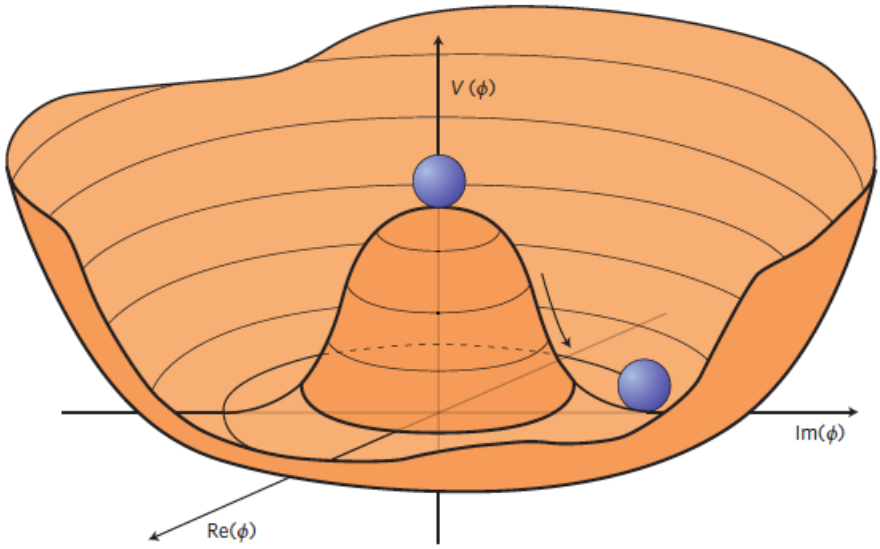

Figure 2.1: Depiction of the Higgs field potential for $\mu^2 < 0$ [7].

2.1 Brout-Englert-Higgs mechanism

The Brout-Englert-Higgs (BEH) mechanism [30, 31, 32, 33] describes the procedure to spontaneously break the symmetry of the electroweak Lagrangian. We can identify the terms of (1.1) in an electroweak context as

$$\mathcal{L}_{\mathcal{EW}} = \mathcal{L}_{ferm} + \mathcal{L}_{Higgs} + \mathcal{L}_{Yuk} \tag{2.1}$$

which corresponds to the fermion/gauge term, the mass term arising from the Higgs mechanism, and interaction term arising from the Yukawa couplings (see section 2.2). The Higgs mechanism requires an additional $SU(2)_L$ isospin doublet corresponding to complex scalar fields, with $Y = 1$ (defined as the hypercharge),

$$\phi = \begin{pmatrix} \phi^+ \\ \phi^0 \end{pmatrix} \tag{2.2}$$

where the contribution to the Lagrangian (2.1) is,

$$\mathcal{L}_{Higgs} = (D_\mu \phi)^\dagger (D^\mu \phi) - V(\phi) \tag{2.3}$$

where the potential is identified as,

$$V(\phi) = \mu^2\phi^2 + \lambda\phi^4 \tag{2.4}$$

and μ is the mass parameter, giving the "Mexican Hat" potential shown in Figure 2.1. . By minimising this potential, we identify that the minimum of the potential $\phi_{min} = \sqrt{\frac{-\mu^2}{2\lambda}}$ for $\mu^2 < 0$ This leads to a vacuum choice:

$$\phi = \frac{1}{\sqrt{2}} \begin{pmatrix} 0 \\ v + h \end{pmatrix} \tag{2.5}$$

The value of the minimum of the potential is the vacuum expectation value (v) - the result of the Higgs mechanism is that for $\mu^2 < 0$, v is non-zero, spontaneously breaking the $SU(2)_L$ symmetry while providing an invariant Lagrangian under the $SU(2)_L \times U(1)_Y$ group of transformations. This is known as spontaneous symmetry breaking. The SM Higgs field as a complex doublet contains 4 degrees of freedom - 3 of which are needed to provide mass to the 3 massive gauge bosons, with the final degree of freedom giving rise to the Higgs boson. This produces massive gauge bosons corresponding to the $W^{\pm}/Z^0$ bosons from the breaking of the symmetry, and fixes the original issue of predicted massless gauge bosons. The physical scalar Higgs field can be identified as h, with the associated particle being the Higgs boson. The W_3 and B bosons previously mentioned mix to form the Z^0 boson and the photon,

$$\begin{pmatrix} \gamma \\ Z^0 \end{pmatrix} = \begin{pmatrix} \cos\theta_W & \sin\theta_W \\ -\sin\theta_W & \cos\theta_W \end{pmatrix} \begin{pmatrix} B \\ W_3 \end{pmatrix} \tag{2.6}$$

where θ_W is the weak mixing angle. The W_1 and W_2 bosons also combine to produce the $W^{\pm}$ bosons,

$$W^{\pm} = \frac{1}{\sqrt{2}} (W_1 \mp iW_2) \tag{2.7}$$

and the Higgs boson to vector boson couplings depend on the square of the boson mass,

$$g_{HVV} = \frac{2m_V^2}{\nu}, \tag{2.8}$$

2.2 Fermion mass generation

The BEH mechanism can explain the origin of massive gauge boson propagators through the manifestation of the Higgs boson, however there is no explicit explanation for the masses of fermions. The Yukawa mechanism introduces a solution, in the form of fermion mass terms in the Lagrangian that obey gauge invariance. The complex doublet in Eqn. 2.2 forms an $SU(2)_L \times U(1)_Y$ singlet as $-\lambda_f \bar{\psi}_L \phi \psi_R$ in the Lagrangian. λ_f is the Yukawa coupling of the Higgs boson to the fermion. This term results in a series of couplings in the SM, $g_{Hf\bar{f}}$, which are linearly dependent on the mass of the fermion.

$$g_{Hf\bar{f}} = \frac{m_f}{\nu}, \tag{2.9}$$

The values of the Yukawa couplings for quarks can vary substantially for models that are beyond the SM (BSM).

2.3 Higgs boson properties

Following the Higgs boson discovery measuring the properties of the Higgs boson is one of the main goals for the LHC, and many results have been published to date. Before discussing the measurements, the production and decay modes of the Higgs boson in the LHC are summarised.

There are various production modes for the Higgs boson at the LHC [10]. The dominant production modes at the $\sqrt{s}$ used in these analyses are gluon-gluon fusion (ggH) ($\sim$ 87%), vector boson fusion (VBF)($\sim$ 7%), associated production with a vector boson ($\sim$ 4%), and quark associated production ($\sim$ 2%). The Feynman diagrams for these processes are shown in Fig 2.2.

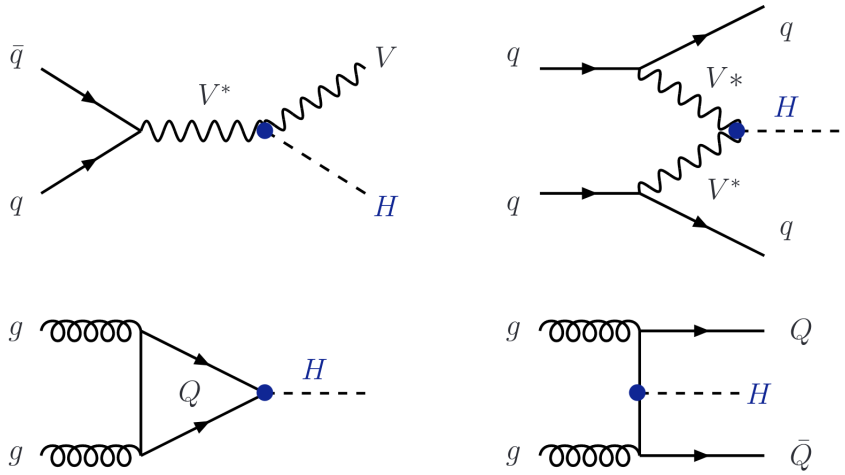

Figure 2.2: Feynman diagrams for the main Higgs boson production processes at the LHC. (a) gluon-gluon fusion, (b) vector boson fusion, (c) associated production with a vector boson, (d) quark associated production. Figure from Ref. [8].

ATLAS measured the total cross section for the production of a Higgs boson inclusive of all production modes from pp collisions to be $55.5^{+4.0}_{-3.8}$pb [34] at $\sqrt{s}$ = 13 TeV using 139 fb^{-1} of data, consistent with the SM prediction. The measurement of the cross section for the production of a Higgs boson [9] from pp collisions split into different production modes is shown in Figure 2.3, using between 24.5 - 139 fb^{-1} of data.

The mass of the Higgs boson was measured in ATLAS through the channels $H \rightarrow ZZ^* \rightarrow 4\ell$ and $H \rightarrow \gamma\gamma$. The value measured through a simultaneous fit to both channels was m_H = 124.97 $\pm$ 0.19(stat.) $\pm$ 0.13(syst.) GeV [35]. CMS also performed measurements of the cross section and mass using these channels [36][37]. The combined measurement for the mass of the Higgs boson from ATLAS and CMS using the $\sqrt{s}$ = 7 TeV and $\sqrt{s}$ = 8 TeV data is m_H = 125.09 $\pm$ 0.21(stat.) $\pm$ 0.11(syst.) GeV [38].

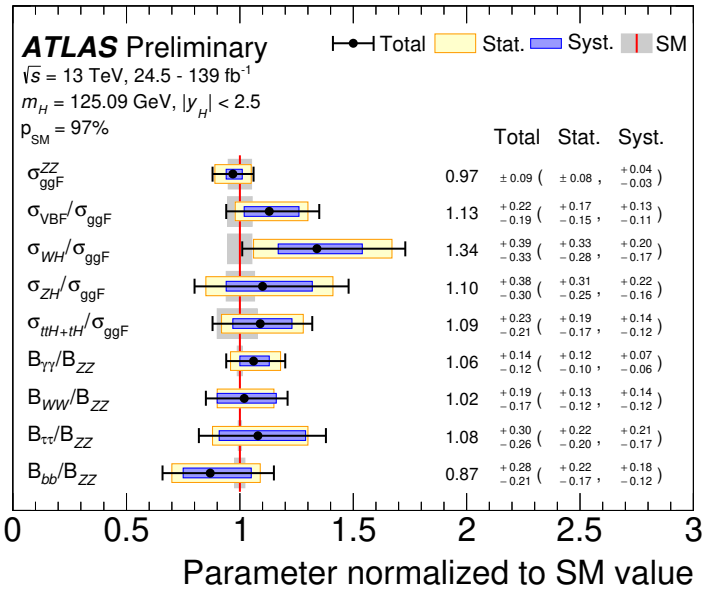

Figure 2.3: Cross sections for the ggF, VBF, WH, ZH and ttH+tH production modes normalized to SM predictions, measured assuming SM values for the decay branching fractions. The black error bars, blue boxes and yellow boxes show the total, systematic, and statistical uncertainties in the measurements, respectively. The gray bands indicate the theory uncertainties in the SM cross-section predictions. Figure from Ref. [9].

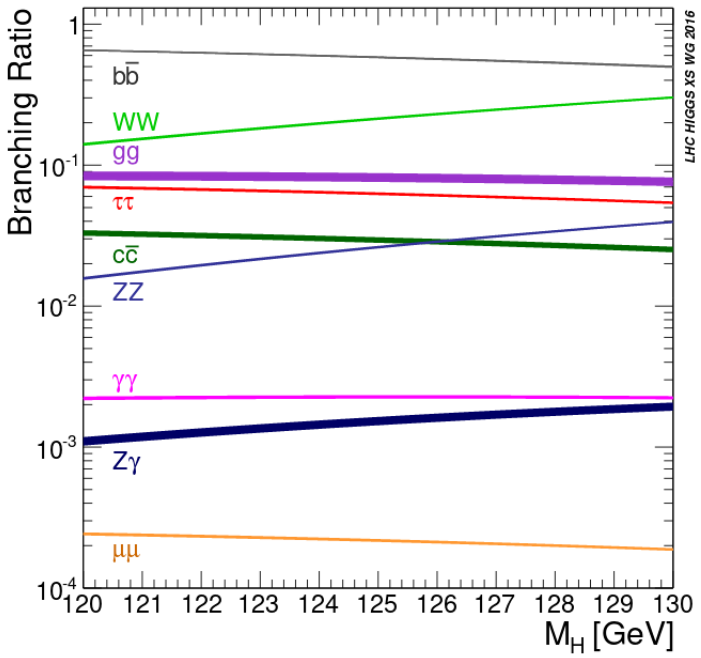

Figure 2.4: Branching ratios for the decays of the Higgs boson for a selected mass range around 125 GeV. Figure from Ref. [10].

There are also various decay modes for the Higgs boson, summarised in Fig 2.4. The measurement of the Higgs decay to other bosons has been measured to be consistent with SM predictions, and will not be discussed here. The decays to fermions are more directly relevant, and take place through a different mechanism. There is experimental evidence for the decay of the Higgs boson to the third generation of fermions, namely $H \to \tau^+\tau^-$ [39][40], $H \to t\bar{t}$ [25][26] and $H \to b\bar{b}$ [27][28]. Evidence for the Higgs boson decay to $\mu\mu$ has also been observed using both the ATLAS and CMS detectors [41, 42]. A direct search with ATLAS has been performed for $H \to c\bar{c}$ [29, 43, 44].

2.4 New physics in Higgs boson couplings to fermions

Deviations in the quark Yukawa couplings from the SM expected values can substantially increase the branching fractions for exclusive radiative Higgs boson decays. Many BSM theories propose such modifications - a few examples are provided below.

The Higgs-dependent Yukawa couplings model [11], for example, suggests the possibility that the Yukawa couplings are a function of the Higgs field, whereby the fermion mass hierarchy is generated through powers of the Higgs vacuum expectation value - this leads to modifications to the branching ratios of Higgs boson decays visible at the TeV scale, in particular for the couplings to lighter quarks (the couplings to the weak gauge boson and to the top quark remain as the SM expected values). Such modifications also allow for flavour violating Higgs couplings. Effects on the branching ratios of Higgs boson decays from certain potential modifications are shown in figures 2.5 and 2.6, showing the effect on the Yukawa couplings and on flavour-violating decays, respectively.

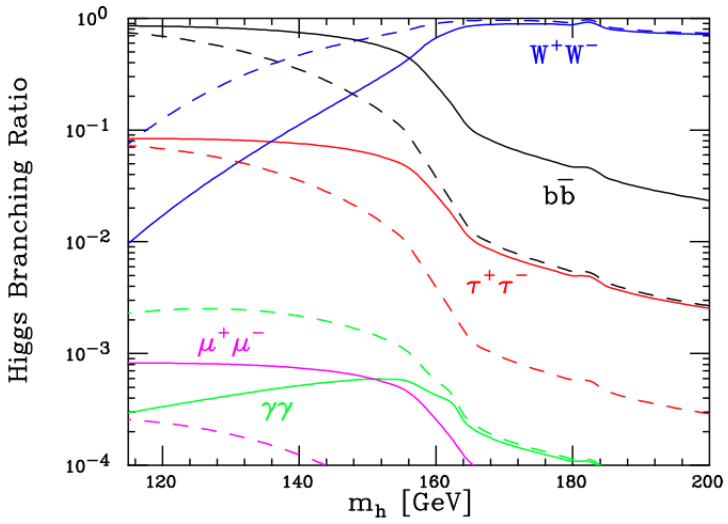

Figure 2.5: Higgs branching ratios for different decay modes for the Higgs-dependent Yukawa couplings model (solid), and for the SM predicted values (dashed). [11]

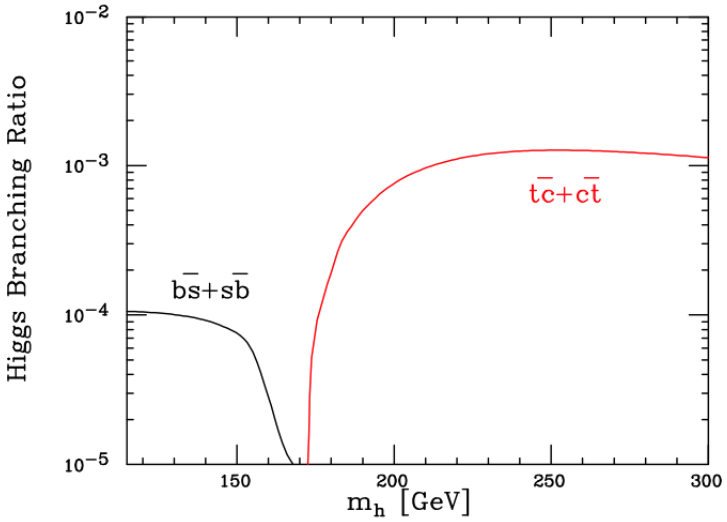

Figure 2.6: Higgs branching ratios for flavour-violating decay modes for the Higgs-dependent Yukawa couplings model (solid). [11]

The Randall-Sundrum models [45] provide an alternative approach to solving the hierarchy problem between the weak scale and the Planck scale, by introducing a single additional dimension, with profound experimental consequences. These include fundamental spin-2 excitations with weak-scale order mass, coupled to the SM particles through the weak scale as opposed to the gravitational strength of the particles - as an experimental consequence, it also allows for flavour violation at LHC energies, and thus is relevant to these searches.

The Minimal Flavour Violation (MFV) framework [46] takes an effective-field theory approach to explaining the minimally-flavour violating effects in flavour physics. If the effective theory starts from the SM with the modification of a Higgs sector containing two scalar doublets, then significant increases in the Yukawa couplings allow for flavour-violating operators to be constructed. These have implications for the neutral and charged currents coupled to the Higgs boson.

The Froggatt-Nielsen mechanism [47] proposes a scalar field which breaks the $U(1)$ symmetry to explain the mass and mixing hierarchies, which has direct implications for the Higgs couplings to the quarks if the Higgs field itself is assumed to be the scalar field. This would modify the decay branching ratios of the Higgs boson, including the rare decays presented in this thesis.

As a final example, there is possibility of the Higgs boson being a composite pseudo-Nambu Goldstone boson [48], analogous to the nature of the pions or K-mesons in QCD - the corresponding broken global symmetry is a symmetry of a new strongly interacting sector from which the Higgs boson emerges as a composite boson. These proposals attempt to address the "naturalness" problem of the SM in relation to the hierarchy problem, allowing for a physical low-mass Higgs boson without significant fine-tuning. Currently, the most testable consequence of these proposals is the modification of the Higgs boson couplings to the other SM fields.

Given the variety of models that predict modifications to the Higgs boson Yukawa couplings, measuring the couplings experimentally is necessary to probe the param-

eter space for these models.

2.4.1 Experimental probes of light quark couplings to the Higgs boson

Measurements of the Higgs decays to b-, c- and lighter quarks directly are restricted by the dominating QCD background. Searches for exclusive rare decays of the Higgs boson into vector mesons and quarkonium states ($\mathcal{M}$) and associated photons provide a way to gain access to the Yukawa couplings. Two amplitudes contribute to the decays. The first, the "direct" amplitude, proceeds through the $H \to q\overline{q}$ coupling, followed by a photon emission before the quark hadronisation into the meson/quarkonium state. The second, "indirect" amplitude, proceeds via the H coupling followed by the fragmentation $\gamma^* \to V$. The two decays are shown in Figure 2.7. The decay topology of a high-p_T photon travelling back-to-back against the decay products of the meson provides a distinct signature to search for.

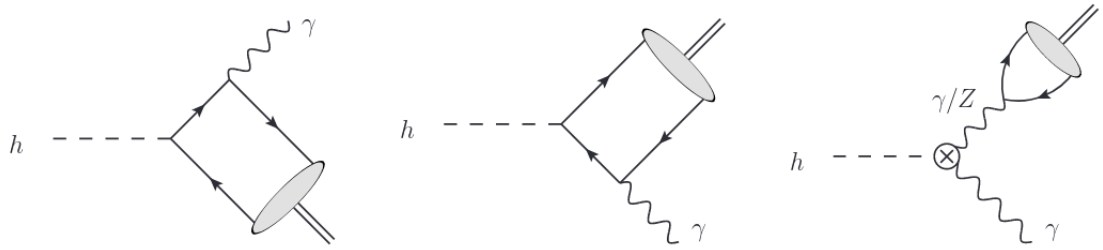

Figure 2.7: Direct contributions to the H$\to \mathcal{M}\gamma$ decay amplitude (left and center), and indirect contributions involving a one-loop correction (right) [3]

At the same time, the analogous exclusive decays of the abundantly produced Z bosons, are attracting interest [49, 2, 50], as they offer a novel and rich physics programme in precision quantum chromodynamics (QCD), electroweak physics, and physics beyond the SM. In precision QCD, these decays are a laboratory to study the QCD factorisation approach [2], since the power corrections in terms of the QCD energy scale over the vector boson mass are small. As a result, they provide a model-independent probe to the light-cone distribution amplitudes of hadrons.

A full list of the decays of interest, including final states, is shown in Table 2.1.

Higgs Boson decay channel	Z Boson decay channel
$H \to \psi(nS)\gamma \to \mu^+\mu^-\gamma$	$Z \to \psi(nS)\gamma \to \mu^+\mu^-\gamma$
$H \to \Upsilon(nS)\gamma \to \mu^+\mu^-\gamma$	$Z \to \Upsilon(nS)\gamma \to \mu^+\mu^-\gamma$
$H \to \rho\gamma \to \pi^+\pi^-\gamma$	$Z \to \rho\gamma \to \pi^+\pi^-\gamma$
$H \to \phi\gamma \to K^+K^-\gamma$	$Z \to \phi\gamma \to K^+K^-\gamma$
$H \to \omega\gamma \to \pi^+\pi^-\pi^0\gamma$	$Z \to \omega\gamma \to \pi^+\pi^-\pi^0\gamma$
$H \to K^{*0}\gamma \to K^+\pi^-\gamma$	$Z \to K^0_S\gamma \to \pi^+\pi^-\gamma$
$H \to D^{*0}\gamma \to D^0(K^-\pi^+)\pi^0\gamma$	$Z \to D^0\gamma \to K^-\pi^+\gamma$

Table 2.1: Decays of interest for both Higgs Boson decays and the analogous Z boson decays.

In addition to searches for $H/Z \to \mathcal{M}\gamma$, there are alternative probes to the first- and second-generation quark Yukawa couplings. Some examples are provided below.

The decay $H \to c\bar{c}$ can be searched for directly, and searches have already been performed with ATLAS and CMS [29, 43, 44]. The most stringent limit is set by the ATLAS analysis, which makes use of the full LHC Run-2 dataset collected, corresponding to an integrated luminosity of 139 fb^{-1}. The analysis exploits flavour-tagging algorithms to identify jets originating from the hadronisation of charm quarks. The search uses three channels, $ZH \to \nu\nu c\bar{c}$, $WH \to l\nu c\bar{c}$ and $ZH \to llc\bar{c}$. The analysis yields an observed limit of 26 times the predicted SM cross-section times branching fraction for a Higgs boson with a mass of 125 GeV decaying into a $c\bar{c}$ pair at the 95% confidence level.

The coupling of the Higgs boson to charm quarks can also be probed via Higgs production in association with a charm-tagged jet: $pp \to hc$ [51]. The reference details a first estimate showing that the Yukawa coupling to charm quarks could be determined at a level approaching the SM value in this channel, given 3 ab^{-1} of data collected at the LHC and sufficiently sophisticated b- and c-jet tagging algorithms.

The charge asymmetry in the $pp \to W^{\pm}H$ production mode is another potential probe of the light quark Yukawa couplings [52]. The LHC favours W^+H production over W^-H production, predominantly through the Higgsstrahlung process $qq' \to W^{\pm *} \to W^{\pm}H$. As an example, at the 14 TeV LHC, with m_H =125.09 GeV, $\sigma(W^+H)/\sigma(W^-H) = 1.56$. However, this inclusive charge asymmetry is signifi-

cantly changed if there are modifications to the SM light quark Yukawa couplings. The paper referenced motivates a measurement of the $W^{\pm}H$ charge asymmetry in the exclusive mode $W^{\pm}H \rightarrow (l^{\pm}\nu)(l^{\pm}\nu jj)$. There is a possibility to reach a $\approx 5\sigma$ significance in the individual ++ and - - final states with $300 fb^{-1}$ of 14 TeV LHC data, which when extrapolated to 3 ab^{-1} reaches a statistical precision of 0.4 % on the charge asymmetry. If the measured asymmetry shows deviation from the SM expectation, then a possible interpretation would be an enhanced SM light quark Yukawa coupling as well as additional new physics effect that preserve the consistency of the Higgs data with the SM expectation.

As a final example, the kinematics of the Higgs boson (in particular the $p_{\mathrm{T}}$and rapidity) can be used to constrain the values of the Yukawa couplings [53, 54]. It can be shown that the normalised p_{T} distribution of the Higgs boson or of jets recoiling against it provides a sensitive probe of the b, c and s Yukawa couplings. Given sufficient advances in the precision of Higgs + jets production calculations, and in the precision of experimental measurements, it is possible to obtain a limit of $\kappa_c \in [-0.6, 3.0]$ at the 95% CL at the HL-LHC, in a complementary fashion to the searches outlined above given the lack of dependence on the small signal rate nor on the performance of flavour tagging algorithms. For the strange Yukawa coupling, the sensitivity in the same environment is expected to be approximately 30 times the SM expectation.

2.5 Exclusive radiative decay search results

The following section summarises the current status of searches for exclusive radiative Higgs and Z boson decays to a meson and a photon with the ATLAS experiment [4, 5], including the resulting upper limits on the branching ratios, which have been compared to theoretical predictions [55, 3, 56, 57, 58, 59, 60]. Similar searches were performed with the CMS experiment [61, 62].

The observation of Higgs boson decays to the J/ψ, $\psi(2S)$ mesons would constrain

the Yukawa coupling to the charm quark, and the $\Upsilon(nS)$ decay would constrain the bottom quark Yukawa coupling. In these searches, the final states for the meson decays are $\mathcal{M} \to \mu^+\mu^-$, and they are performed using ATLAS data collected during 2015/2016 at $\sqrt{s} = 13$ TeV with $\mathcal{L} = 36.1$ fb^{-1}.

No significant excess of events are observed above the expected backgrounds in the searches. However, constraints on the branching fractions of the decays can be placed - the 95% confidence level upper limits are shown in Table 2.2. The results improve on a previous search performed [63]. The observation of Higgs boson decays to the ρ and ϕ mesons would constrain the Yukawa couplings to the up/down and strange quarks respectively. In these searches, the decays are searched for in the final states $\rho \to \pi^+\pi^-$ and $\phi \to K^+K^-$, and are performed using ATLAS data collected during 2015/2016 at $\sqrt{s} = 13$ TeV with $\mathcal{L} = 35.6$ fb^{-1}. At the time of these measurements, no other experimental information existed about the $H \to \rho\gamma$ decay channel, and the $H \to \phi\gamma$ 95% confidence level upper limit was significantly improved from a previous search [64].

	SM Expected Branching Ratio $\mathcal{B}$	
Meson $\mathcal{M}$	H	Z
J/ψ	$2.99^{+0.16}_{-0.15} \times 10^{-6}$	$8.96^{+1.51}_{-1.38} \times 10^{-8}$
$\psi(2S)$		
$\Upsilon(nS)$, n = 1,2,3	$(5.22^{+2.02}_{-1.70}, 1.42^{+0.72}_{-0.52}, 0.91^{+0.16}_{-0.15}) \times 10^{-9}$	(4.80,2.44,1.88) $\times 10^{-8}$
ϕ	(2.31±0.11) $\times 10^{-6}$	(1.04±0.12) $\times 10^{-8}$
ρ	(1.68±0.08) $\times 10^{-5}$	(4.19±0.47) $\times 10^{-8}$
ω	(1.48±0.08) $\times 10^{-6}$	(2.82±0.40) $\times 10^{-8}$
K^*		
	95% CL upper limit on branching ratio $\mathcal{B}$	
J/ψ	2.1×10^{-4}	1.2×10^{-6}
$\psi(2S)$	10.9×10^{-4}	2.3×10^{-6}
$\Upsilon(nS)$, n = 1,2,3	(2.6,4.4,3.5) $\times 10^{-4}$	(1.0,1.2,2.3) $\times 10^{-6}$
ϕ	4.8×10^{-4}	0.9×10^{-6}
ρ	8.8×10^{-4}	25×10^{-6}
ω	1.0×10^{-4}	3.5×10^{-7}
K^*	8.9×10^{-5}	-

Table 2.2: Summary of the SM predictions for the branching ratios for $H/Z \to \mathcal{M} + \gamma$, $\mathcal{M} = J/\psi$, $\psi(2S)$, $\Upsilon(nS)$, ϕ, ρ, ω, K^* [2][3] and the 95% CL upper limits on the branching ratios. Calculations for the specific decay of a Higgs or Z boson to a particular meson state are not available, where entries have been left blank. [2][3][4][5]

2.6 Kinematic properties of exclusive final states

Estimating the acceptance for $H \to M\gamma$ decays within the ATLAS detector can be done using kinematic simulations, which provide an initial value for the proportion of events which might be detected.

Input files are produced using the `POWHEG` [65] and `Pythia8` [66] MC event generators, containing samples of Higgs bosons produced via various processes (gluon-gluon fusion, vector boson associated production ($W^{\pm}$/Z) and vector-boson fusion), and are used to simulate decays. A phase space is defined for the kinematics of the decay. Lorentz vectors are constructed for each particle in the decay using Monte Carlo, within the restrictions imposed by the phase space. For each decay channel, the effect of polarisation of the decay products on the overall detector acceptance is included, as it is not accounted for in the initial production of the MC.

The kinematic distributions for the $H/Z \to \omega\gamma$, $H \to K^*\gamma$, $Z \to K^0_S\gamma$, $H \to D^{*0}\gamma$ and $Z \to D^0\gamma$ channels are shown in Figures 2.8 - 2.13. These plots allow us to understand the effect of the polarisation on the acceptances of the decays, as well as the effect of fiducial selection requirements.

2.6.1 The polarisation of the decay products

The polarisations for the decay channels are evaluated following the procedure in Ref. [67].

The angular distribution of a $1 \to 2+3, 2 \to 4+5$ decay chain is described in the helicity formalism by:

$$I(\theta') = \frac{1}{\Gamma_1\Gamma_2}\frac{2s_2+1}{2}\sum_{\lambda_1\lambda_2\lambda_3\lambda_4}|d^{s_2}_{\lambda_2,\lambda_4-\lambda_5}|^2|A_{\lambda_2\lambda_3}|^2|B_{\lambda_4\lambda_5}|^2 \tag{2.10}$$

$$|\lambda_2 - \lambda_3| \leq s_1 \tag{2.11}$$

$$|\lambda_4 - \lambda_5| \leq s_2 \tag{2.12}$$

where $I(\theta')$ is the angular distribution of the decay products, $\Gamma_{1,2}$ are the decay rates of particles 1 & 2, $s_{1,2}$ are the spins of particles 1 & 2, and λ_i, $i \in [1,5]$ are the helicities of the labelled particles. $A_{\lambda_2\lambda_3}$ and $B_{\lambda_4\lambda_5}$ are the helicity amplitudes of the primary and secondary decays respectively. The following is a list of justifications for the chosen angular distributions for each decay channel in the document. For the decays $H \to \mathcal{M}\gamma, \mathcal{M} = K^{*0}, \omega$, the value of $s_1 = 0$. The K^{*0}, ω have $J^{PC} = 1^{--}$ and the photon is a massless vector boson $J = 1$, $m_J = \pm 1$. The $K^{\pm}, \pi^{\pm,0}$ have $J^P = 0^-$. From selection rules (2.10), (2.11), (2.12) the possible helicity amplitudes are $A_{1,1}$ and $A_{-1,-1}$. The assumption is made that the 3-body decay of the ω meson can be treated as a 2-body decay due to all the final state particles having equal spin = 0. Therefore, the meson is also transversely polarised, since $s_1 = 0$ and the photon only has transverse polarisations. For the B amplitudes the allowed value is

$B_{0,0}$ given $s_4 = s_5 = 0$. Therefore the only contributions to the angular distributions are $d^1_{1,0} = d^1_{-1,-0} = -\frac{\sin\theta'}{\sqrt{2}}$. The angular distribution is therefore $\sin^2\theta' = 1 - \cos^2\theta'$ for all mesons listed.

For the decays $Z \to \mathcal{M}\gamma, \mathcal{M} = \omega$, the value of $s_1 = 1$, and the Z has a mixture of polarisations - however, as pointed out in [50], the transversely-polarized component of the meson vanishes up to corrections of order $m^2_{\mathcal{M}}/M^2_Z$. Therefore, the mesons in the decays are only longitudinally polarized. The assumption is made that the 3-body decay of the ω meson can be treated as a 2-body decay due to all the final state particles having equal spin = 0.
The allowed helicity amplitudes based on (2.10), (2.11), (2.12) are $A_{0,-1}$ and $A_{0,1}$, and $B_{0,0}$ as $s_4 = s_5 = 0$.
Thus the only contributions to the angular distribution are from $d^1_{0,0} = \cos\theta'$ and the angular distribution is thus $\cos\theta'$.

For each decay channel, a range of kinematic variable distributions were studied in order to inform analysis strategies and examine the effects of polarisation on the decay products. For example, the following are some of the distributions produced: photon p_T, leading/subleading track p_T, invariant mass of the ditrack system, ΔR between tracks, ΔR and Φ between $\mathcal{M}$ and photon.

The rare decays of the Higgs boson to $\omega\gamma$ provides sensitivity to the up- and down-quark couplings to the Higgs boson. The final state of this decay is similar to that of the decay $H \to \rho\gamma$, with the addition of a π^0 in the final state. Searches for decays of the Higgs boson to the mesons $K^{*0}(d\bar{s})$ and $D^{*0}(c\bar{u})$ result in similar final states of two tracks and a photon. The distinction between these two channels and the other mesons is that these decays imply flavour-changing Yukawa interactions with the Higgs boson due to the quark contents of the mesons. This arises through loop-induced contributions in the SM at a very small rate, however there are a variety of BSM models that incorporate Yukawa interactions that change flavour with higher rates.

The following pages show the raw distributions before any fiducial and preliminary selection requirements are applied based on the ATLAS detector geometry and acceptance (blue), as well as distributions with these selection requirements applied (green). Where the invariant mass of the ditrack system is missing, the value of the mass used for the meson is fixed rather than being drawn from a distribution, due to the negligible width of the particle. These selection requirements are shown in Table 2.3.

	Selection requirement						
Meson $\mathcal{M}$	$\lvert\eta_{lead,sub}\rvert$	$\lvert\eta_\gamma\rvert$	$\lvert\Delta\phi_{\mathcal{M},\gamma}\rvert$	min pT_{lead} [GeV]	min pT_{sub} [GeV]	min $\mathrm{pT}_{\mathcal{M}}$ [GeV]	min pT_γ [GeV]
J/ψ	< 2.5	< 1.37, > 1.52	$> \frac{\pi}{2}$	3.0	3.0	35.0	35.0
$\psi(2S)$				6.0	6.0		
ϕ				15.0	15.0		
ρ							
K^{*0}/K^0_S							
D^{*0}/D^0							
ω					3.0	25.0	30.0

Table 2.3: Selection requirements for the discussed rare exclusive H and Z boson decays. 'Lead' and 'Sub' refer to the leading and subleading leptons in p_T, and p_T is defined in the lab frame.

These distributions allow the kinematics of the decay channel to be understood. The acceptance for signal events can be defined by determining how many events are within the criteria imposed by the cuts. This value can be determined for both non-polarised and polarised decays. As an example, the acceptance for $H \to \omega\gamma$ decays with(out) polarisation effects is 29.3%(36.3%), and for $Z \to \omega\gamma$ it is 14.9%(15.7%). This demonstrates the significant effect in the reduction of the acceptance due to the helicities of the decay products, which affects their angular distribution. A different angular distribution will vary the number of events falling within the selection criteria. This effect on the acceptance is summarised in Table 2.4 for multiple decay channels. The plots shown take into account the decay product polarisation, and use the selection requirements given in Table 2.3.

The distributions are useful in informing both the trigger strategy and the overall analysis selection and strategy for all the decay channels of interest. Additionally, it allows new decay channels to be studied with relative ease. For example, Fig.

2.8(d) shows the invariant mass combination of the final state products for the $H \to \omega\gamma \to \pi^+\pi^-\pi^0\gamma$ decay channel, excluding the π^0. This allows us to determine whether a potentially difficult reconstruction can be avoided, and whether there is indeed a need to reconstruct the neutral pion. As the distribution shows, the neutral pion is indeed important and needed for an accurate reconstruction of the Higgs boson mass. The same reasoning was applied for the analogous Z boson channel, for which the same distribution is shown in Fig 2.9(d). In addition, the distributions of the invariant mass of the ditrack system allow us to estimate the effect of the π^0 to the acceptance. The distributions are produced based on cuts on the $\pi^\pm$ tracks. The π^0 will leave a more prominent signal in the calorimeter, hence the trigger used for this channel uses a looser calorimeter requirement in order to try and include the energy contribution from the $\pi^0 \to \gamma\gamma$ decay. This will allow a more accurate determination of the three-body invariant mass.

Meson $\mathcal{M}$	Acceptance ($\% \pm (< 0.1\%)$)			
	$H \to \mathcal{M}\gamma$		$Z \to \mathcal{M}\gamma$	
	Polarised	Non-polarised	Polarised	Non-polarised
J/ψ	40.8	42.9	26.2	23.3
$\psi(2S)$	30.8	32.6	23.6	20.7
ϕ	47.9	47.6	24.7	26.2
ρ	33.1	24.8	1.5	0.9
ω	29.3	36.3	14.5	15.7
K^{*0}/K^0_S	34.8	29.7	-	11.6
D^{*0}/D^0	30.5	22.7	-	7.8

Table 2.4: Acceptances for the decays $H/Z \to \mathcal{M}\gamma$, assuming detector selection criteria and both accounting for and ignoring polarisation. Empty entries in the table are where the polarisation is determined to not have an effect on the angular distribution of the decay products.

This procedure is repeated for a list of possible decays of interest - these distributions have been produced for the searches summarised in Section 2.5, as well as for searches not yet performed such as $H \to \mathcal{M}\gamma$, $\mathcal{M} = D^{*0}$ and $Z \to \mathcal{M}\gamma$, $\mathcal{M} = K^0_s, D^0$. The kinematic distributions for these have been included regardless, as they demonstrate the usefulness of these studies in determining the kinematic selections. The decay channels mentioned here that have not yet been searched for have the distinction of being non-prompt decays, and the effect of this distinction can be seen in the

kinematic distributions.

As a results of these studies the effect of the polarisation on the acceptances of the rare decays of the Higgs boson to a meson and a photon have been quantified. In the cases of the $H \to \mathcal{M}\gamma$ decays, for $\mathcal{M} = J/\psi, \psi(2S), \omega$ there is a loss in the acceptance when helicity is taken into account, and for the other mesons there is a gain in the acceptance. In the cases of the $Z \to \mathcal{M}\gamma$ decays, for $\mathcal{M} = \phi, \omega$ there is a loss in the acceptance when helicity is taken into account, and for the other mesons there is a gain in the acceptance, except for the D^0 and K_s^0 decays. For these decays, the helicity is shown not to have an effect on the kinematics of the decay, and so does not require accounting for.

The effect of the polarisation is different depending on whether the decay is originating from a Higgs boson or a Z boson. Since the Higgs boson is a scalar particle, the polarisation of the resulting meson is dependent only on the polarisation of the photon, which is transverse. However, for the Z boson decay, the spin is 1, with a mix of polarisations. However, the transversely-polarised component of the meson has a dependency of the form $\frac{m_{\mathcal{M}}^2}{M_Z^2}$. Therefore, if the mass of the meson is small compared to the mass of the Z boson, which is the case here, then the transversely-polarised meson disappears to leading order. This means the meson will be longitudinally polarised. This distinction results in the differences in the acceptances shown in Table 2.4.

Overall, these kinematic studies and distributions allow us to inform the analysis strategy and selection, and gives an understanding of the effect of the polarisation on the acceptance of the decay channels under consideration. For the analyses presented in this document, these distributions were instrumental in dictating the analysis strategy.

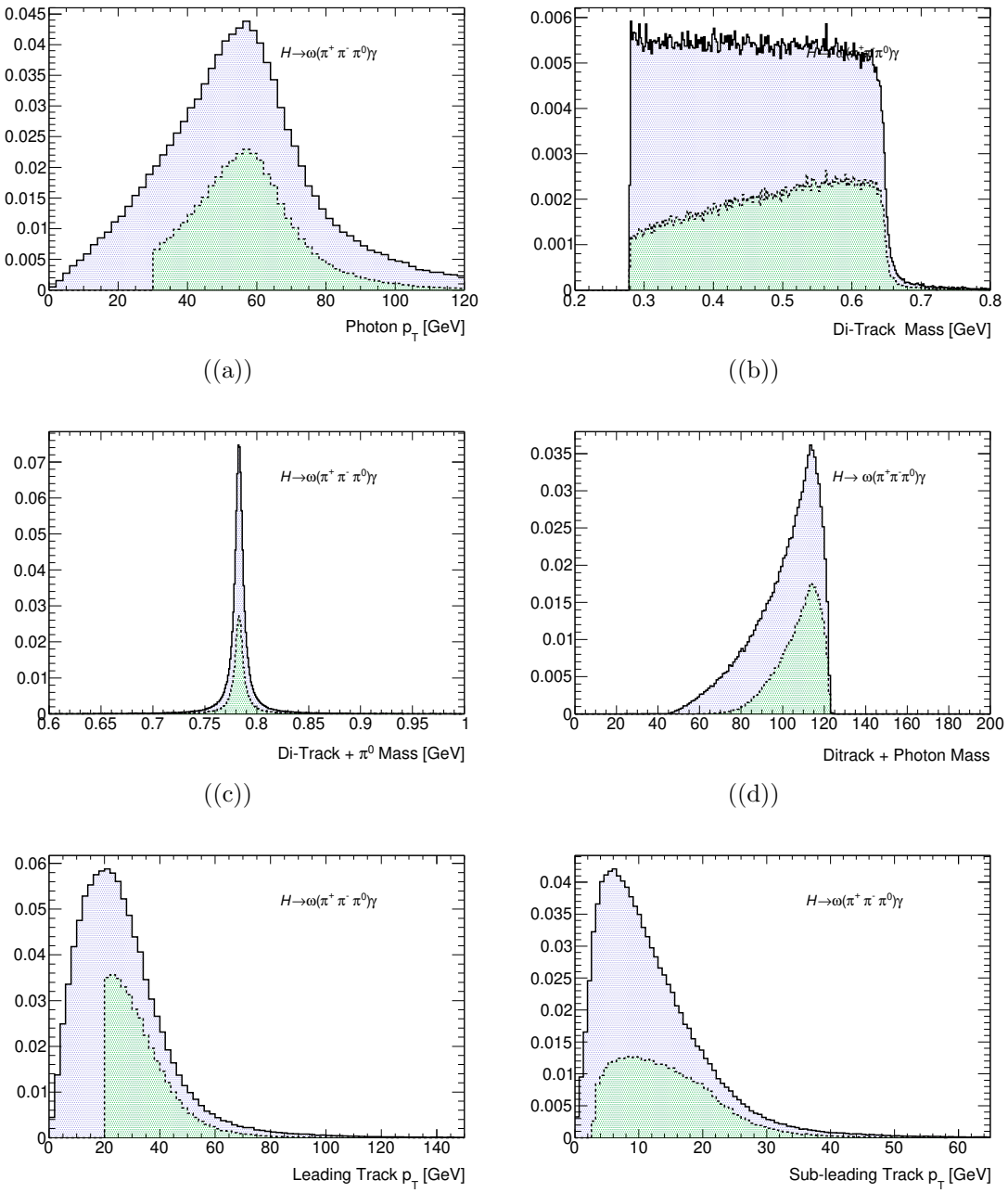

Figure 2.8: Kinematic distributions for the $H \to \omega\gamma \to \pi^+\pi^-\pi^0\gamma$ decay channel. Blue distributions are before fiducial cuts are applied, green distributions are after the cuts are applied. Plots are normalised relative to the blue distribution.

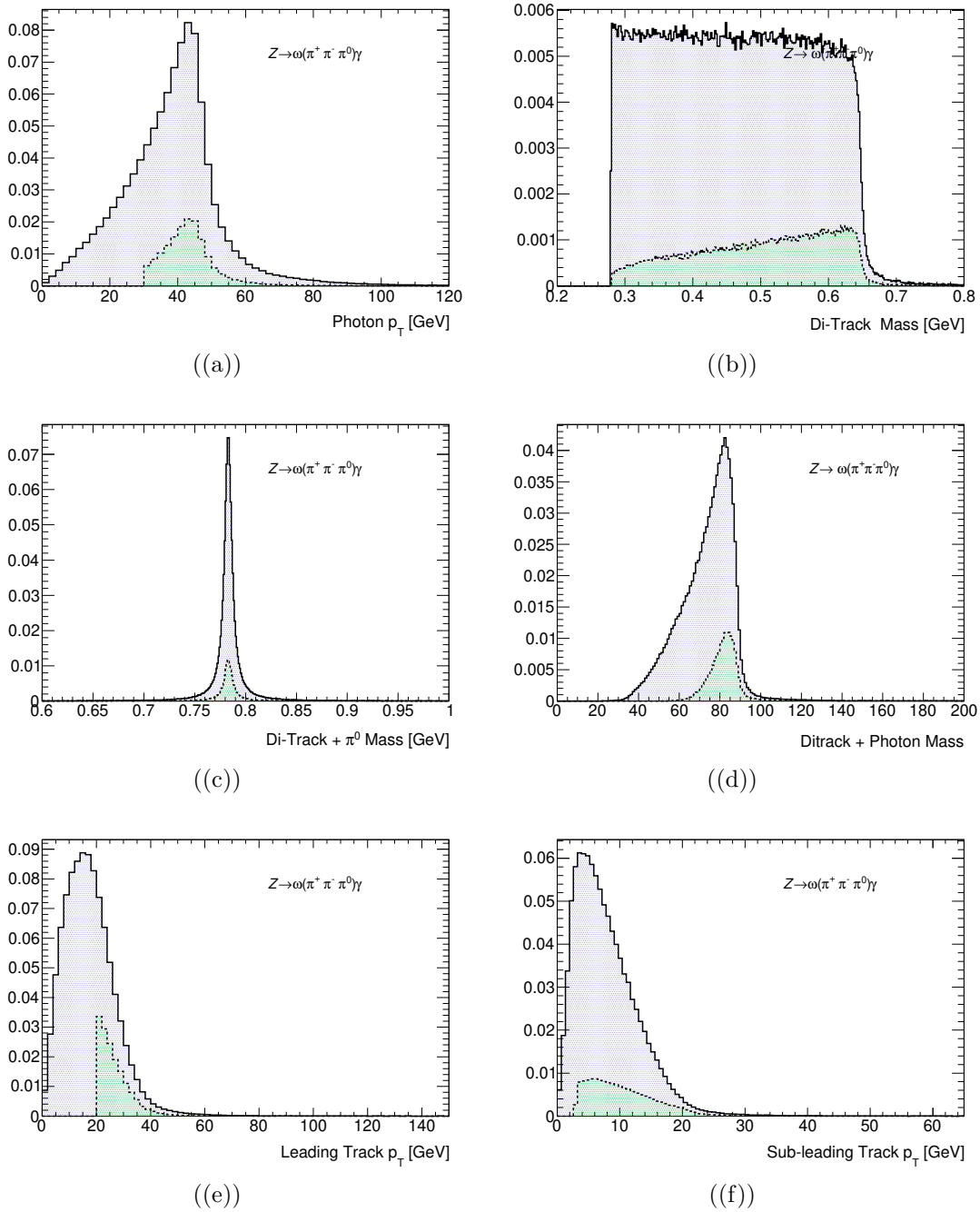

Figure 2.9: Kinematic distributions for the $Z \to \omega\gamma \to \pi^+\pi^-\pi^0\gamma$ decay channel. Blue distributions are before fiducial cuts are applied, green distributions are after the cuts are applied. Plots are normalised relative to the blue distribution.

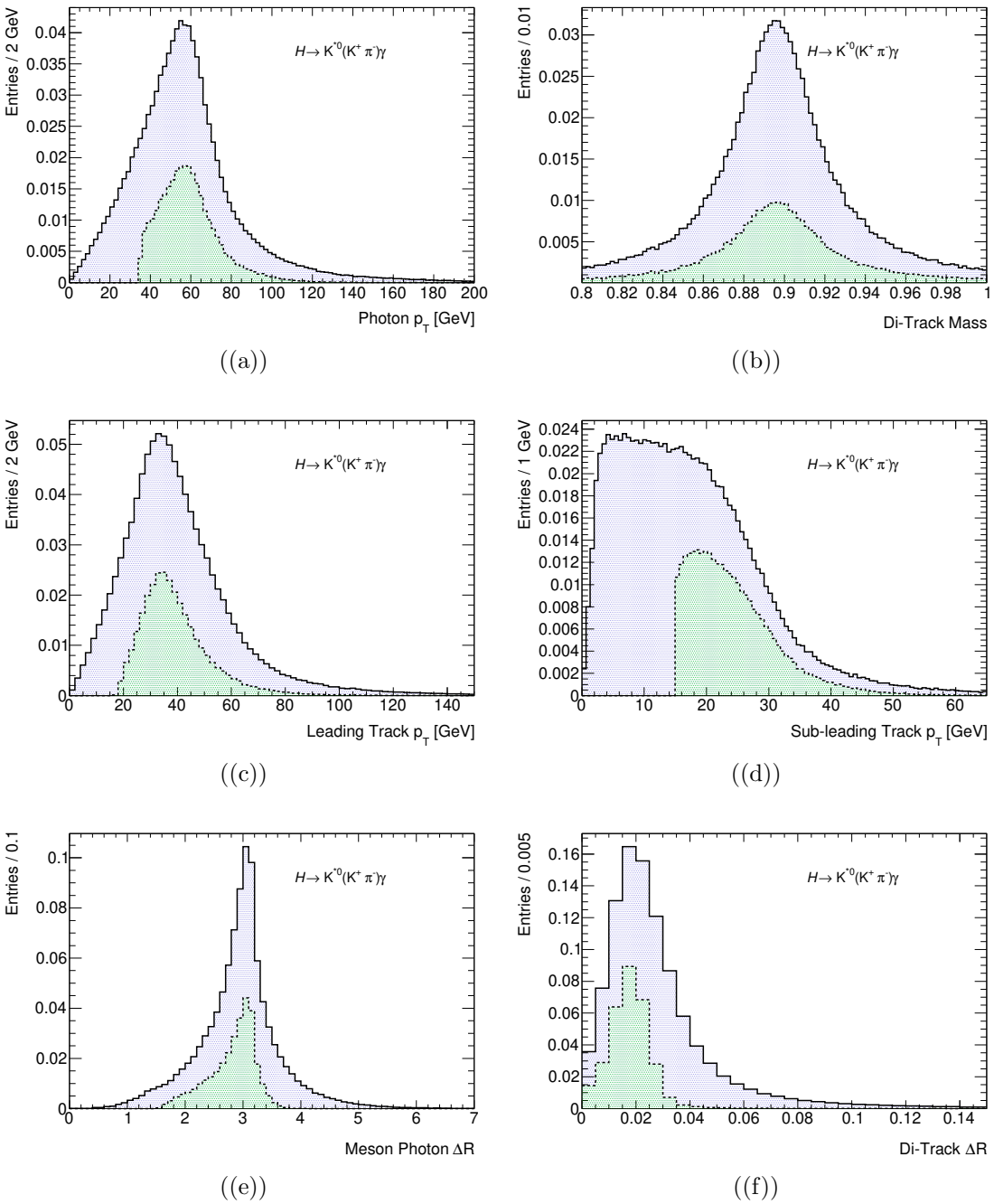

Figure 2.10: Kinematic distributions for the $H \to K^{*0}\gamma \to K^{+}\pi^{-}\gamma$ decay channel. Blue distributions are before fiducial cuts are applied, green distributions are after the cuts are applied. Plots are normalised relative to the blue distribution.

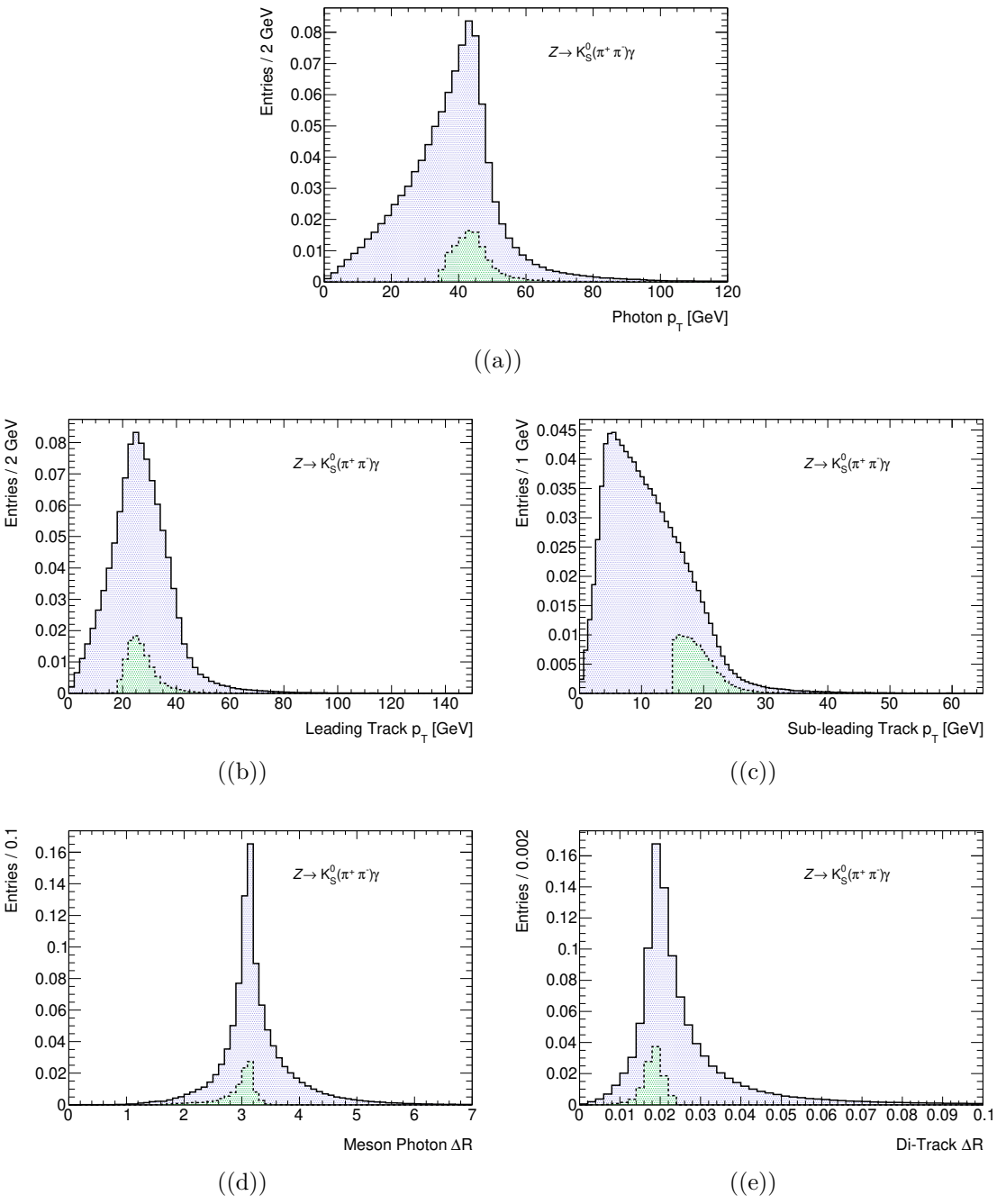

Figure 2.11: Kinematic distributions for the $Z \to K^0_S\gamma \to \gamma$ decay channel. Blue distributions are before fiducial cuts are applied, green distributions are after the cuts are applied. Plots are normalised relative to the blue distribution.

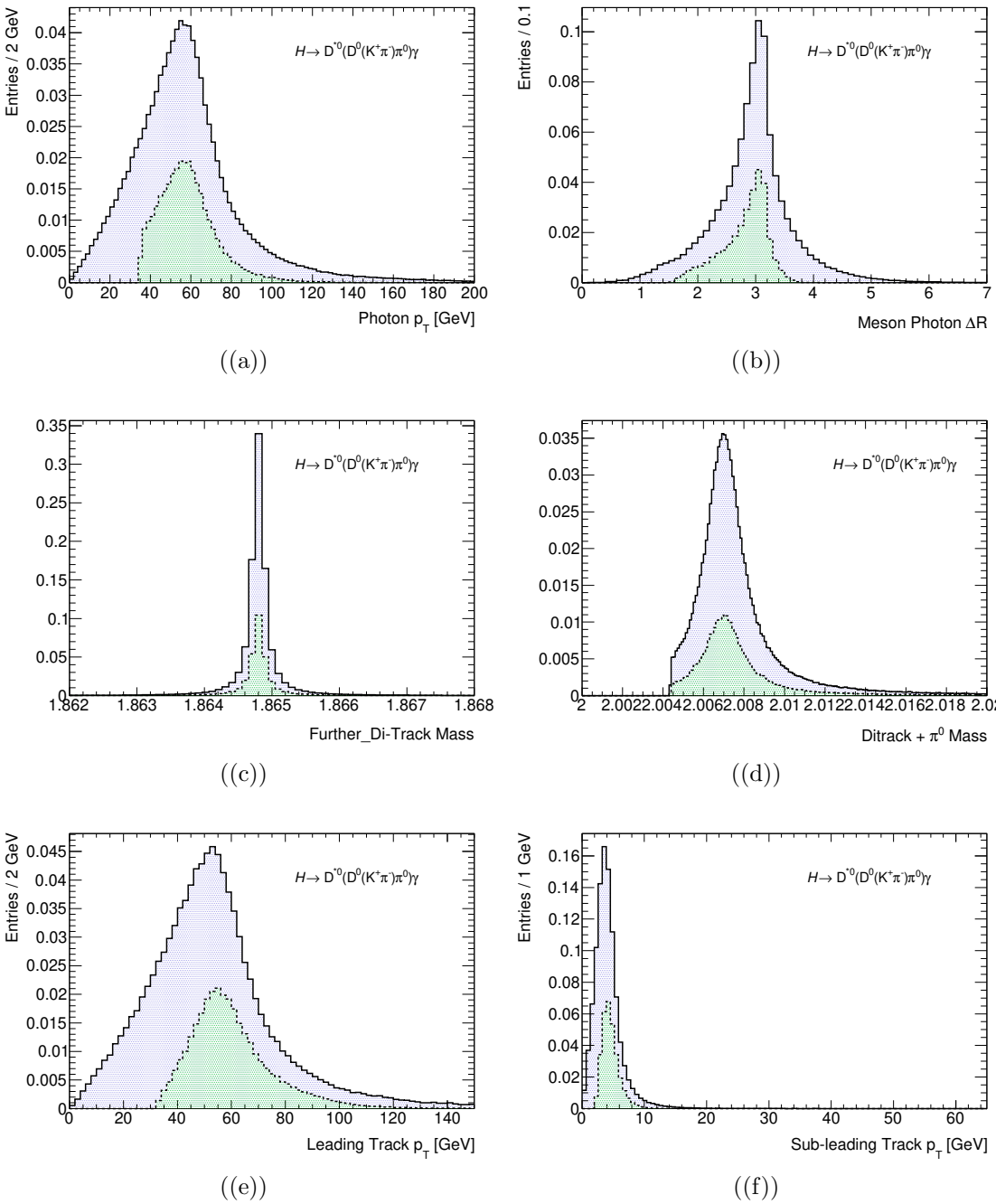

Figure 2.12: Kinematic distributions for the $H \to D^{*0}\gamma \to D^0(K^+\pi^-)\pi^0\gamma$ decay channel. Blue distributions are before fiducial cuts are applied, green distributions are after the cuts are applied. Plots are normalised relative to the blue distribution.

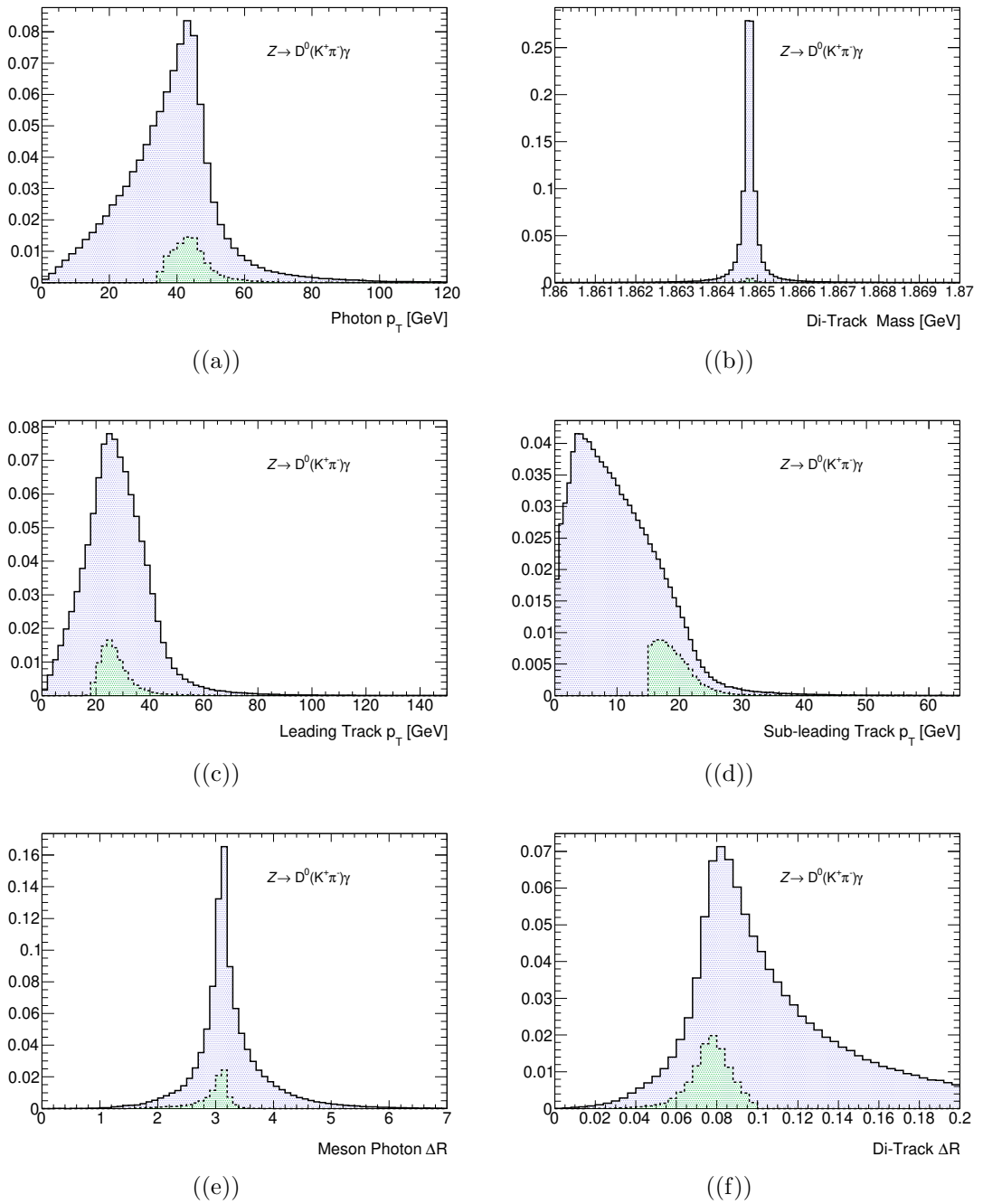

Figure 2.13: Kinematic distributions for the $Z \to D^0\gamma \to K^+\pi^-\gamma$ decay channel. Blue distributions are before fiducial cuts are applied, green distributions are after the cuts are applied. Plots are normalised relative to the blue distribution.

CHAPTER 3

The ATLAS detector at the CERN LHC

The ATLAS detector, situated within the ring of the CERN Large Hadron Collider, provides the precision necessary to perform searches such as those described in this thesis, as well as a multitude of other experimental measurements.

3.1 The Large Hadron Collider

The Large Hadron Collider (LHC) [24] is a superconducting circular hadron accelerator situated in the 26.7 km circumference tunnel originally constructed for the Large Electron-Positron Collider (LEP, 1989-2000) [68]. The nominal design of the LHC is to accelerate and subsequently collide two counter-rotating beams of protons with a centre of mass energy ($\sqrt{s}$) of up to 14 TeV. The design also allows for the use of heavy ions rather than protons, most commonly lead nuclei, with a centre of mass of 2.3 TeV per nucleon, to allow for lead-lead or lead-proton collisions. The

main physics goals for the collider include Higgs boson searches and measurements of its properties; measurements; tests of the Standard Model; and searches for exotic and supersymmetric particles, at the TeV energy scale.

The LHC has a depth varying between 50 to 170 meters. It consists of 8 arcs and straight sections, where the straight sections are approximately 528 m long and serve as experimental insertion points. The particle-particle collider consists of two beam pipes with beams travelling in opposite directions. In order to maintain beam quality and avoid spurious collisions from gas molecules, they are kept at a high vacuum of approximately 10^{-13} atm. A total of 9593 magnets of varying type (dipole, quadrupole, sextupole) are combined with radio-frequency (RF) cavities to make the LHC. The only way to achieve the designed $\sqrt{s}$ for the collider is to use superconducting technology, therefore roughly 96 tonnes of liquid helium are used to maintain an operational temperature of 1.9 K (-271.3 °C) for the magnets. The most essential magnets are the 1232 superconducting dipoles. Each magnet is 14.3 m long and weighs 35 tonnes. The superconducting component of the magnets is the niobium-titanium (NbTi) cable coils, which become superconducting at T $<$ 10 K. A current of 11850 A runs through these coils to produce a magnetic field of strength 8.33 T. This bends the beams in a circular path, and is the main limitation to achieving higher energies at the LHC.

Proton beams require production and refinement before being injected into the main LHC ring. Initially, ionised hydrogen gas is used to produce protons, accelerated using a linear accelerating structure (LINAC 2) up to an energy of 50 MeV. This is directed into the Proton Synchrotron Booster (PSB), which accelerates the particles to 1.4 GeV, which feeds then into the Proton Synchrotron (PS), which further increases the energy to 25 GeV. The penultimate chain is the 6.9 km long Super Proton Synchrotron (SPS), which raises the energy to 450 GeV, before the protons are transferred to the two beam pipes of the LHC ring. The final acceleration within the LHC ring brings the beams to their nominal energy of 7 TeV in approximately

20 minutes. This complex is depicted in Figure 3.1.

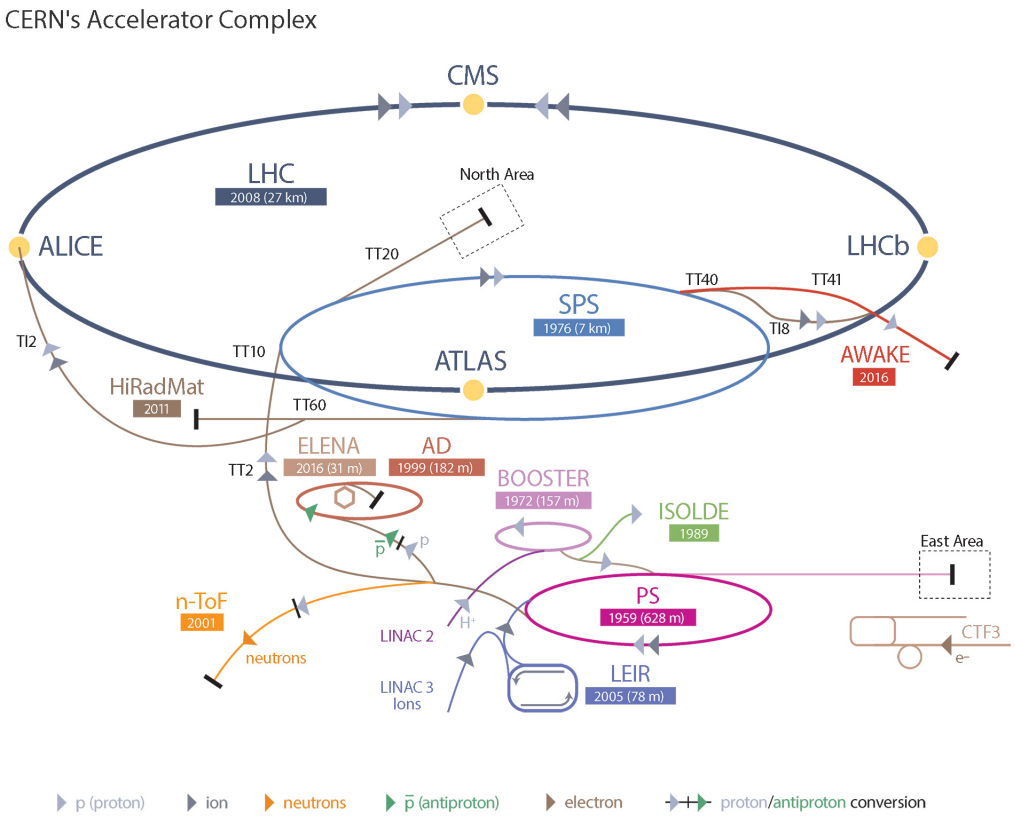

Figure 3.1: The CERN accelerator complex. Figure from Ref. [12]

In separate regions within the straight sections around the LHC, the two counter-rotating beams are brought together at the interaction points (IPs). Situated around these points are the four main experiments: ATLAS (**A** **T**oroidal **L**HC **A**pparatu**S**) at IP1, CMS (**C**ompact **M**uon **S**olenoid) at IP5, LHCb (**L**arge **H**adron **C**ollider **b**eauty) at IP8, and ALICE (**A** **L**arge **I**on **C**ollider **E**xperiment) at IP2. ATLAS and CMS are general-purpose detectors, designed to probe a wide range of phenomena using the full potential of the LHC collision data. LHCb and ALICE are designed with more specific physics goals, providing dedicated studies on b-quark physics and heavy ion/quark-gluon plasma physics respectively.

Specific and well-defined beam parameters are required to allow physical processes

to be studied. For a given physics process at the LHC, the event rate is given by:

$$\frac{dN}{dt} = L \times \sigma, \tag{3.1}$$

where σ is the cross section for the process measured in barns (10^{-28} cm^2), and L is the instantaneous luminosity of the machine measured in cm^{-2}s^{-1}. The luminosity is independent of the process under consideration, and is determined purely from the parameters of the beams. The number of events produced for a particular data taking period is therefore obtained by integrating the above expression over time:

$$N = \int L dt \times \sigma = \mathcal{L} \times \sigma, \tag{3.2}$$

where $\mathcal{L}$ is now the integrated luminosity measured in barn^{-1}. By maximising the luminosity, we are more likely to observe rare physics processes such as the production of a Higgs boson, whose cross section is many orders of magnitude smaller than the total cross section of proton-proton collisions at the LHC.

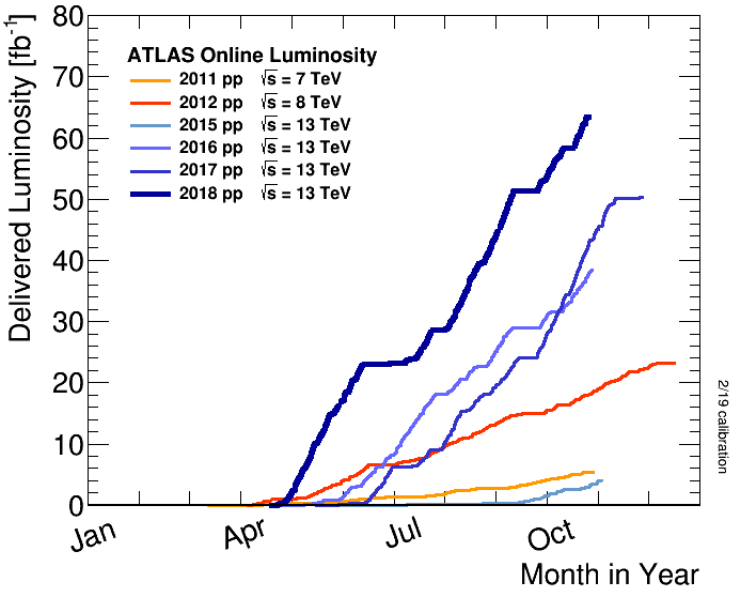

Figure 3.2: Integrated luminosity of proton-proton collisions delivered to the ATLAS detector by the LHC for the period 2011-18.

Figure 3.2 shows the total integrated luminosity delivered to the ATLAS detector (see next section) by the LHC using proton collisions to date. The LHC operating schedule consists of periods of data-taking, interspersed with shut-down periods where upgrades and maintenance are undertaken. In terms of major changes to the operation of the LHC, these are defined as runs, of which two have taken place. Run-1 took place between 2010-2012, and operated at $\sqrt{s}$ = 7-8 TeV and at a peak luminosity of 7.7×10^{33} cm^{-2}s^{-1}. The first long shutdown saw upgrades to the magnet system of the LHC such that during Run-2 (2015-2018) operation could be performed at $\sqrt{s}$ = 13 TeV. The second long shutdown, currently underway, is set to be complete at the beginning of 2022.

3.2 ATLAS detector

The ATLAS experiment [69] at the LHC is a general purpose particle detector, shown in Figure 3.3, with approximately forward-backward symmetric cylindrical geometry, with the direction of the beams defining the axis of symmetry. ATLAS consists of cylindrical layers of sub-detectors surrounding the beam interaction point ('barrel'), with two end-cap regions on either side in order to maximise the hermeticity of the detector. Immediately around the interaction point is the inner tracking detector (ID). This is surrounded by a thin superconducting solenoid. Following this are the electromagnetic and hadronic calorimeters (ECAL/HCAL). Finally, a muon spectrometer (MS) incorporates three large toroidal superconducting magnets. A trigger and data acquisition system (TDAQ) is also present, and is necessary to collect LHC data at the required rates. These subdetectors will be described in detail in the following sections.

ATLAS uses a right-handed coordinate system, centred around the interaction point. The direction of the beam defines the z-axis. The positive x-axis points towards the center of the LHC ring, and the positive y-axis points upwards. The $x-y$ plane is defined as the transverse plane, and is orthogonal to the beam; quantities including

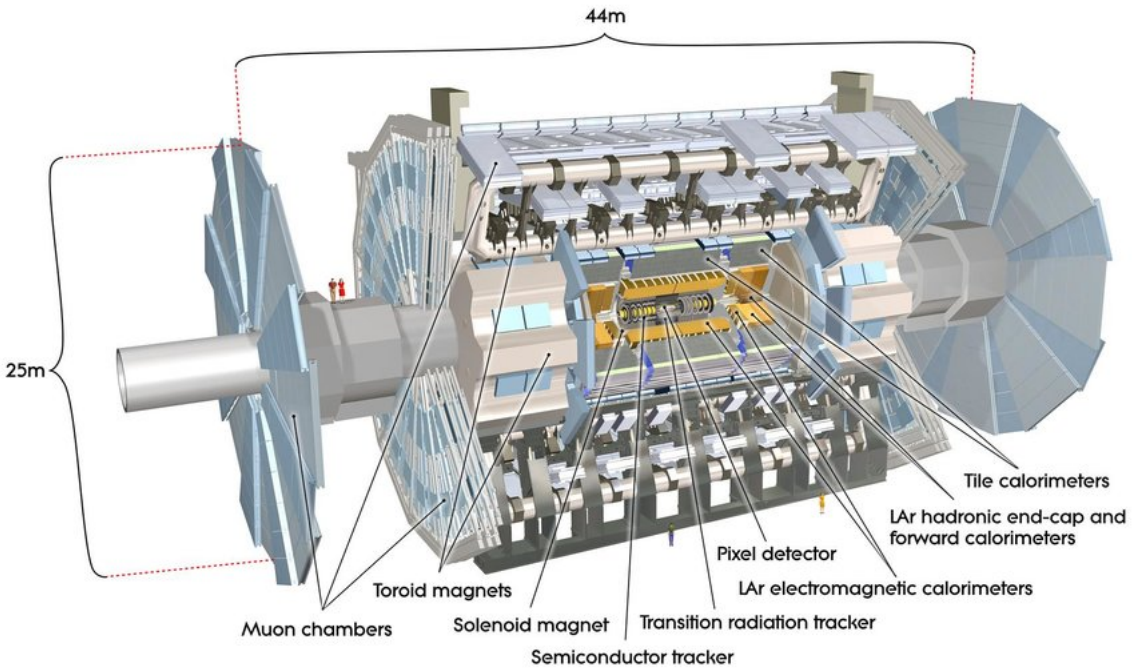

Figure 3.3: A view of the ATLAS detector and subsystems. [13]

transverse momentum ($p_T^2 = p_x^2 + p_y^2$) and transverse energy ($E_T = E \cdot \sin\theta$) are constructed relative to this. The polar angle θ is the angle from the beam axis, and the azimuthal angle ϕ is the angle around the beam axis. Two commonly used quantities, rapidity (y) and pseudorapidity (η) are defined as follows:

$$y = \frac{1}{2} \ln \left(\frac{E + p_z}{E - p_z} \right) \tag{3.3}$$

$$\eta = -\ln \tan \frac{\theta}{2} \tag{3.4}$$

where E is the energy and p_z is the component of the momentum along the beam axis. In the limit where the mass of a particle is zero, $y = \eta$, and both quantities are invariant to Lorentz boosts along the beam direction. A commonly used coordinate space is the $\eta - \phi$ space, using a distance:

$$\Delta R = \sqrt{\Delta\eta^2 + \Delta\phi^2} \tag{3.5}$$

3.2.1 Magnet system

The ATLAS magnet system [69] consists of 1 solenoidal and 3 toroidal superconducting magnet systems. The solenoidal magnet is the innermost part of the system and generates a 2 T axial magnetic field for the Inner Detector, which is aligned with the beam axis. A toroidal magnet is located at each endcap, and one within the barrel. The toroidal magnets produce a 0.5 T magnetic field in the barrel region for the Muon Spectrometer, and a 1 T magnetic field in the endcap regions. The purpose of these magnetic fields is to bend the trajectories of charged particles to allow the Inner Detector and Muon Spectrometer to perform momentum and charge measurements.

3.2.2 Inner Detector

The Inner Detector (ID) is the innermost layer of ATLAS, consisting of three precision tracking detectors designed for momentum measurements for charged tracks above 0.5 GeV and provide sufficient granularity to identify primary and secondary vertices [69]. The first layer is the pixel detector, consisting of the insertable b-layer (IBL) [70], surrounded by three layers of silicon pixel modules. There are roughly 80 million readout channels for these layers. This provides measurement points for charged particles produced at the interaction point (IP), with an accuracy of 10 μm in (R-ϕ), allowing accurate primary vertex reconstruction which is integral to many physics analyses. Secondly is the Semiconductor Tracker (SCT), 4 layers of silicon microstrip detectors, with more than 6 million readout channels. This typically provides four space points for charged particles from the IP, with an accuracy of 17 μm in the ϕ direction. Finally, the Transition Radiation Tracker (TRT) surrounds this, composed of gas filled straw-tubes. These typically provide 36 hits per track with

over 350k readout channels. The reduced accuracy of 130 μm is offset by the larger number of measurements and length of the track.

The performance of the ID can be shown through the track reconstruction efficiency for jets. Figure 3.4 shows the track reconstruction efficiency as a function of jet transverse momentum and as a function of the production radius of the jet. The decrease in efficiency for large production radii is largely due to fewer clusters being produced if particles are produced after the initial active layers of the ID, and the fact that the reduction in flight length between the next active layer causes the average separation between particles to be smaller, causing clusters to merge.

Figures 3.5 and 3.6 demonstrate the performance of the ID. Figure 3.5 shows the single-track reconstruction efficiency as a function of the initial particle's p_T. Figure 3.6 shows the relatively low level of tracks lost when reconstructing jets, as a function of the jet p_T.

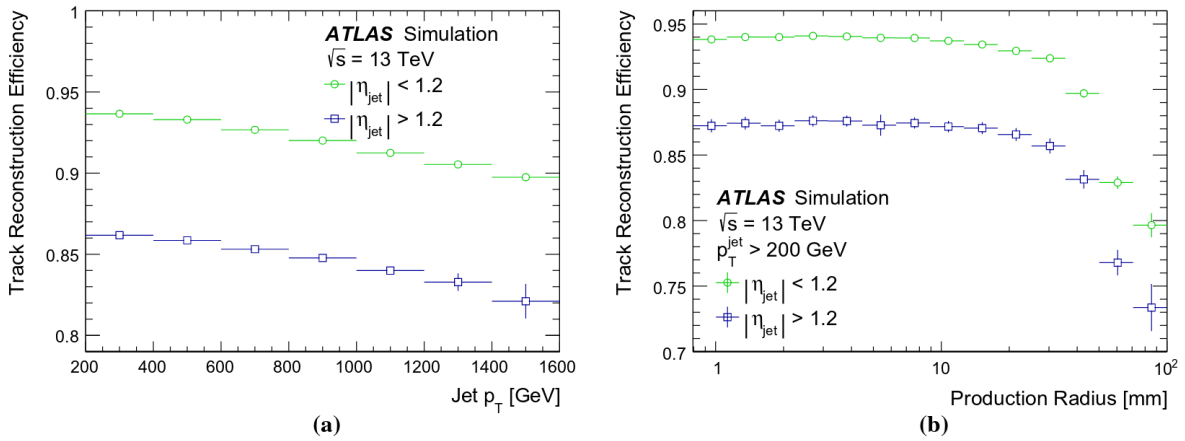

Figure 3.4: Track reconstruction efficiency for charged particles within simulated dijet MC events for different $|\eta|$ ranges as a function of the (a) jet p_T and (b) production radius. [14]

3.2.3 Calorimetry

The ATLAS calorimetry system consists of various electromagnetic and hadronic detectors designed to measure the energy of electrons, photons, τ leptons and hadronic jets, as well as provide some positional and directional information [69]. There are

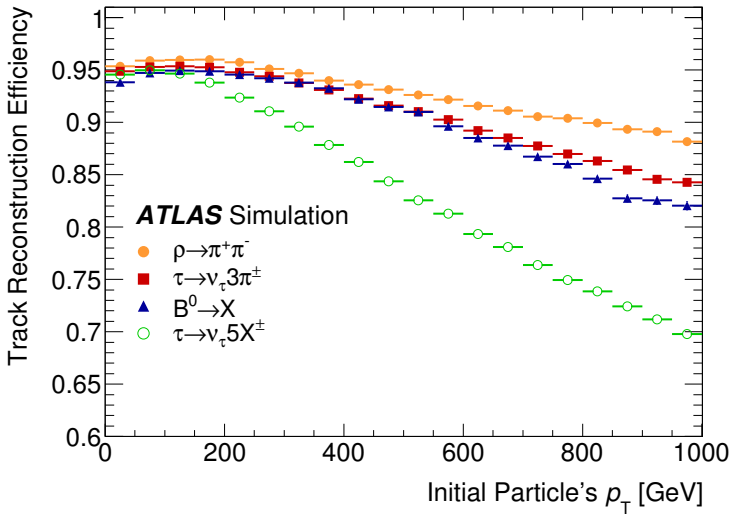

Figure 3.5: Single-track reconstruction efficiency is shown as a function of the initial particle's p_T when it is required that the parent particle decays before the IBL for the decay products of a ρ, three- and five-prong τ and a B0. [14]

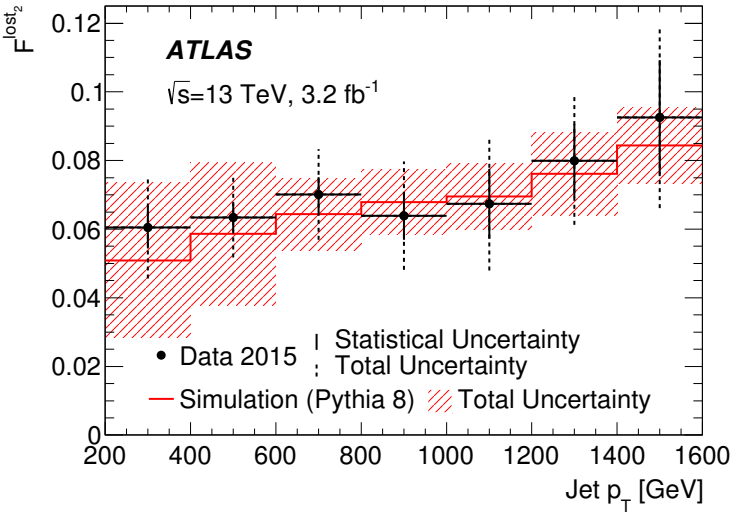

Figure 3.6: The measured fraction of lost tracks, Flost2, in the jet core (R(jet,trk)<0.05) as a function of jet p_T for data (black circles) and simulation (red line). [14]

two main types of calorimeter systems, the electromagnetic calorimeter (ECAL) and the hadronic calorimeter (HCAL). The innermost layer consists of one EM barrel calorimeter (EMB), one EM endcap calorimeter (EMEC) at each end, and equivalently one hadronic endcap (HEC) at each end, and finally a forward calorimeter (FCal). The outer layer consists of a hadronic calorimeter (TileCal), comprised of one central barrel and two extended barrels on either side.

The EM calorimeter is a sampling calorimeter, which consists of layers of sensitive material alternating with layers of dense absorber material. Particles which traverse the calorimeter will interact and lose energy within the dense absorber layers, forming showers of particles. For electrons, this is mainly through bremsstrahlung resulting in a photon emission, whereas for photons the primary mechanism is electron-positron pair production. The sensitive layers will then generate a signal which is proportional to the lost energy of the particle, through ionisation. The resulting showers are incident on the lead and liquid argon (Pb-LAr) detectors, arranged in an accordion shape, where the lead is the absorber material and the liquid argon is the active material.

The HCAL is used to identify, reconstruct and measure the energy of particle jets, and to quantify the missing transverse energy in an event through the measurement of hadronic showers, rather than electromagnetic. Hadronic showers are comprised of two main parts, an electromagnetic part (photons mainly from π^0 decays) and a hadronic component (various nuclear effects). There is an 'invisible' component to the hadronic energy, which is energy not contributing to the signal - this is largely due to the binding energy of nucleons released through nuclear reactions. The barrel region consists of a sampling calorimeter, using iron as the absorber material, and scintillators as the active medium. The endcap region consists of liquid argon for the active medium, and copper and tungsten plates for the absorbers.

The performance for electron reconstruction and identification [71] in the ATLAS detector is performed through a combination of energy deposits in the EM calorimeter and corresponding tracks in the ID. If an energy cluster in the EM calorimeter is consistent with the clusters typically left behind by an electron, an ID track is selected and fitted with the cluster as an extra hit. This determines a candidate for the electron.

Figure 3.7 [15] shows the efficiency for reconstruction electrons in $Z \to ee$ events as a function of the transverse energy E_T accounting for the full η range for the ATLAS detector, using 43.8 fb^{-1} of data recorded during 2017 at $\sqrt{s} = 13$ TeV.

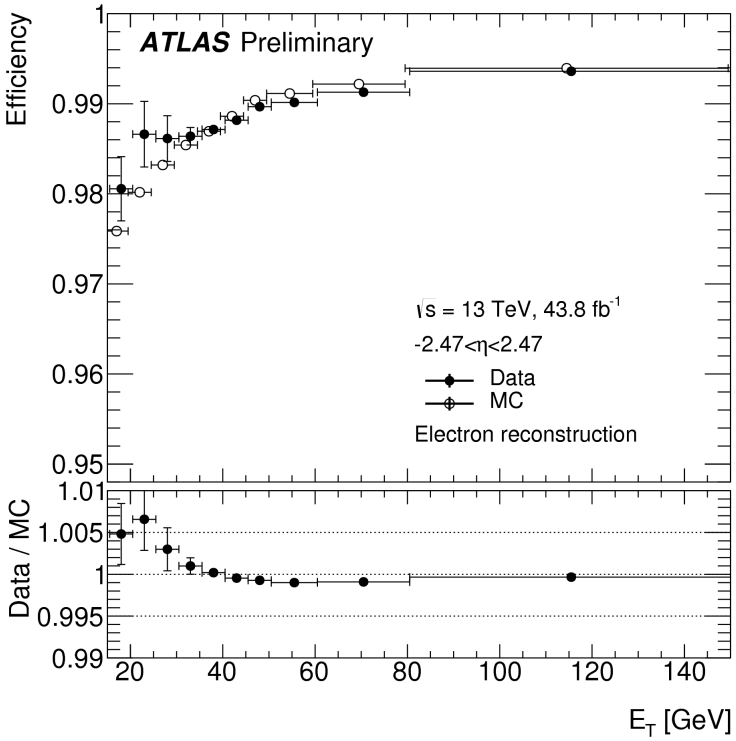

Figure 3.7: Electron reconstruction efficiency as a function of the transverse energy, using both simulated MC and collected data. [15]

The definition of the efficiency is the ratio of the number of reconstructed electrons over the total number of clusters. The efficiency for reconstruction is consistently high, and provides a basis for the algorithms used for identification. Typically, ATLAS works using a 99% or greater efficiency for high-E_T electrons.

The process for the reconstruction of photons in the ATLAS detector [72] begins in a similar way as to the electrons, in that an energy cluster in the EM calorimeter is searched for that is photon-like. No ID track is required for a photon. Tracks are searched for to reconstruct conversions resulting from photons, with photon conversions being used to generate vertex candidates which are matched to the clusters in the EM calorimeter. Algorithms are then used to distinguish between unconverted photons, converted photons and electrons, based on vertex and track matching to the energy clusters.

Figures 3.8 and 3.9 [16] show the identification efficiency for the *tight* requirement on photons, which involves not only the cluster and shower calorimeter information

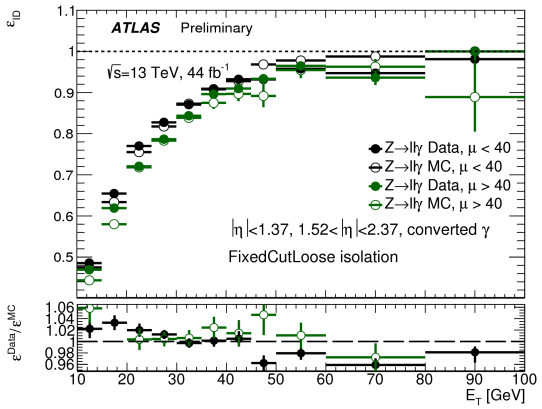

Figure 3.8: Converted photon identification efficiency. [16]

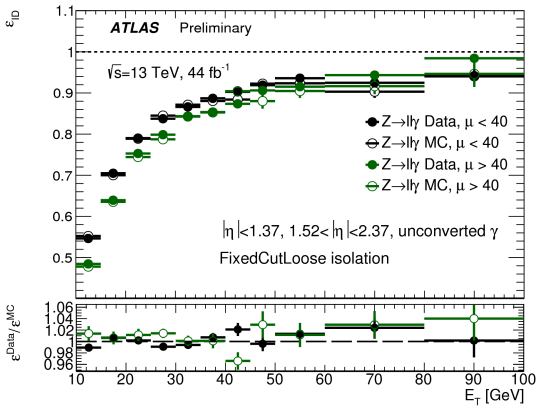

Figure 3.9: Unconverted photon identification efficiency. [16]

but also on information from the segmented layer of the calorimeter. Further details are provided in Table 3.1. The figures use a loose isolation requirement, based on the E_T, p_T and ΔR cone size. The efficiencies for converted photons increase from approximately 62-66% at $E_T = 20$ GeV to 92-94% at $E_T = 60$ GeV. For unconverted photons, the efficiencies increase from 64-70% at $E_T = 20$ GeV to 92-94% at $E_T = 60$ GeV.

		Variable	Description
Tight	Loose	R_{had}	Ratio of E_T in the HCAL to E_T of the EM cluster
		R_η	Ratio of 3×7 to 7×7 cell energies $\eta \times \phi$
		$w_{\eta 2}$	Lateral width of the shower in the 2^{nd} calorimeter layer
		w_{tots1}	Total lateral shower width in the strip calorimeter layer
		E_{ratio}	Ratio of the energy difference between the largest and second largest deposits to the sum of these energies
		ΔE	Difference between the energy of the 2^{nd} maxima and the lowest energy between the 1^{st} and 2^{nd} maxima in the strip layer
		f_{side}	Fraction of energy outside core of 3 central cells but within 7 cells
		w_{s3}	Lateral shower width calculated from 3 strips around the strip with the highest energy deposit in the strip layer
		R_ϕ	Ratio of 3×3 to 7×7 cell energies $\eta \times \phi$

Table 3.1: The variables used to define the photon ID working points 'tight' and 'loose'. [6]

3.2.4 Muon Spectrometer

The muon detection system within ATLAS is designed to detect particles that penetrate through the calorimeter systems, in particular muons [69]. Known as the Muon Spectrometer (MS), it is comprised of four main subsystems: the Monitored Drift Tube (MDT) chambers and Cathode Strip Chambers (CSC), which are precision trackers, and the Resistive Plate Chambers (RPC) and Thin Gap

Chambers (TGC), which are dedicated trigger chambers. These subsystems are implemented within large air-core superconducting toroidal magnets, covering a momentum-measurement range of $|\eta| < 2.7$ and serving as a trigger detector for $|\eta| < 2.4$. Particle trajectories within the magnetic fields are tracked, providing momentum measurements. The MS consists of a barrel section and two end cap sections. A plot of the reconstruction and identification efficiencies for muons at various working points used in ATLAS is shown in Fig 3.10, demonstrating high efficiencies at even low p_T values.

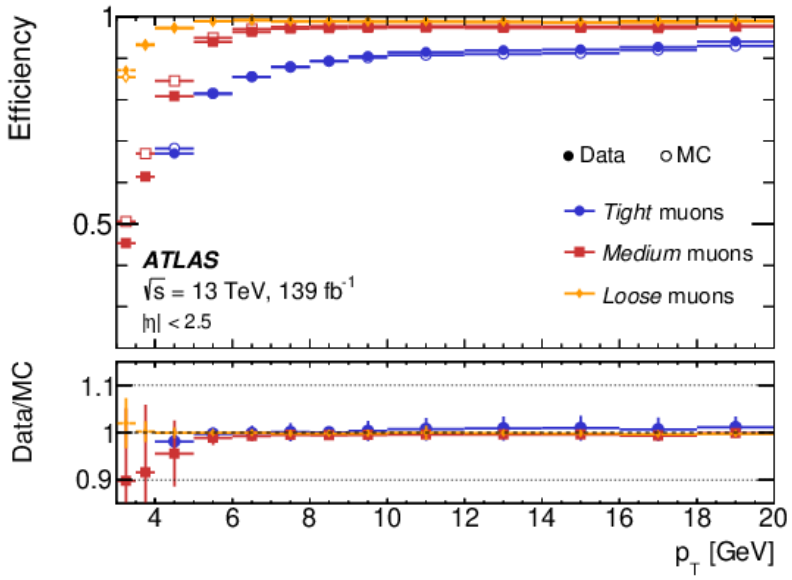

Figure 3.10: Muon reconstruction and identification efficiencies for the loose, medium and tight working points used, for $J/\psi \to \mu\mu$ events as a function of p_T. [17]

3.2.5 Trigger and Data Acquisition

Collecting data from events within ATLAS is a vast technological challenge, and current systems are not sufficiently advanced to collect all event information. In order to cope with the high rates, a trigger system [69] is required which reduces the input rate of events from proton-proton collisions from a rate of 40 MHz (bunch crossing rate) to a final output rate of roughly 1 kHz to record for further analysis. Another quantification of this is considering the amount of data per event. The

information for a single event corresponds to roughly 1 MB of data, and the rate for writing this information to disk is on the order of 100 MB/s, requiring a reduction in rate of around 5 orders of magnitude. The current trigger system in ATLAS has two levels. The first level (L1) is hardware-based, taking in coarse granularity information from both the calorimeters (L1Calo) and the muon system (L1Muon) in order to make very fast decisions (< 2.5 μs), reducing the rate to approximately 100 kHz. The second level (HLT) is a software-based trigger, utilising the full precision capabilities and granularity of the different ATLAS subsystems. This level further reduces the rate from 100 kHz to approximately 1 kHz with an average processing time of 200 ms.

The L1 trigger uses both calorimeter and muon system information. L1Calo uses coarse granularity information in order to classify objects into criteria such as EM clusters, τ-leptons, jets, missing E_T, E_T sum, and total jet transverse energy. This classification is performed mainly using trigger towers, collections of cells which are 0.1×0.1 in $\Delta\eta$ and $\Delta\phi$ over almost all of the calorimeter coverage. Using the multiplicities and thresholds of these various objects, a decision is made. L1Muon relies on trajectory information received from the RPC and TGC trigger chambers, using muon p_T thresholds to perform a decision. Overall, the decision for whether an event is accepted or rejected at L1 is made by the central trigger processor (CTP), which contains up to 256 preset configurations (items). These consist mainly of different sets of E_T or p_T requirements (thresholds), as well as isolation and size criteria for various objects. The overall acceptance for each item can be controlled through prescale factors, which reduce the events passing particular thresholds to a subset to pass through to the next level of trigger. The output from the L1 trigger is typically a Region of Interest (RoI). L1 trigger rates during standard data taking are illustrated by Figure 3.11. The average number of interactions per bunch crossing is denoted with $< \mu >$.

The High Level Trigger (HLT) [73] uses the RoIs from the L1 trigger as input,

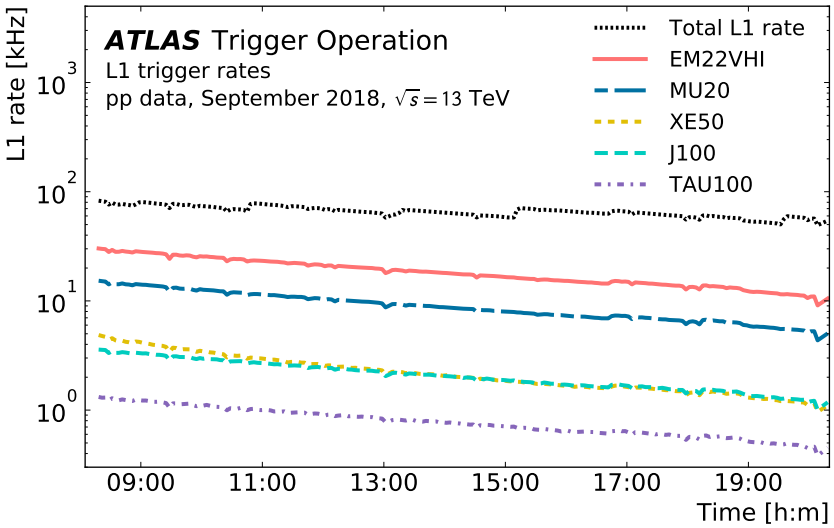

Figure 3.11: L1 trigger rates for physics during data-taking (September 2018). The peak instantaneous luminosity at the time was $\mathcal{L} = 2.0 \times 10^{34}\text{cm}^{-2}\text{s}^{-1}$, with a maximum $< \mu >= 56$. The plot shows representative single-object triggers, without prescaling. [18]

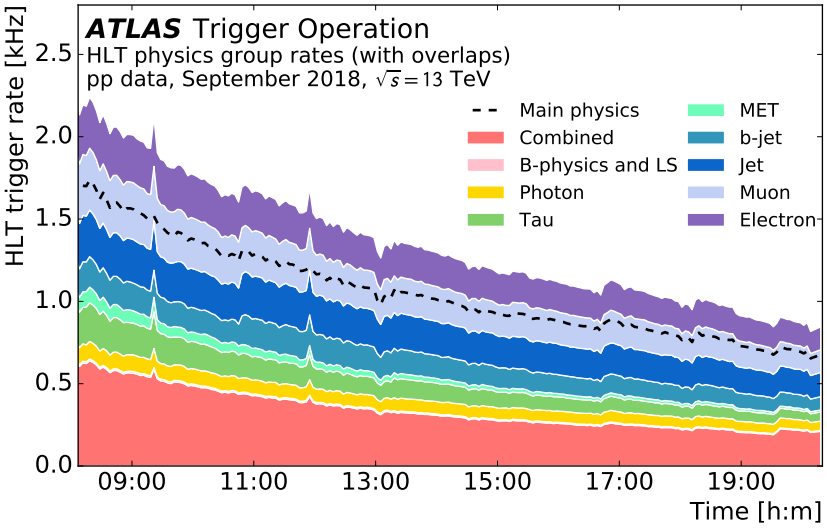

Figure 3.12: HLT rates organised in physics groups during data-taking (September 2018). [18]

and performs offline-like selections with more precision than previous stages. The HLT takes the form of a single farm of approximately 40,000 processor cores, which process the RoIs into data 'chains', which are then written to disk. The HLT is responsible for reducing the rate of data written to disk from the hardware-based

Level-1 (L1) Trigger. HLT reconstruction has the capability of being executed either within the RoIs defined in L1, or for the full detector. To reduce the processing and computation times for the algorithms, the majority of triggers use a two-stage system. The first stage is typically a fast reconstruction, the aim of which is to reject the majority of background events. The second stage is a slower but more precise reconstruction for the events which pass the first stage. HLT trigger rates during standard data taking are illustrated by Figure 3.12.

3.3 Trigger strategy for exclusive final states

Dedicated triggers were employed for these searches in order to accept events. The triggers for the track final states rely on a modification of the triggers used for τ-lepton identification, as the signature in the detector for the $\mathcal{M}$ decays is of a similar topology (two tracks in the ID). Similar triggers were used for decays with muon final states, which instead trigger on muons rather than a modified τ-lepton object. Various triggers were implemented, with different thresholds for acceptance, corresponding to different efficiencies for signal events.

The triggers are summarised in Table 3.2, where `g35` corresponds to an isolated photon with $p_T > 35$ GeV, `tau[25,35]` corresponds to a tau p_T cut of [25,35] GeV, `kaonpi1` and `dipion3` correspond to different mass windows of [790,990] MeV and [279,648] MeV respectively,and calorimeter isolations for the invariant mass of the tracks, and the remaining terms in the names are defined later in this document. In addition, there are requirements on the track p_T for both the leading and subleading p_T tracks, and a requirement on the ratio between the ratio of the p_T of the EM cluster associated to the τ and the p_T of the ditrack system.

Decay channel	Trigger name	Luminosity (fb^{-1})	Years operating
$H \to K^*\gamma \to K^+\pi^-\gamma$	HLT_g35_medium_tau25_ kaonpi1_tracktwo_L1TAU12	32	2016
	HLT_g25_medium_L1EM24VHI_tau25_ kaonpi1_tracktwo_50mVis10000	102	2017-2018
$H \to \omega\gamma \to \pi^+\pi^-\pi^0\gamma$	HLT_g35_medium_L1EM24VHI_tau25_ dipion3_tracktwo_60mVis10000	89.5	2017-2018

Table 3.2: Summary of triggers used in the analyses, including the logical names, luminosities and years of operation.

3.4 Data and MC simulation

3.4.1 Data Sample

The analyses are performed with a data sample collected between runs 300271 in 2016 to 364485 in 2018 at $\sqrt{s} = 13$ TeV, which corresponds to a total integrated luminosity of 135.2fb^{-1} for the $H \to K^*\gamma$ analysis, and 89.5fb^{-1} for the $H/Z \to \omega\gamma$ analyses based on the triggers, with a 1.7% uncertainty on the total Run-2 dataset. Runs included in the "Good Run Lists" were included in the analysis. Good Run Lists only include runs where the detector was operating under normal operating conditions with no major faults or exclusions. The triggers applied to the data samples are detailed in Section 5.1 in this document. The data is processed using a relevant (`DxAOD_HDBS2`) derivation. Derivations allow large samples of data to be skimmed and reduced in size to only retain relevant reconstruction and auxiliary information pertaining to an event.

Events kept in `DxAOD_HDBS2` fulfil the following conditions. They contain at least two reconstructed inner detector tracks with $p_{\mathrm{T}} > 15$ GeV. The invariant mass of the system of the two reconstructed inner tracks, assuming that both of them are pions, must satisfy $2 \times m_{\pi}(493.677 \text{ MeV}) < m_{\pi^+\pi^-} < 1.2$ GeV. Finally, a photon candidate with $p_{\mathrm{T}}^{\gamma} > 15$ GeV is present in the event.

3.4.2 Simulated Samples

Various Higgs production modes are used in the analyses presented. Gluon fusion and vector boson fusion Higgs boson production are simulated with POWHEG NLO [74, 75] interfaced with PYTHIA8.1 [76]. Parton shower, hadronisation, and underlying events were modelled with the AZNLOCTEQ6L1 tune. Higgs boson associated production with a W or Z boson, or a top-quark/top-anti-quark pair is modelled at leading order with PYTHIA8.1, using the CT10 parton distribution functions [77] and the A14NNPDF23LO tune.

The inclusion of ttH production has not been previously considered in published $H \to M\gamma$ analyses. The all-hadronic, semi-leptonic and di-leptonic decay channels are considered, as their contribution to the limit has not been quantified using ATLAS MC samples. In line with the relative cross-section for these decay channels, the contribution ends up being negligible in comparison.

The details of the production of the MC samples are shown in Table 3.3.

Higgs Production Mode	**Generator + PDF**	**Particle showering**	**UE model**
ggH	PowhegBox v2 + CT10	Pythia 8	AZNLOCTEQ6L1
VBF	PowhegBox v2 + CT10	Pythia 8	AZNLOCTEQ6L1
ZH	NNPDF23LO	Pythia 8	A14
W^+H	NNPDF23LO	Pythia 8	A14
W^-H	NNPDF23LO	Pythia 8	A14
ttH allhad	aMcAtNlo + NNPDF23LO	Pythia 8	A14
ttH semilep	aMcAtNlo + NNPDF23LO	Pythia 8	A14
ttH dilep	aMcAtNlo + NNPDF23LO	Pythia 8	A14

Table 3.3: Generators, PDFs, particle showering models and underlying-event models for the MC samples used.

Each sample contains 10^5 simulated $H \to K^*\gamma$ and $H/Z \to \omega\gamma$ events (with the exception of the ttH channels, which each contain $30,000$ events). Pythia 8 is used to decay the Higgs boson for all channels. The Z signal sample is produced with 0 jets at NLO.

3.4.3 Theoretical systematic uncertainties

The Higgs boson production cross sections, as well as their uncertainties, are taken from Refs. [78, 79, 80] and arise from the theoretical calculations of the Higgs boson processes at the NLO or NNLO level.

The QCD scale uncertainties on the cross-section for a 125 GeV H boson [80] amount to $+7\%$ and -8% for the ggF process, $\pm 0.4\%$ to $\pm 4\%$ for the VBF and associated WH/ZH production processes and $+6\%$ and -9% for the associated $t\bar{t}H$ production process.

The uncertainty on the production cross section due to uncertainties on the parton distribution functions (PDF) and the strong coupling constant, α_s, is $\pm 3.1\%$ for ggF processes, $\pm 2.1\%$ and $\pm 1.6\%$ for the VBF and associated WH/ZH production processes and $\pm 3.6\%$ for the associated $t\bar{t}H$ production process [80].

For the Z signal the production cross section as well as its uncertainty are taken from the measurement in Ref. [81], with an uncertainty of 5.5%. The value is obtained from measurements of the $Z \to e^+e^-$ and $Z \to \mu^+\mu^-$ channels, which are then used to extract the production cross section.

The above uncertainties are combined by summing in quadrature and weighting by cross-section contribution as 5% for the QCD uncertainties and 2.9% for the uncertainties on the production cross section, and these two numbers are included in the fitting procedure as nuisance parameters (described in Section 5.5).

CHAPTER 4

τ-lepton Algorithm Validation in the ATLAS High Level Trigger

The decays of the τ-lepton pose a challenge for reconstruction and identification within proton collisions, due to the relatively convoluted decay and jet-like final state. As such, triggering on these decays requires substantial efforts to disentangle potential τ-lepton decays from QCD backgrounds to keep interesting events. The triggers used in Run-2 must be validated for performance, which is described in the first part of this chapter. Looking ahead to Run-3 and beyond, potential improvements to the algorithms used are available through machine learning, which is described in the latter half of this chapter.

4.1 L1 τ-lepton trigger

The L1 τ-lepton trigger reconstructs relatively simplistic candidates for τ-leptons (known as $\tau_{had-vis}$ candidates) in events, based on calorimeter information. The algorithm has remained largely the same since Run-1, and is executed as follows. Two regions are defined for each candidate in the L1Calo trigger, using trigger towers in the EM and hadronic calorimeters - the core region, and an isolation region surrounding this core. The granularity of the trigger towers is $\Delta\eta \times \Delta\phi = 0.1 \times 0.1$ with a coverage of $|\eta| < 2.5$. The core region is defined as a square of 2×2 trigger towers, corresponding to 0.2×0.2 in $\Delta\eta \times \Delta\phi$ space. The isolation region surrounding this forms an annulus between 0.2×0.2 and 0.4×0.4 in $\Delta\eta \times \Delta\phi$ space. The E_T of a $\tau_{had-vis}$ candidate at L1 is the sum of the transverse energy in the two most energetic neighbouring central towers in the EM calorimeter core region, and in the 0.2×0.2 towers in the hadronic calorimeter.

For each $\tau_{had-vis}$ candidate, the EM isolation E_T^{EMisol} is calculated as the transverse energy in the annulus between 0.2×0.2 and 0.4×0.4 in the EM calorimeter. A cut on this variable is placed in order to supress background events, and thus reduce trigger rate. A cut of E_T^{EMisol} [GeV] $\leq \left(\frac{E_T}{10} + 2\right)$ is applied for $\tau_{had-vis}$ candidates up to 60 GeV. This requirement was tuned based on $\sqrt{s} = 13$TeV MC simulation to provide a selection efficiency of 98%. No isolation requirement is applied above

60 GeV.

Further improvements to the reconstruction of $\tau_{had-vis}$ candidates are performed using L1Topo topological algorithms, which achieve reductions in rate based on kinematic and geometric selections. Typically these algorithms apply an angular selection on L1 objects above given E_T thresholds. A selection of such algorithms is included based on target final states of interest.

4.2 HLT τ-lepton trigger

HLT algorithms for the τ trigger are based on the decay topology of the hadronic decays of the τ lepton [1]. τ-leptons decay hadronically, i.e. $\tau^- \rightarrow$hadrons, 65% of the time, and leptonically (e.g. $\tau^- \rightarrow \mu^-\nu_\mu\nu_\tau, e^-\nu_e\nu_\tau$) 35% of the time [1]. The proper decay length is 87.03±0.15 μm, the implication being that it decays typically before reaching the sensitive components of the detector, but it can travel a measurable distance from the collision vertex.

Accurate reconstruction of τ-lepton decays is necessary for a range of analyses. As mentioned previously, evidence for the $H \rightarrow \tau\tau$ decay was found [39], acting as a measurement of the strongest coupling of the SM Higgs boson to leptons. In many BSM models containing heavier or exotic Higgs bosons, a final state containing τ-leptons is preferred [82, 83, 84].

Hadronic decays of the τ-lepton, which are the focus of the following section, have a distinct topology. Being the only lepton capable of decaying hadronically through the weak interaction, there are a number of common hadronic decay modes, which are listed in table 4.1 (there are many more, however the branching ratios are sub-dominant). Importantly, every decay channel contains some undetectable component due to the neutrino, which must be present to conserve lepton number. The charged pions in the decay leave tracks in the tracking system, which can be used to determine the charge, and energy deposits in the calorimeters.

Decay products	Branching ratio (%)
$\pi^{\pm}\pi^{0}\nu_{\tau}$	25.52
$\pi^{\pm}\nu_{\tau}$	10.83
$\pi^{\pm}\pi^{0}\pi^{0}\nu_{\tau}$	9.3
$\pi^{\pm}\pi^{\pm}\pi^{\mp}\nu_{\tau}$	8.99
$\pi^{\pm}\pi^{\pm}\pi^{\mp}\pi^{0}\nu_{\tau}$	2.70
$\pi^{\pm}\pi^{0}\pi^{0}\pi^{0}\nu_{\tau}$	1.05

Table 4.1: Common hadronic decay modes of the τ-lepton.

The structure of the algorithm for identifying candidate τ-leptons within ATLAS in Run-2 is as follows [85].

Calorimeter-only preselection: The visible decay products of the τ-lepton (i.e. the pions) are reconstructed using only information available from the calorimeters. The L1 calorimeter cells are taken, and a topological clustering algorithm is executed, which attempts to identify the most likely combination of clusters which could act as a seed for a τ-lepton candidate based on geometry, but no clusters are rejected at this stage. The clusters are then calibrated using local hadron calibration (LC), which attempts to suppress noise, account for the different responses in the detector to pions and electrons, and correct for dead material. This results in a signal which is very similar to the offline values. The result from the topological clustering is then used as a 'jet seed' for the τ-lepton candidate. The candidate energy is measured within a cone of $\Delta R < 0.2$ around the jet seed. Following this, an energy calibration (TES) is then applied, specific to τ-lepton candidates. It uses kinematic variables such as the p_T and η of the candidate, and attempts to correct for pile-up and missing ν_{τ}. Finally, a cut is applied on the p_T of the candidate, and if it passes the cut then it is forwarded to the next stage.

Track preselection: Track information is now added to the previous calorimeter information using a two-stage 'fast tracking' procedure. First, a leading p_T track is sought in a narrow cone of $\Delta R < 0.2$ around the partially reconstructed candidate across the whole detector. Then, any further tracks are then fit in a larger cone of $0.2 < \Delta R < 0.4$, but in a tighter range around the leading track on the beam. This

defines two regions, an inner *core* region, and an outer *isolation* region, containing N_{core} and N_{isol} number of tracks respectively. Only candidates with $1 \leq N_{core} \leq 3$ and $0 \leq N_{isol} \leq 1$ are passed on to the final stage.

Offline-like selection: To finalise the identification of a τ-lepton candidate, a precision tracking algorithm is executed using the previously identified tracks. The information from this is used to compute a set of input variables for 1- and multi-prong candidates separately, which are passed to a Boosted Decision Tree (BDT). The BDT reduces the dimensionality of the input to a single number, or score, which can be used to discriminate real τ-leptons from background, and is tested and trained using simulated signal ($Z \rightarrow \tau\tau$) and background (QCD jets) samples. Various working points are defined based on the level of background rejection, and correspond to *tight*, *medium* and *loose* categories.

After these steps are complete, the candidate τ-leptons are passed through as final and kept within the event information.

There are a number of different triggers in the HLT which employ this algorithm, the main variations between them being a different cut on the p_T of the identified candidate, as well as the working point of the final BDT identification. The following is a representative list of the triggers which are used in the HLT trigger menu for identifying τ-leptons, all in the menu for 2017-2018:

- HLT_tau25_medium1_tracktwo, the trigger suffering from the inefficiency described in the next section.
- HLT_tau25_medium1_tracktwoEF, the trigger which attempts to solve the inefficiency of the previous trigger.
- HLT_tau25_(veryloose/loose/medium/tight)RNN_tracktwoMVA, an additional trigger building upon the previous one, including an RNN ID algorithm at various working points.

The nomenclature is explained as follows. `tau25` corresponds to a cut on the can-

didate p_T of 25 GeV, `medium1` corresponds to the medium BDT working point for the final τ identification, `tracktwo` defines the category of triggers with the pile-up inefficiency, `tracktwoEF` defines the category of triggers which attempt to solve the inefficiency, and `tracktwoMVA` defines the triggers which use a more advanced form of multivariate analysis to perform the identification.

The `tracktwoEF` and `tracktwoMVA` categories are defined in the next section.

4.3 Trigger inefficiency and solution

In Run-2 data taking within ATLAS, there were high levels of pile-up (on average approximately 36.1 interactions per bunch crossing) within the detector during physics data taking. One of the negative consequences of this is a reduction in the efficiency of the HLT algorithms to correctly identify τ-lepton candidates as pile-up increases.

This inefficiency is due to a larger number of non-τ-lepton-originating tracks. This increase in the number of background tracks results in the track preselection stage of the algorithm finding too many tracks falling within the cones, and therefore the cuts applied on N_{core} and N_{isol} cause a drop in the number of candidates correctly identified.

In order to correct for this, it was decided to remove the requirement on N_{core} and N_{isol} during the fast-tracking stage, and instead pass the information produced by the fast-tracking on to the precision tracking stage. After the more precise fitting is performed, then the requirements on the number of tracks is applied. By doing this, the negative effect of high pile-up on the signal efficiency could be mitigated. It was found that this imposed minimal requirements on the TDAQ system, and so was feasible to implement without degrading the performance of the TDAQ to any significant degree.

In addition to this, a further more ambitious set of triggers was constructed, using

a form of multivariate analysis known as a *Recurrent Neural Network* (RNN) [86] to perform the identification.

In order to validate the new trigger categories, the efficiency for correctly identifying τ-leptons in signal samples and the rejection of jet tracks as real τ-leptons requires investigation. In order to do this, a number of different signal and background MC simulation samples are used. This section shows a representative sample of the plots produced, using $Z \to \tau\tau$ samples for the signal, and Enhanced Minimum Bias[1] data for estimating background efficiencies.

The HLT efficiency is defined by taking the ratio of the number of events that pass the HLT trigger of interest with the number of events that pass the L1 trigger that seeds the same HLT trigger. As well as this, a veto is performed for events that fall in the 'crack' region ($1.37 < |\eta| < 1.52$) in the ATLAS detector between the barrel and the endcap. Distributions are then produced as a function of the mean number of interactions per bunch crossing (denoted μ), p_T and η of the tau candidate. The aim of these efficiency distributions is to show firstly that the signal efficiencies for the new trigger categories are more robust against pileup. The signal efficiency should not be lower for the new trigger categories compared to the original, and there should not be a significant increase in the background jet efficiency, as this would mitigate the improvement in the signal efficiency depending on the magnitude of the increase. Figures 4.1, 4.2 and 4.3 show such signal efficiency curves for a sample of 100,000 $\gamma^* \to \tau\tau$ events, with respect to pile-up, p_T, and η. Pile-up in the sample covers the range $\mu = 20$ to $\sim$70, which is roughly the range for the remainder of Run-2 data taking within ATLAS. The p_T range is chosen such that the 'turn-on' is clearly visible, i.e. the value of p_T at which the trigger is designed to accept events, and such that the plateau is clearly visible, at which point the signal efficiency levels off. The η range is chosen to cover the full range of the ATLAS detector. The RNN category of triggers use the 'medium' tau ID requirement.

[1]Enhanced Minimum Bias data is data collected by triggering at random, but placing high weights on events with high p_T as these are likely to be events of interest. This produces a compact dataset which can be used for assessing trigger rates.

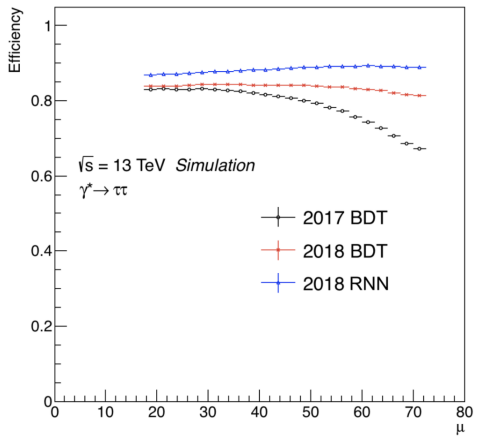

Figure 4.1: Signal efficiency against (μ).

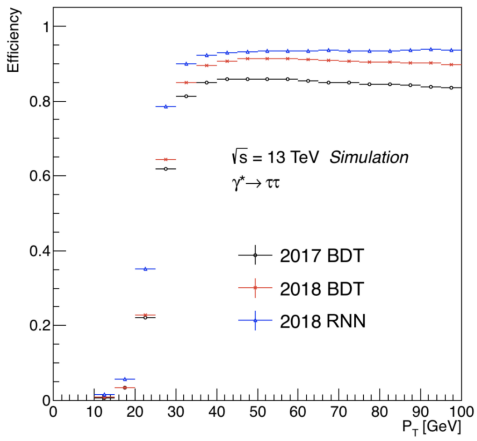

Figure 4.2: Signal efficiency against p_T.

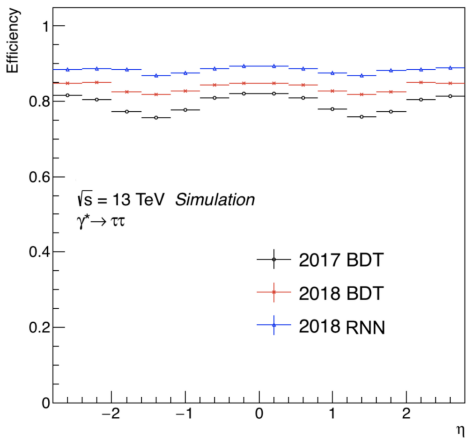

Figure 4.3: Signal efficiency against η.

Figure 4.1 demonstrates that the 2018 BDT and RNN trigger categories are more robust against pile-up and do not suffer the inefficiency of the 2017 BDT category. The RNN category has a marked increase in signal efficiency (∼4-5%) over the BDT category with respect to pile-up. This achieves the stated purpose of the new trigger strategy. Examination of the p_T efficiency curve shows that the turn-on is faster (rises from 10% - 90% of the plateau efficiency) and achieves a higher plateau efficiency in a manner similar to the pile-up efficiency plot. Finally the signal efficiency with respect to η demonstrates that the overall shape and flatness over the full range is maintained, and no unexpected behaviour is produced.

Figures 4.4 and 4.5 show the background efficiency with respect to p_T and η. Since these plots were produced with actual enhanced minimum bias data, the μ distribu-

tion depends on the variations in luminosity during the run in which the data was taken. For these plots, the value of μ did not vary by more than approximately 3, so this distribution does not add much information. However, as a first estimate of the background rates expected from these triggers, these plots are sufficient.

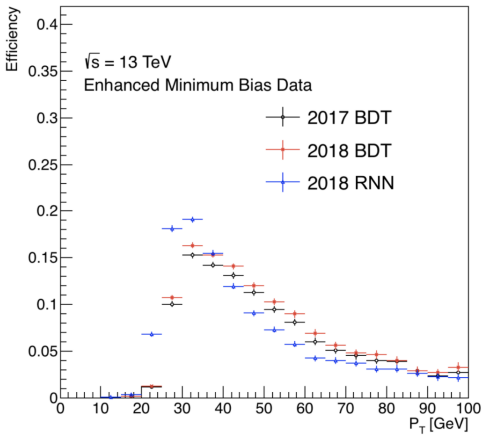

Figure 4.4: Background efficiency vs p_T.

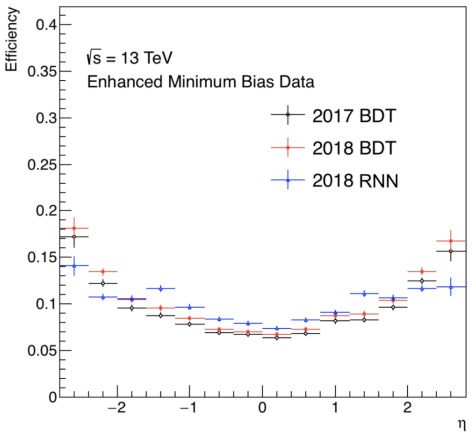

Figure 4.5: Background efficiency vs η.

The purpose for the background efficiency plots is to estimate any potential changes in the efficiency of the triggers to misidentify jet backgrounds as real τ-lepton candidates. Figures 4.4 and 4.5 show that the 2018 BDT category is comparable to the 2017 BDT category in terms of rates, with only a marginal increase. However the shape of the efficiency for the RNN category appears to be inconsistent with the BDT categories. A higher peak efficiency is followed by a lower tail efficiency at higher p_T compared to the BDT triggers. Integrating over all the events to get an idea of the rates gives an increase of $< 1\%$ between the 2017 and 2018 BDT categories, and a $\sim$4% increase between the 2018 BDT and RNN categories.

There are no major differences between the background efficiencies for the different trigger categories, when studied as a function of η and p_T. This, as well as the overall flatness of the trigger categories demonstrates that the rates with respect to η are not detrimental to the performance of the new triggers.

This is sufficient information to draw conclusions about the preliminary performance of the improved trigger categories, the validation of which is the foundation of the work described here.

- The 2018 BDT and RNN trigger categories are robust with pile-up when compared to the 2017 BDT category, as a result of the changes described at the start of this section.

- There is no detrimental signal efficiency performance for the new trigger categories as a function of p_T and η, with an increase of $\sim$4-5%.

- The background efficiency for misidentifying tracks from jets as true tracks from hadronically decaying τ-lepton tracks is increased for the 2018 categories when compared to the 2017 categories. However, the increase is not high enough to be detrimental. When put into the context of physics analysis, in particular the search for a new particle, the significance is defined as $S/\sqrt{B}$, where S is the number of signal events, and B is the number of background events. Since the magnitude of the increase in the background is on a comparable level to the signal, the significance is expected to increase. Background levels are typically very reducible in analyses, and this further enforces the fact that the new triggers have an improved performance.

In order to further validate the performance of these triggers, it would be useful to obtain dedicated MC samples to investigate the background rates. Often, simulated dijet samples are used to estimate the expected background efficiencies. To conclude the results from validation of the new 2018 BDT and RNN trigger categories, the initial goal of increasing the robustness of the triggers to high pile-up conditions has been achieved. The new trigger categories are performing as expected when taking data online in nominal ATLAS data-taking conditions, and further validation is expected using simulated MC samples for dijet backgrounds.

4.4 Further improvements to HLT hadronic τ-lepton algorithms

Since the initial inefficiency of the triggers with pile-up was constrained to the second track-finding stage of the HLT algorithm, there is an interest in developing a better

way to perform this stage. A promising alternative comes in the form of an RNN, which has been mentioned previously. RNNs have been previously demonstrated to improve other stages of the τ HLT algorithm such as identification. The RNN would perform the classification of the τ-lepton tracks, removing the need for the inefficient cut. The development of this is currently underway, and the aim is to have this in place for Run-3 data taking.

4.5 HLT τ-lepton track classification with an RNN

Recurrent neural networks using Long Short-term memory (LSTM) [87] have been proven very useful in tackling many challenges in high energy physics, having been adapted from wider uses in language processing [88], time-series analysis [89], and translation [90].

The basic principle of an neural network is modelled upon biological neurons, connected to form complex structures capable of identifying dependencies and making predictions from datasets. Artificial neurons (or cells) containing state vectors are connected in a series of layers, where a connection is modelled as weights. Positive and negative weights determine the amplitude of the output of each cell, controlled by an activation function (often normalised to be between 0 and 1 or -1 and 1). Propagating input variables through the network reduces the initial series of arbitrary length to a fixed dimensional representation of the entire sequence.

Recurrent neural networks extend the idea to allow representation of the initial sequence as a time series, allowing longer term dependencies to be determined. A representation of an RNN is shown in Fig 4.6.

A particular architecture for an RNN was shown to have promise in preliminary studies for an offline environment (still currently a work in progress), and is being adapted for use in the HLT algorithm. The Keras [91], Theano [92] and TensorFlow [93] packages are used for the training and testing of the network.

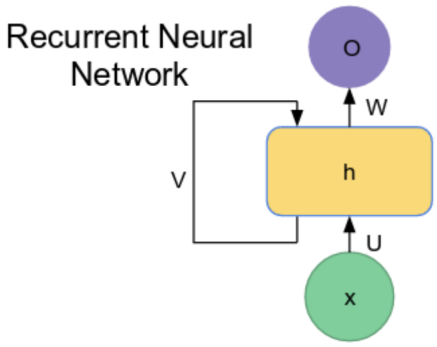

Figure 4.6: A representation of an RNN. A standard feed-forward neural network is shown, taking input x, passing through to the hidden layers (h) for processing, and producing output o. The inclusion of the loop V then creates the recurrency.

The details of each layer in the architecture will not be discussed here, however it is important to motivate some of the features. LSTM layers were chosen since they allow longer term dependencies to be incorporated through a more complex internal cell structure. Longer term dependencies, traditionally referring to time-series, in this instance take the form of multiple tracks in a system; that is, the effect of a particular track on the system as a whole is taken into account by treating each track as a "time step". Initially, the full set of tracks in the system are given to the RNN input. There are two "branches" to the network, splitting after the $lstm\_2$ layer. The left branch attempts to classify the tracks into four separate categories: Tau tracks (TT), Conversion tracks (CT), Fake tracks (FT) and Isolation tracks (IT). Tau tracks are those directly from the τ-lepton decay. Conversion tracks are due to photon conversions resulting in e^+e^- pairs. Fake tracks are those that are a result of actual tracks resulting from pile-up in the detector, or from hits in the trackers that fake tracks. Isolation tracks are those from the underlying event. The right branch attempts to classify the track as being from a τ-lepton decay, or from the QCD background. The output is created using the $softmax$ function, which normalises the output to be between 0 and 1, allowing the result to be interpreted as a probability. The form of the output is 4 scores for the left branch, and 2 scores for the right branch. The largest score is taken as being the classification for that track.

Variable	Description
log(track p_T)	The logarithm of the track p_T
log(jet seed p_T)	The logarithm of the jet seed p_T
log(track p_T/jet Seed p_T)	The logarithm of the ratio of the track p_T to jet seed p_T
track η	The η of the track
z0sinThetaTJVA	Longitudinal impact parameter multiplied by the sinθ of the track
rConv	Distance from the vertex to the beamline in the transverse plane
rConvII	Same as rConv but taking into account the impact parameter, d0
dRJetSeedAxis	ΔR between the jet seed axis and the τ-lepton candidate track
d0	Impact parameter, defined as the transverse distance to the beamline
qOverp	Ratio of the reconstructed charge to the track momentum
Innermost pixel layer hits	Hits from tracks in the innermost pixel layer
Pixel shared hits	Shared hits in the pixel layer
SCT shared hits	Shared hits in the SCT layer
TRT hits	Hits from tracks in the TRT layer
Pixel hits	Hits from tracks in the pixel layer
Si hits	Hits from tracks in the silicon layer
Charge	Charge of the track

Table 4.2: Variables used to train the RNN.

Training the network is done by taking a set of input variables from the events, which then feed into the updated values of the weights in the network. The list of variables is given in Table 4.2.

This set of variables was chosen based on previous studies using different multivariate techniques, however it is being studied as to whether this list of variables is necessary or optimal in this context. As such, it is important to note that this configuration and the results presented are in the context of offline studies, rather than what will actually be used during data taking (online). With sufficient reproduction of the offline results, it can then be adapted for online usage. Each iteration (or epoch) of the training updates the weights once. For memory and processing limitations, the number of tracks resulting from a τ-lepton decay considered in the training is limited to 20.

The network is trained on a set of 350k $\gamma^* \rightarrow \tau\tau$ events for signal, and a background set of 350k dijet events. The training is performed for 20 epochs. The output of this is a trained network, which can be applied to new sets of data to see the performance. The classification performance of the network is benchmarked by comparing to the

truth labels for the tracks in the simulated data. In this way, one can measure the efficiency of identifying the track types with respect to variables such as p_T and μ.

Applying the trained network to a MC sample of signal $\gamma^* \rightarrow \tau\tau$ yields the efficiency distributions in Fig 4.7, with respect to the reconstructed τ-lepton p_T. The efficiencies again are defined in terms of ratios, where the denominator for all lines is the number of truth 1- and 3-prong tracks that are TT. The numerator for the green line is the number of true TT associated to a τ-lepton decay (i.e. the best efficiency that an algorithm can hope to achieve). The red line corresponds to where the RNN classifies these tracks as TT, rather than the other three categories. The black line corresponds to a previous effort to achieve this, using another form of multivariate analysis called a Boosted Decision Tree (BDT) - however, previous studies have shown that the RNN outperforms this. These are then split into 1- and 3-p decays. The efficiencies shown in this document are a work in progress, and are attempts at recreating this performance so that the configuration can be adapted for use online in the HLT during data taking in Run-3.

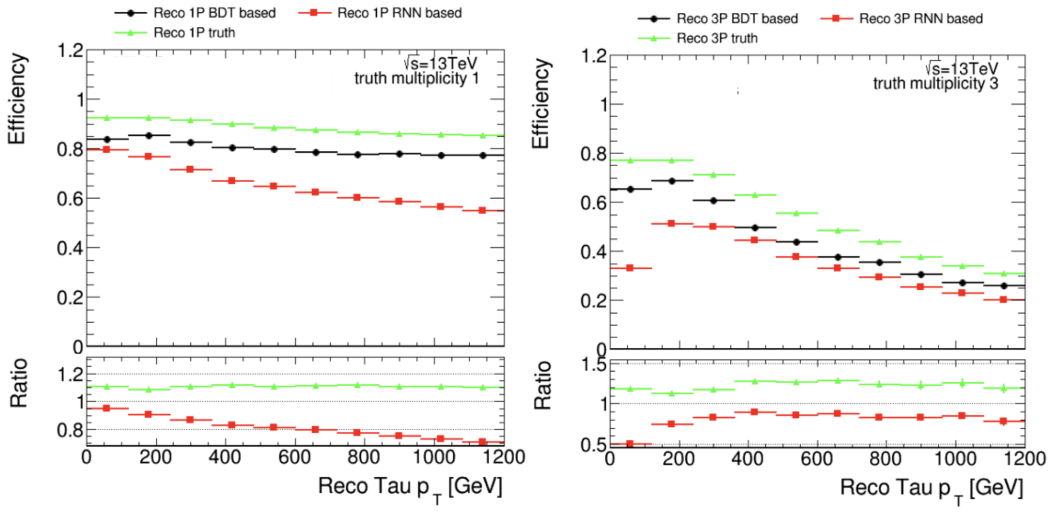

((a)) ((b))

Figure 4.7: Classification efficiency for (a) 1-prong and (b) 3-prong τ-lepton decays with respect to the reconstructed τ-lepton p_T.

The efficiency plots produced show a poorer performance overall for identifying TT in a signal sample using the RNN when compared to a previous BDT effort. This is not a complete picture however, as the performance with background rejection

must also be determined before a more definitive statement can be made on the performance. The next steps in the development of the RNN are as follows:

- The poor efficiency compared to the BDT must be explained. Current efforts are concluding that it is more likely to be an issue in the setup, rather than anything conceptually wrong.
- The importance of the input variables will be determined. By examining the correlation between the input variable and the output score from the RNN, the variables can be ranked in terms of impact on the RNN training.
- The RNN performance for background rejection must be determined.
- The environment will be adapted to run online during data taking. This will involve possibly changing the input variables, and adapting the data formats to use those that are prevalent in the HLT.

Development of the RNN will continue, with the goal of implementing it in the HLT τ-lepton algorithm for Run-3.

To conclude, the validation of HLT τ-lepton triggers in Run-2 was performed in order to confirm appropriate rates of background rejection and signal acceptance. Looking ahead, improvements to the τ-lepton track reconstruction algorithms for Run-3 are underway, making use of appropriate machine learning techniques.

CHAPTER 5

Search for the decay $H \to K^*\gamma$

The Higgs boson decay $H \to K^*\,\gamma$ offers an opportunity to access the down/strange-quark Yukawa couplings [56]. This decay has a very small predicted Standard Model (SM) branching ratio, arising from loop-contributions (shown in Fig 5.1), with a value of $\mathcal{B}(H \to ds) = 1.19 \times 10^{-11}$ [94], which represents a conservative upper bound on a SM value for $\mathcal{B}(H \to K^*\gamma)$. Any observation of this process would likely imply BSM effects, given the magnitude of the branching ratio. This is the first exclusive decay analysis to target flavour-changing interactions of the Higgs boson.

We perform a search for the decays of the Higgs boson to $K^*\,\gamma$ using the ATLAS 2016, 2017 and 2018 pp dataset collected at a centre-of-mass ($\sqrt{s}$) energy of $\sqrt{s} =$ 13 TeV. The analysis is performed by exclusively reconstructing the decay $K^* \to K^+\pi^-$. The branching fraction for $K^* \to K^+\pi^-$ decays is $\mathcal{B}\,(K^* \to K^+\pi^-) \approx 100\%$, $m_{K^*} = 895.81 \pm 0.19$ MeV [1].The analysis will exploit the distinctive $H \to K^*\gamma \to K^+\pi^-\gamma$ topology of a pair of oppositely-charged, high p_{T} isolated tracks, with a very

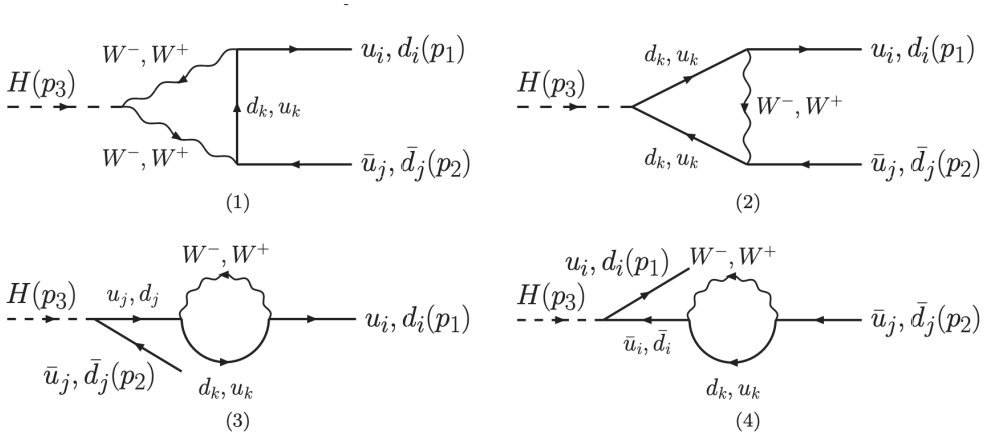

Figure 5.1: The $H \to u_i u_j$ decay with $u_i u_j = u\bar{c} + \bar{u}c$ and $d_k = d, s, b$ and $H \to d_i d_j$ decay with $d_i d_j = d\bar{s} + \bar{d}s, d\bar{b} + \bar{d}b, s\bar{b} + \bar{s}b$ and $u_k = u, c, t$ [19].

small opening angle ($\Delta R < 0.05$), recoiling against a hard isolated photon.

No calculation is available for the analogous Z boson decay to $K^*\gamma$, as this would violate the conservation of angular momentum due to the flavour-violating nature of the decay.

Until the analysis selection was frozen, the analysis was blinded, removing events satisfying 120 GeV $< m_H <$ 130 GeV.

5.1 Event Selection

The following dedicated triggers were activated during the 13 TeV data collection for this analysis:

- `HLT_g35_medium_tau25_kaonpi1_tracktwo_L1TAU12`
- `HLT_g25_medium_L1EM24VHI_tau25_kaonpi1_tracktwo_50mVis10000`

These triggers are a combination of a photon and tau trigger including an invariant mass requirement where the standard tau variables have been modified to select two

tracks consistent with a $K^* \to K^+\pi^-$ decay, instead of the nominal 1- or 3-prong tau objects.

The following selection is in part motivated by the kinematic distributions given in Section 2.6. In order to select $K^* \to K^+\pi^-$ decays of interest, firstly tracks are required to satisfy the Tracking CP group "Loose" quality. The tracks must be of opposite charge, as well as satisfying $|\eta^{K\pi}| < 2.5$. Both tracks must have $p_{\mathrm{T}}^{K\pi} > 15$ GeV, and one must have at least $p_{\mathrm{T}}^{K\pi} > 20$ GeV. The invariant mass of the di-track system must satisfy 792 MeV$< m_{K^+\pi^-} <$992 MeV. The sum of the p_{T} of the reconstructed ID tracks within $\Delta R < 0.2$ of the leading track candidate for tracks with $p_{\mathrm{T}} > 0.5$ GeV and $|\Delta z^0_{\mathrm{PV}}| < 1.5$mm must be less than 6% of the K^* candidate p_{T}. Finally, the best di-track pair is chosen based on the proximity to the K^* mass.

Photons need to fulfil the "tight" identification criteria [6] to ensure high-quality reconstructed photons. Their reconstructed pseudorapidity must be within $|\eta_\gamma| < 2.37$ and outside of the "crack" region of $1.37 < |\eta_\gamma| < 1.52$, as well as having $p_T^\gamma > 35$ GeV. In order to mitigate contamination from jets, the "`FixedCutTight`" photon isolation working point [95] is used[1].

Tracks are assigned a particular mass hypothesis by calculating the invariant mass of the di-track system for both possible assignments (K/π or π/K). The combination which results in the closest invariant mass to m_{K^*} is chosen. Alternative methods for track assignment were considered - either assigning the highest p_{T} track to be the kaon, or a random assignment (used primarily to confirm the effectiveness of the chosen track assignment method). The method which provided the narrowest resolution of the reconstructed m_{K^*} peak when compared to truth-matched K^* candidates was the invariant mass method.

$K^* \to K\pi$ candidates and photons, that satisfy the criteria discussed above, are paired to form loose $K^*\gamma \to K\pi\gamma$ candidates. These loose candidates are retained for further analysis if the difference in azimuthal angle between the $K^* \to K\pi$

[1] For photon track isolation $\Delta R < 0.2$ and only tracks with $p_{\mathrm{T}} > 1$ GeV are used

candidate and photon satisfies $\Delta\phi(K^*\gamma) > \pi/2$.

Finally, for validation and cross-checking purposes, a sideband region is defined. This dataset applies the same selection criteria listed above, but with the exception of an invariant mass requirement of $m_{K^+\pi^-}$ <792 MeV and $m_{K^+\pi^-}$ >992 MeV, essentially taking all events outside of the SR mass window. This provides sufficient statistics in the dataset, as well as a representative sample of the background.

A number of regions are defined in the analysis selection. Firstly, a loose selection excluding the isolation requirements on both the photon and tracks is defined, named the "GR", or Generation Region. From this, three validation regions are defined, each applying a single requirement on top of the GR level selection. "VR1" applies the ditrack isolation, "VR2a" applies the calorimeter component of the "FixedCutTight" photon isolation working point, and "VR2b" which applies the track component of the "FixedCutTight" photon isolation working point. These three validation regions are only used to derive and validate the background model.

The defined regions are summarised in Table 6.1.

Region		Cut	
GR	-	-	-
VR1	K^* Isolation < 0.2	-	-
VR2a	-	Photon Fixed Cut Tight (Calo)	-
VR2b	-	-	Photon Fixed Cut Tight (Track)
SR	K^* Isolation < 0.2	Photon Fixed Cut Tight (Calo)	Photon Fixed Cut Tight (Track)

Table 5.1: Definition of the various regions used. The selection is defined with respect to the basic GR selection.

The PDF in $m_{K\pi\gamma}$ for signal events is determined using simulation. For the Higgs boson the sum of two Gaussians with a common mean is used, shown in Fig 5.2. Two separate Gaussians are used in order to model both the peak and the tails well. All Higgs production modes listed in the MC samples are used as events for the signal modelling, weighted by cross section. The cut flow for MC and data is given in Tables 5.2 and 5.3. Generator level distributions for the reconstructed objects required by the trigger are given in Appendix B.

Table 5.2: Cut Flow in signal MC and data, assuming SM values for branching ratios and production cross-sections. Event yields for all cut stages are below 0.005 for the ttH dilepton sample.

	Signal								**Data**
	ggF	VBF	W^-H	W^+H	ZH	ttH allhad	ttH semilep	ttH dilep	
Starting events	6.82	0.52	0.03	0.04	0.04	0.01	0.01	0.00	1.57×10^7
Passed Trigger	6.80	0.52	0.03	0.04	0.04	0.01	0.01	0.00	1.57×10^7
γ:- tight, p_T/η req.	3.55	0.29	0.01	0.02	0.02	0.01	0.01	0.00	3.08×10^6
Trk:- loose, p_T/η req.	2.70	0.24	0.01	0.01	0.01	0.01	0.01	0.00	2.72×10^6
K^* mass window	2.70	0.24	0.01	0.01	0.01	0.01	0.01	0.00	2.72×10^6
$\Delta\phi(K^*\gamma) > \pi/2$	2.27	0.24	0.00	0.00	0.00	0.01	0.01	0.00	1.57×10^6
Pass GR	2.03	0.17	0.00	0.00	0.00	0.00	0.00	0.00	568 073
Pass SR	1.91	0.15	0.00	0.00	0.00	0.00	0.00	0.00	395 798

Table 5.3: Cut Flow in signal MC and data, assuming SM values for branching ratios and production cross-sections. The percentage value is relative to the starting total number.

	Signal								**Data**
	ggF	VBF	W^-H	W^+H	ZH	ttH allhad	ttH semilep	ttH dilep	
Starting events	100	100	100	100	100	100	100	100	100
Passed Trigger	99.58	99.66	99.79	99.80	99.67	100	100	100	100.00
γ:- tight, p_T/η req.	51.99	56.09	49.52	46.52	46.20	68.40	68.86	69.32	19.59
Trk:- loose, p_T/η req.	39.56	46.23	28.90	27.13	28.82	63.17	59.98	50.57	17.31
K^* mass window	39.56	46.23	28.90	27.13	28.82	63.17	59.98	50.57	17.31
$\Delta\phi(K^*\gamma) > \pi/2$	33.27	45.11	0.70	0.65	0.57	0.29	0.34	0.30	4.35
Pass GR	29.69	31.68	0.39	0.49	0.44	0.15	0.24	0.19	3.61
Pass SR	28.01	28.56	0.34	0.37	0.33	0.14	0.18	0.15	2.52

5.2 Selection optimisation procedure

The requirements presented in the previous section in general are defined by the acceptance of the ATLAS detector and the underlying reconstruction techniques. However, certain variables such as $p_T^{K^+\pi^-}$, p_T^{γ} and the isolation on the meson tracks have the potential to be varied in order to optimise the selection. This optimisation is performed by a simple calculation of $S/\sqrt{B}$ in the blinded mass window range using the simulated signal and the derived background model. Significance scans are then performed by varying the variable of interest to calculate the value which maximises the significance. It was found that there was no additional benefit to increasing the value of the cut on either $p_T^{K^+\pi^-}$ or p_T^{γ}, and an optimal value for the K^* isolation was found to be 0.2.

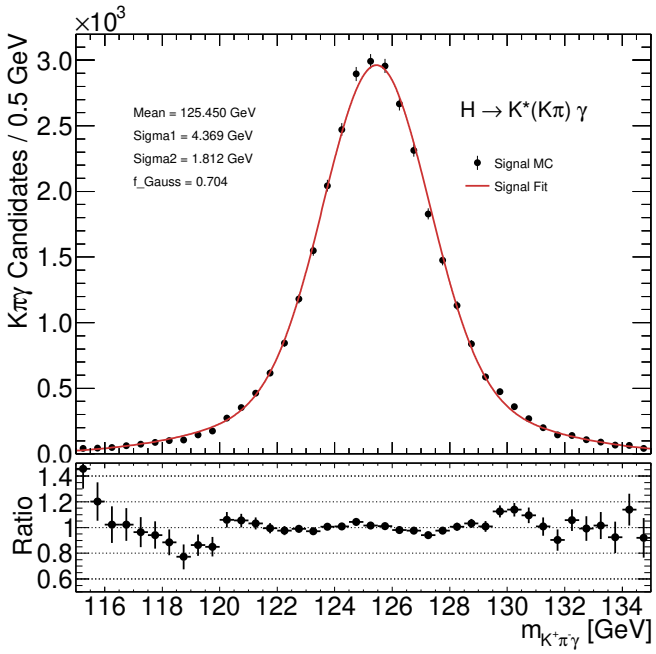

Figure 5.2: The $m_{K^+\pi^-\gamma}$ distribution model for the Higgs boson. For the Higgs mass distribution a double Gaussian function is used, where `Sigma1` and `Sigma2` are the width of the two Gaussians respectively and `f_gauss` is the fraction of the first Gaussian.

5.3 Background Modelling

For the analyses presented, the contributing background processes are difficult to model with MC simulation due to the complexity of the final states involved. The main backgrounds contributing are dijet production processes and γ plus jet production processes, in which a candidate for the K^* meson is reconstructed within a jet due to the similarity of the meson decay and a jet signature. In order to model these backgrounds, a data-driven non-parametric background model is used. This background model has been used successfully in previous analyses such as $H \to (\rho,\ \phi,\ \psi(nS),\ \Upsilon(nS))\gamma$ [4, 5, 63, 64].

5.3.1 Background Modelling Methods

The non-parametric data-driven background model relies on generating $K^*\gamma \rightarrow K^+\pi^-\gamma$ pseudo-candidates. This is achieved by loosening the isolation requirements on the $K^*\gamma \rightarrow K^+\pi^-\gamma$ candidates in the signal region to form a collection of loose data candidates (the GR region) in which the background processes will contribute far more than any signal to the statistics of the sample. The distributions of certain kinematic and isolation variables of these GR candidates are then sampled in a particular sequence based on the strength of the correlation between variables in data in order to generate the pseudo-candidates, which then have the full SR selection requirements applied. This resultant sample is then a usable representation of the background that remains following the full selection procedure. The various validation regions can also be applied at this stage, corresponding to individual isolation requirements.

The choice of the order of the sampling within the background model is based on the correlation matrices shown in Fig 5.4. For each step of the model, the decision was chosen to create histograms based on the strength of the correlation - however, it is sometimes the case that a correlation is not modelled even if a strong correlation exists between two variables, if one of those variables has multiple correlations with other variables. The binning of the histograms and the order of the sampling results in the final modelling of the SR $m_{K\pi\gamma}$ distribution, which is the variable of interest in the fitting procedure.

The background model configuration is shown in Fig 5.3. The motivation for each stage is determined by the correlations shown in Fig 5.4. The procedure is as follows:

i) Initially, values for $p_{\mathrm{T}}^{\mathcal{M}}$ and p_{T}^{γ} are sampled from a 2D histogram of ($p_{\mathrm{T}}^{\mathcal{M}}$, p_{T}^{γ}) from the sample of data, since they have the largest correlation in data (32%). The values of the meson mass, $\eta_{\mathcal{M}}$ and the ϕ angle of the meson are sampled from 1D histograms of the variables from the data sample. 1D histograms are used since these variables are not considered in the correlation matrices.

ii) The relative photon calorimeter isolation variable is sampled from a 2D histogram, distributed in bins of p_{T}^{γ}, given the large 29% correlation. Then the $\mathcal{M}$ isolation distribution is then sampled from a 3D histogram in which the $\mathcal{M}$ isolation is distributed in bins of $p_{\mathrm{T}}^{\mathcal{M}}$ and p_{T}^{γ}, where the value chosen is based on the values of $p_{\mathrm{T}}^{\mathcal{M}}$ and p_{T}^{γ} sampled in the previous step. This is motivated by the correlation between the $\mathcal{M}$ isolation and p_{T}^{γ}, and also the physical motivation that the $\mathcal{M}$ isolation should in some way be correlated to $p_{\mathrm{T}}^{\mathcal{M}}$, even if the correlation is weak in the correlation matrix.

iii) From the value of the relative photon calorimeter isolation drawn in the previous step, the values of $\Delta\eta(\mathcal{M},\gamma)$ and relative photon track isolation are sampled simultaneously from a 3D histogram, since all three variables show a correlation in the data with each other - particularly the two isolation variables.

iv) The value of $\Delta\phi(\mathcal{M},\gamma)$ is sampled from a 2D histogram, distributed in bins of $\Delta\eta(\mathcal{M},\gamma)$.

v) Given these sampled values, and the values sampled previously for $\Delta\eta(\mathcal{M},\gamma)$ and $\Delta\phi(\mathcal{M},\gamma)$, the values of $\eta_{\mathcal{M}}$ and ϕ_{γ} are then defined by summing.

Following the sampling procedure to generate the pseudo-candidates, the entire sample is weighted in order to match the loose data sample normalisation. Before unblinding occured, this was done by using the events observed in the $K^*\gamma$ mass distribution in the model to get the expected normalisation. Since the normalisation is applied on the loose sample, before the final isolation selection requirements are applied, this sample has the benefit of describing the background normalisation. This is a useful validation of the consistency of the model, however this information is not used in the final fitting procedure as the background normalisation is left as a free-floating parameter.

The background template used in the statistical procedure described in the next section is generated by using a Kernel Density Estimation (KDE) of the SR pseudo-candidate sample m_H distribution. KDEs are a non-parametric method used to

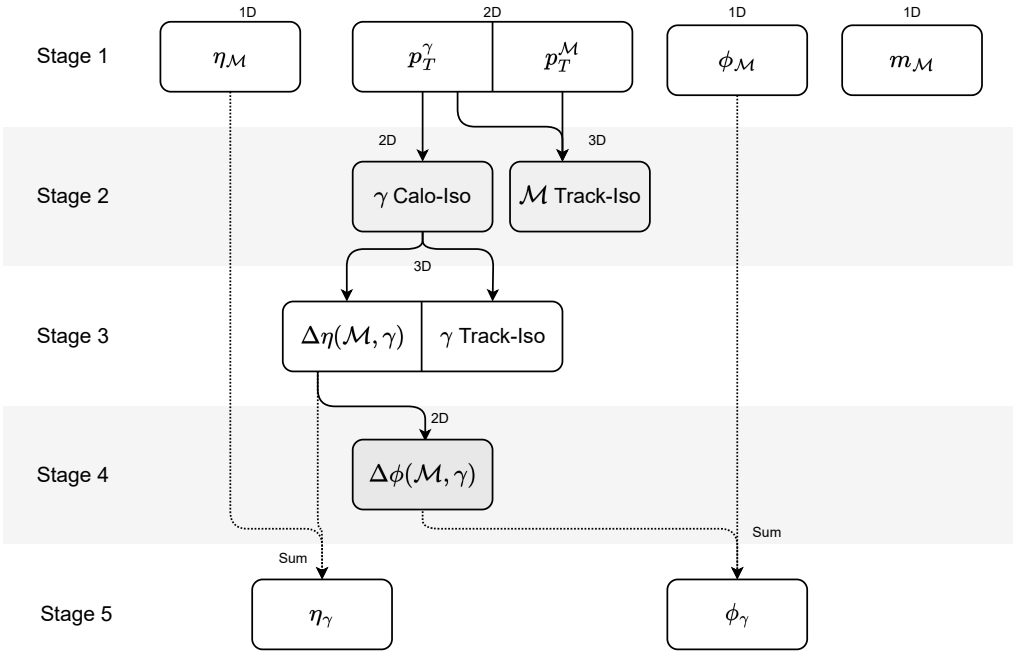

Figure 5.3: Background model procedure.

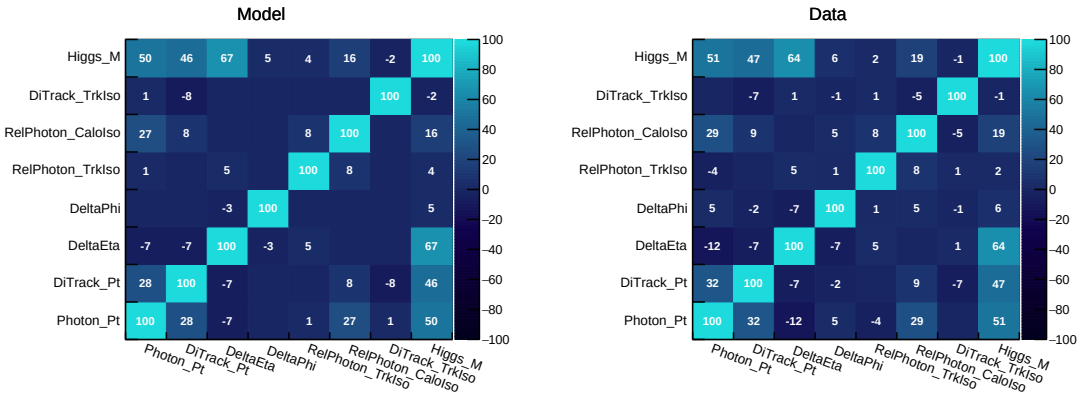

Figure 5.4: Correlation matrices showing the linear correlations between modelled variables in the background modelling, for the model (left) and the data (right), in the SR region.

estimate the probability density function of a random variable, using an optimised function (Gaussian, in this case) as a 'kernel', or weight. The optimisation is performed qualitatively, such that no visible bumps or features are visible in the resulting KDE template, and the kernel still describes the data well.

Validation of the background model using signal injections was performed, and is

detailed in Appendix E. The background model performs well and does not deviate significantly when very large signals are injected into the dataset.

It is noted that there are mis-modellings present in some of the variables, particularly the p_{T}-spectra, in the VR2a/b validation regions due to the background model's inability to capture every possible correlation in the data. Earlier studies have demonstrated that mis-modellings on these variables have little effect on the modelling of the three-body mass distribution. The modelling of the $m_{K\pi\gamma}$ distribution, which is the important distribution for the likelihood fit, in VR2a/b is good, and as such these mis-modellings are not considered to be detrimental in any significant way to the final performance of the fit. Regardless, systematics are assigned to cover these mis-modellings, as described in the next section.

Plots showing the distributions of relevant kinematic variables for the GR, VRs and SR are given in Figs 5.5 - 5.8. The plots demonstrate a good agreement between the data and the background model, in particular for the distribution of $m_{K\pi\gamma}$ which is the only variable used in the final fitting procedure.

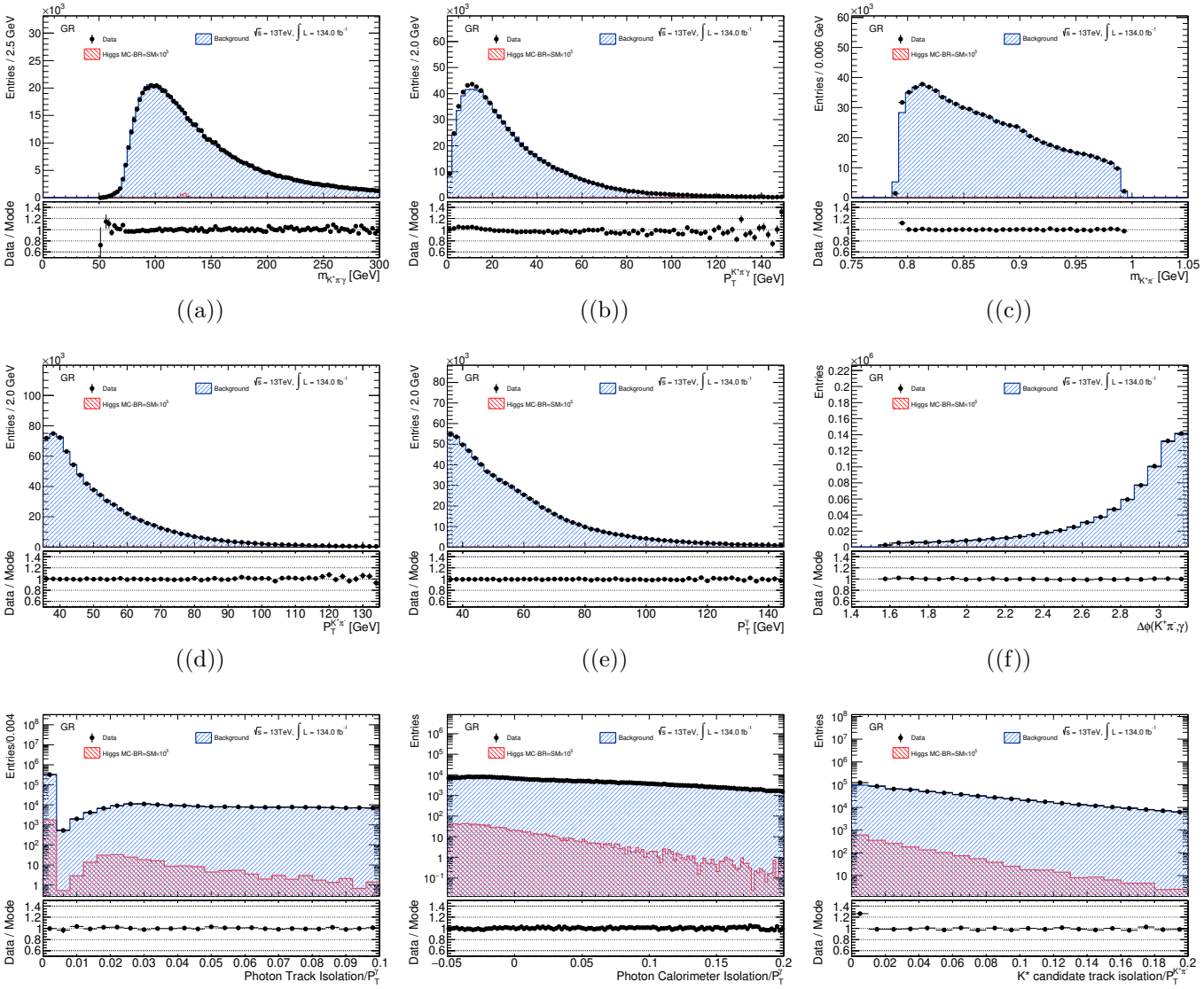

Figure 5.5: GR distributions of the background model.

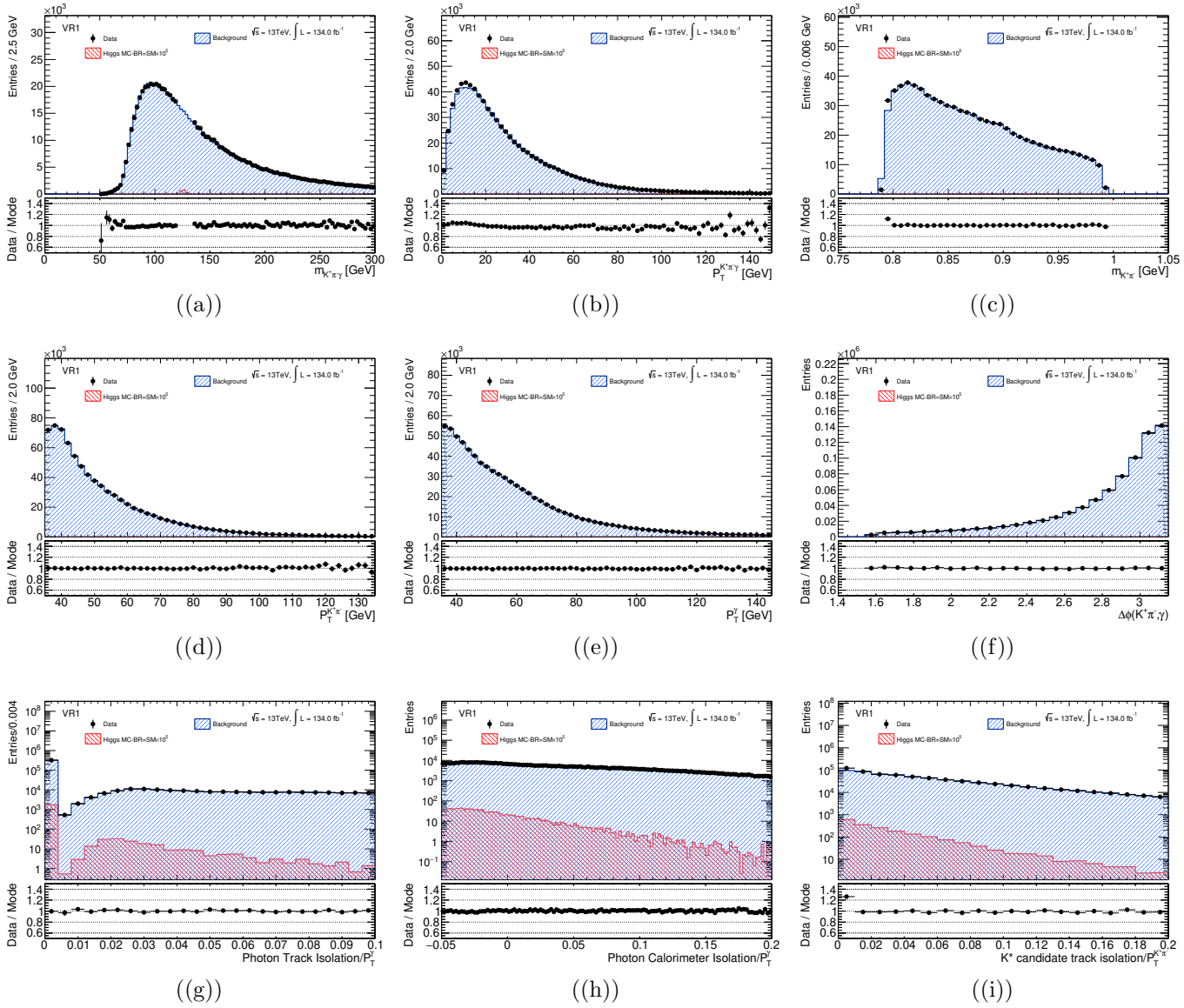

((a)) ((b)) ((c))

((d)) ((e)) ((f))

((g)) ((h)) ((i))

Figure 5.6: VR1 distributions of the background model, applying the meson track isolation requirement.

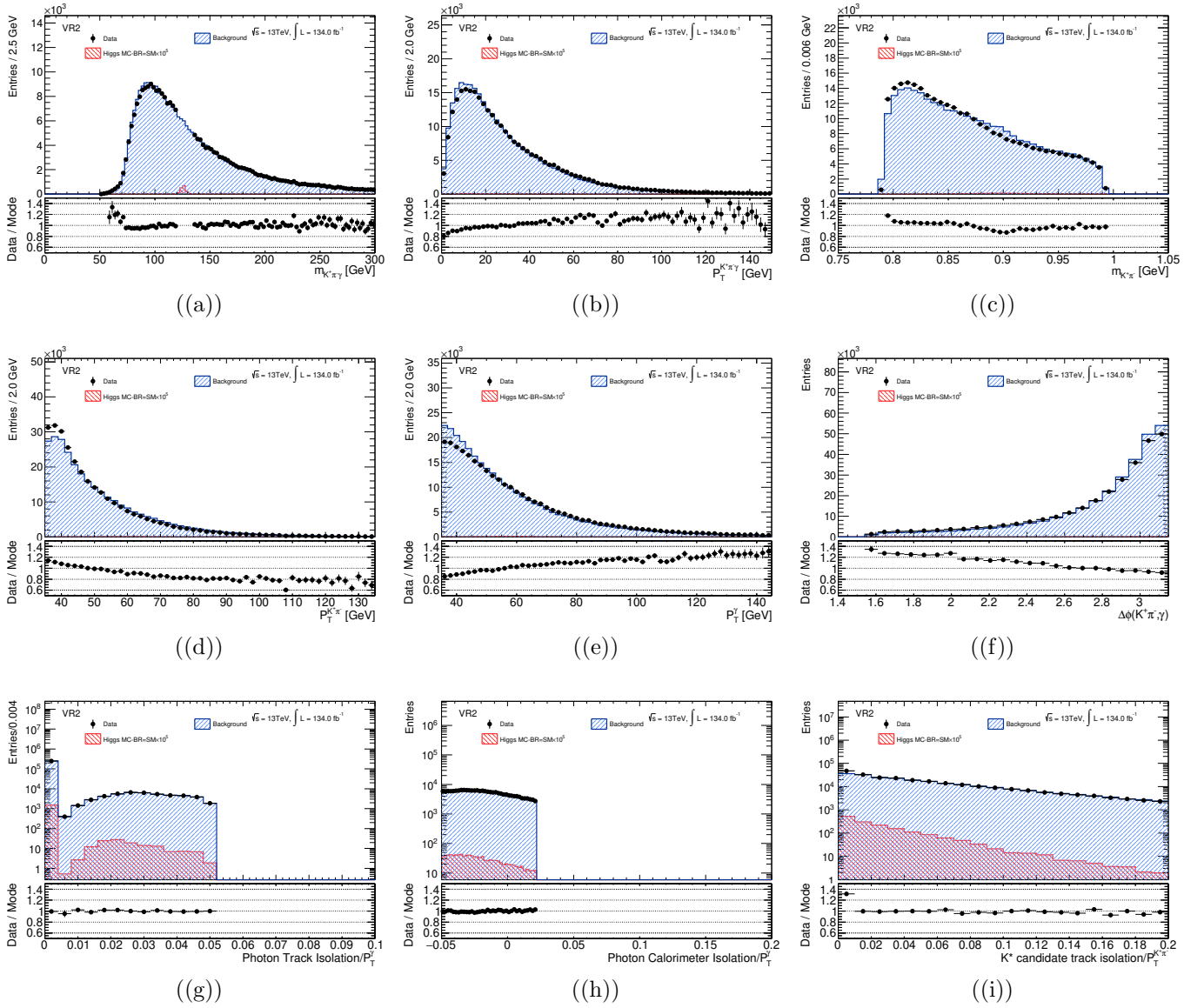

Figure 5.7: VR2 distributions of the background model, applying the photon calorimeter isolation requirement.

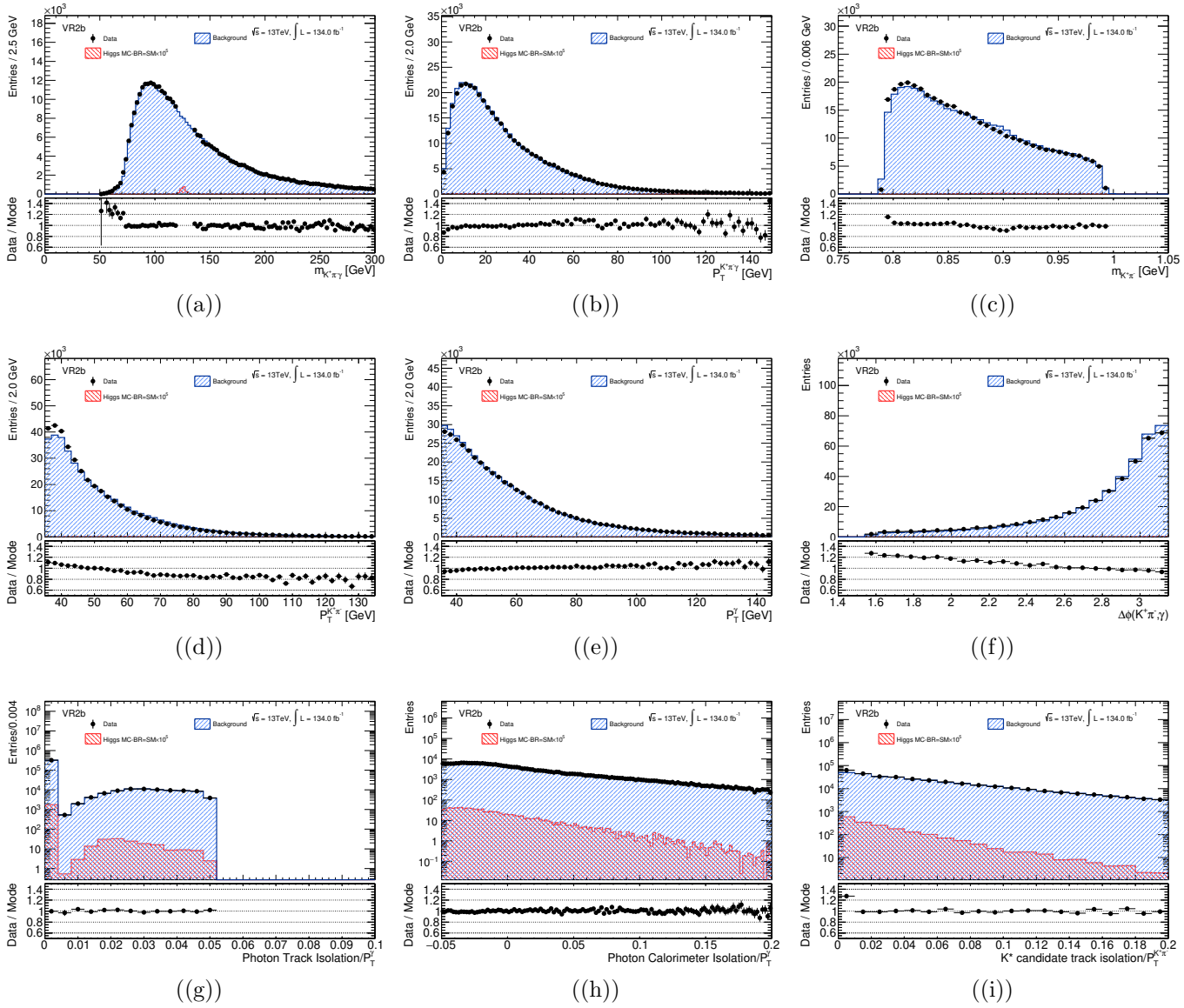

((a)) ((b)) ((c))

((d)) ((e)) ((f))

((g)) ((h)) ((i))

Figure 5.8: VR2b distributions of the background model, applying the photon track isolation requirement.

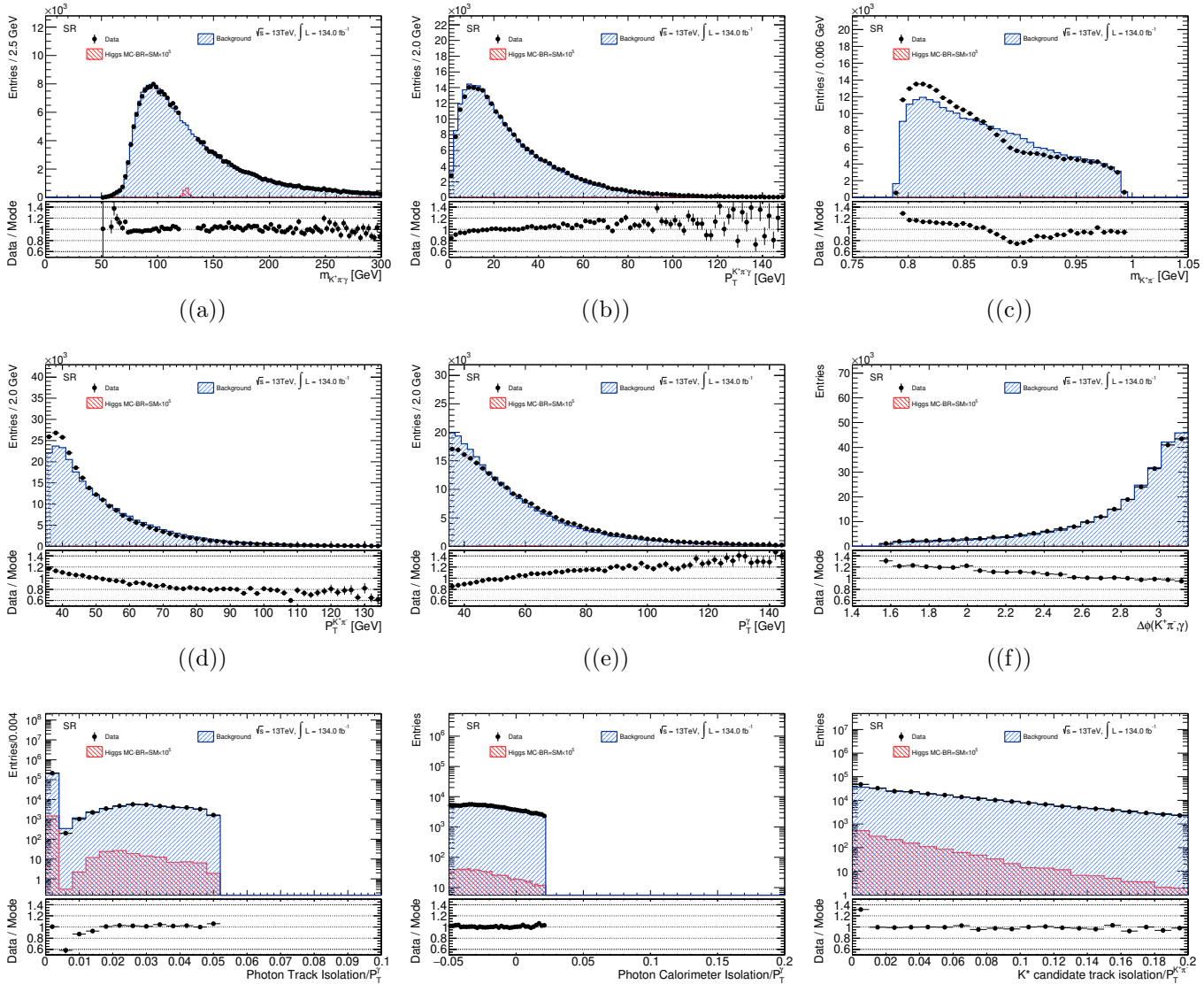

Figure 5.9: SR distributions of the background model, applying the full selection.

5.4 Background Model Validation with Shape Systematics

There is an associated uncertainty in the shape of the background model KDE generated from the procedure described in the previous section. In order to allow some freedom in the fit to account for any residual discrepancy between the KDE and the observed background distribution in data, the background model is altered to define different shapes. This is achieved through either generating entirely new background models in which the kinematics are modified, or by taking the nominal background model and re-weighting it to change the shape.

There are 3 separate systematics defined to account for the variations in the background model.

$p_{\mathrm{T}}^{K\pi}$ - shift This is an alternative model which is generated in the same way as the nominal, however the $p_{\mathrm{T}}^{K\pi}$ distribution used in the generation of the model is modified by either adding or subtracting 5 GeV. This variation results in a shift which is taken to be an effective $\pm 5\sigma$ boundary of the nuisance parameter included in the final likelihood fit, motivated by the p_{T} distributions shown in the previous section for this variable.

$\Delta\phi(K^*, \gamma)$ reweighting This is another alternative model similar to the previous systematic, however in this variation the $\Delta\phi(K^*, \gamma)$ distribution is reweighted around $\pi/2$ using a function of the form $1 + a\Delta\phi$, where a is chosen such that the variation effectively captures the associated fluctuations in the shape. The value of a selected is 10 based on the $\Delta\phi$ plots shown in the previous section.

Tilt variation The previous systematics provide a lateral shift of the peak of the $m_{K^+\pi^-\gamma}$ distribution to some degree, either across the whole range or in the tails. However, the shape could also be distorted through a general "tilt" of the peak. This is accounted for by accounting for a discrepancy in the ratio of the model and data

through reweighting, resulting in either an "upwards" or "downwards" tilting of the peak. A cubic fit is performed to the ratio of the data and the prediction from the model in the VR2a region, in order to also account for the low-mass points. The parameters from this fit is used to re-weight the model to match the data. The reflection of this line about $y = 1$ is also taken as a variation in the opposite direction. The fit function is given in Equation 5.1.

$$y = -1.8 \times 10^{-7}x^3 + 1.1 \times 10^{-3}x^2 - 0.0219x + 2.44 \tag{5.1}$$

The resulting distorted alternative background models are shown in Figure 5.10. From these alternative models, KDE templates are derived in the same way as the nominal background template. These resulting KDE templates are then included in the final fit as either Gaussian-constrained NPs or unconstrained NPs, acting as uncertainties for the background model for the fit to morph between. The interpolation between the shapes is done using the RooMomentMorph class, details of which are supplied in Ref. [96]. Further validation plots are given in Appendix A.

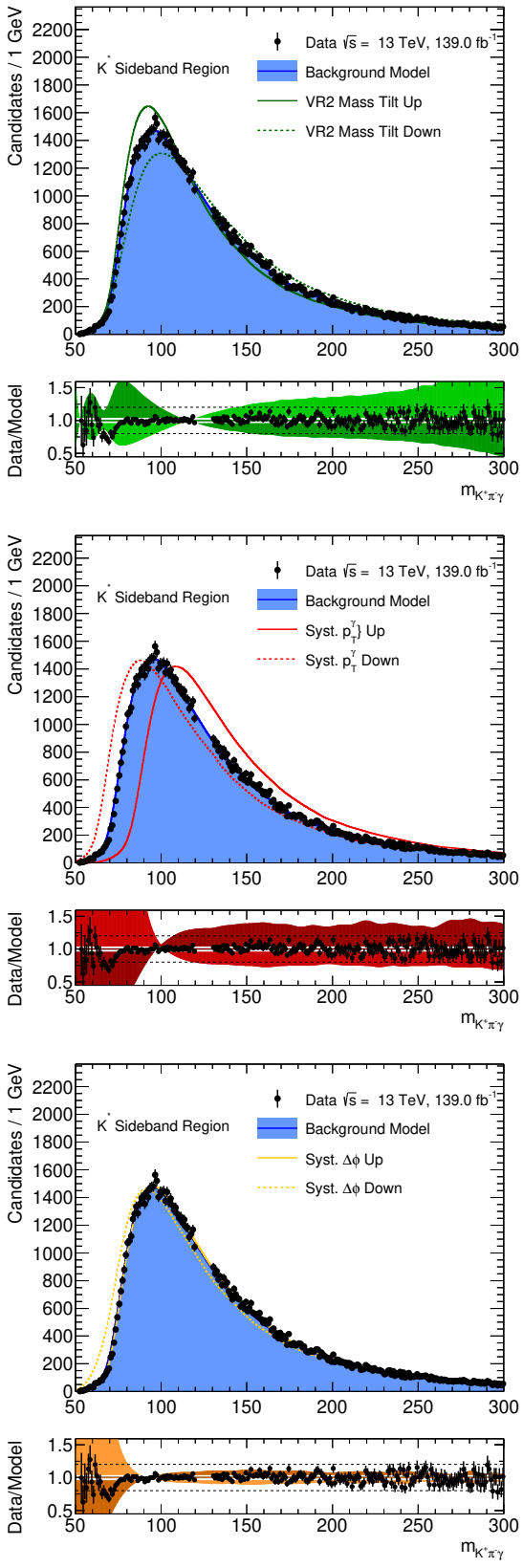

Figure 5.10: $m_{K^+\pi^-\gamma}$ distributions in data side-bands, compared to the background model prediction. The uncertainty bands represent the maximum difference of the variations from the nominal, for each individual systematic variation.

5.5 Systematic Uncertainties

MC simulation is used to model signal events, and in doing so many assumptions must be made in order to obtain signal yields and shapes. In order to account for this, systematic uncertainties must be assigned, which are input as nuisance parameters into the final fits. The theoretical systematic uncertainties have been described in Section 3.4.3.

5.5.1 Experimental systematic uncertainties

Various systematic uncertainties arising from experimental sources affect the obtained results. These are evaluated by comparing the normalisation of the nominal $m_{K^+\pi^-\gamma}$ distribution when compared to the $m_{K^+\pi^-\gamma}$ distribution with a particular systematic variation applied, to give the relative uncertainty.

The experimental systematic uncertainties can be broadly categorised and grouped together in order to obtain a few uncertainties which are included as nuisance parameters in the final fitting procedure.

The first of these is the uncertainty on the reconstruction, identification or isolation of the photon in the $H \to K^*\gamma$ decay, which is taken as one nuisance parameter due to the relatively small magnitude of the contributing systematics. The value of this uncertainty, when taking into account the various sources of uncertainty, amounts to 1.52%.

Following this, the photon energy scale and resolution also have uncertainties. There are 30 energy scale variations and 4 resolution variations, which are all independent to one another. These sources are applied correlated between each other. This results in an uncertainty of 0.11%.

For the tracks, the effects of the efficiency and resolution uncertainties are obtained by using a series of tools which smear, exclude, or modify tracks based on the

variations in efficiency in the different regions of the detector. This is a stochastic process, and as such the variations were applied 5 times and the mean value taken to be the final uncertainty. The non-negligible track uncertainties result in an overall value of 3%.

There are also experimental uncertainties arising from the collection of the data - either the uncertainty of the luminosity of the combined 2015-2018 dataset, which amounts to 1.7%, or the uncertainty arising from the trigger. The triggers used to collect events for these analyses have separate photon and track components, which are taken to be independent. The trigger efficiency, defined as the yield of events satisfying both the offline selection and the trigger divided by the yield of events satisfying the offline selection alone is a source of uncertainty for both the photon and track components. For the photon component, the uncertainty on the trigger efficiency is 0.2%. For the track component, this uncertainty is expected to be small compared to the existing track systematic defined previously.

5.6 Statistical analysis and expected sensitivity

The likelihood model, statistical interpretation, fitting procedure, and expected/obtained limits from the full unblinded dataset are presented in the following.

5.6.1 Likelihood model

An unbinned maximum likelihood fit to the final signal region data events is used in order to obtain the upper limit on the branching ratio of the $\mathcal{B}(H \to K^*\gamma)$ channel. The components of the fit are the PDF of the signal channel, the background PDF derived from the KDE procedure, the background model normalisation, and the systematic uncertainties. The experimental systematic uncertainties are included as nuisance parameters. The background shape systematic uncertainties, based on the three separate variations described in Section 6.3, are included as nuisance parame-

ters which are profiled during the fit. The $\Delta\phi$ and p_T shift systematic shapes have an additional Gaussian constraint applied. The signal m_H distribution is modelled with a double Gaussian as described in Section 6.1, with the only discriminating variable used being $m_{K^+\pi^-\gamma}$.

5.6.2 Statistical Interpretation

In order to perform the maximum likelihood fit, a likelihood must first be constructed with depends on the parameter of interest, which in this instance is μ (the branching ratio). The likelihood is built from the signal and background models, and takes the form

$$\mathcal{L}(\mu,\theta) = \text{Pois}(N|\mu\cdot S(\theta)+B(\theta))\cdot\prod_{k=1}^{N}\mathcal{P}(m_k;\mu,\theta)\cdot C(\theta), \tag{5.2}$$

which can be broken down as the product of the Poisson probability of observing N events given the expected values for the signal S and background B with the product over the N events of the shape PDF $\mathcal{P}$. The combined PDF takes into account both the signal and background, where m_k is the mass of the Higgs candidate in the event. $C(\theta)$ are the constraint terms. The nuisance parameters are collectively denoted with θ.

In order to obtain the limits, the CL_s modified frequentist formalism [97] with the profile-likelihood ratio test statistics [98], as well as the asymptotic approximations which are derived in Ref. [99] are used. To calculate the confidence intervals (CL), the profile likelihood ratio $\Lambda(\mu)$ is constructed as follows:

$$\Lambda(\mu) = \frac{\mathcal{L}\big(\mu,\hat{\hat{\theta}}(\mu)\big)}{\mathcal{L}(\hat{\mu},\hat{\theta})} \tag{5.3}$$

taking into account the parameter of interest μ and the nuisance parameters θ. The

final unbinned maximum likelihood fit can then be performed.

The value of θ maximising $\mathcal{L}$ for a given value of μ is denoted as $\hat{\hat{\theta}}$. The value of μ that maximises $\mathcal{L}$ for both θ and μ is denoted as $\hat{\mu}$.

The value of $\mu = 1$ corresponds to a branching ratio of 1.0×10^{-6}.

5.6.3 Expected Sensitivity

Expected sensitivies for the analysis can be calculated, which act as indicators of the performance of the analysis overall, as well as confirmation of the robustness of the fitting procedure. The expected sensitivities are calculated as 95% CL upper limits from the SR dataset. A dataset representing the expected background distributions is calculated, known as the Asimov dataset, which is derived from a conditional fit to the SR data with $\mu = 1$. The fit contains the normalisation of the inclusive background, which is obtained from the fits to the background templates. Validation of the fit to the Asimov dataset is performed using signal injections, detailed in Appendix E.

The obtained fit is shown in Fig 5.11.

	Expected	$\pm1\sigma$	$\pm2\sigma$
Higgs [10^{-4}]			
No systematics	1.19	1.66/0.86	2.24/0.64
Shape+Norm	1.21	1.69/0.87	2.31/0.65

Table 5.4: Expected branching ratio limits at the 95% CL for $H \to K^*\gamma$. The limits obtained including and excluding the systematics are compared.

5.6.4 Results

As a test of the robustness of the fitting and background modelling procedure, a fit is performed using data in a sideband of the meson mass, including the background shape and signal normalisation systematics as nuisance parameters. The fit is shown

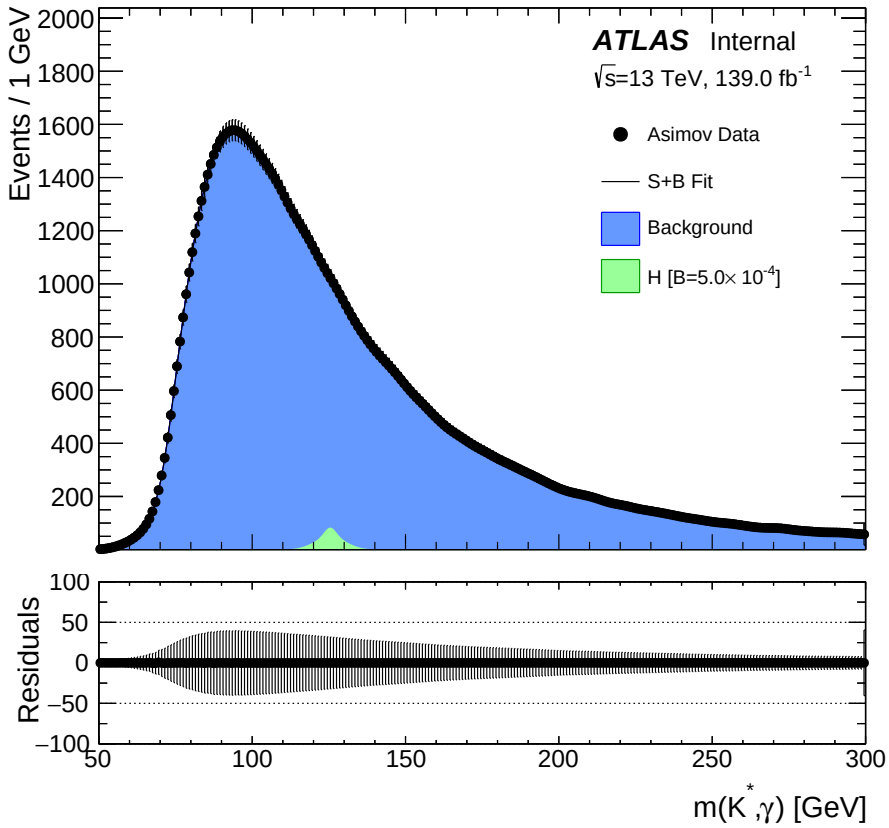

Figure 5.11: $m_{K^+\pi^-\gamma}$ fit using Asimov data.

in Fig 5.12. Since the resulting background shape is not expected to be drastically different from the final signal region data, this test is valuable in demonstrating the validity of the fitting procedure. The resulting fit parameters for both the background-only and the signal-plus-background fits to sideband meson mass data are given in Table 5.5. The θ parameters correspond to the nuisance parameters for both the signal normalisation uncertainties as well as the background shape uncertainties. The μ parameters are the background and signal normalisations. A full list is as follows:

- θ_HZ_Lumi: The uncertainty due to the luminosity on the full dataset.
- θ_H_PDF_Scale: The uncertainty due to the PDF scale on the signal samples.
- θ_H_Ph_Eff: The combined uncertainty of the photon signal systematics.
- θ_H_QCD_Scale: The uncertainty due to the QCD scale on the signal samples.

- θ_H_Trk_Eff: The combined uncertainty of the track signal systematics.
- θ_backgroundShape_DPHI_INC: The nuisance parameter corresponding to the $\Delta\phi$ shape systematic KDE.
- θ_backgroundShape_PHOTONPT_INC: The nuisance parameter corresponding to the $p_{\mathrm{T}}^{\gamma}-$shift shape systematic KDE.
- θ_backgroundShape_TILT_INC: The nuisance parameter corresponding to the global tilt shape systematic KDE.
- μ_Mix_KDE_INC: The nominal background shape KDE nuisance parameter.
- μ_H: The signal normalisation nuisance parameter.

No unexpected deviations in the fit parameters are observed, and the background shape systematic and signal normalisation systematic nuisance parameters are mildly pulled as expected. Given that this sideband dataset provides a representation of the signal region data for the fitting procedure to perform on, this result provides sufficient confidence in the fitting procedure that the signal region dataset can be unblinded.

After freezing the analysis strategy, the full dataset can be unblinded, and background-only and signal-plus-background fits can be performed. The purpose of performing a background-only fit is to demonstrate that the fit functions as expected. No unexpected deviations are observed in the systematic uncertainties. The resulting fit parameters are shown in Table 5.6, and the signal-plus-background fit is shown in Fig 5.12. The results indicate that the fitting procedure captures the background well, given the small pulls observed. The negative signal strength parameter μ_H does not indicate a negative signal - given the statistics procedure followed, it simply indicates that fewer background model events were observed under the region around the signal mass than expected. The issue of overly-optimistic limits given this negative value is also avoided, given the asymptotic limit procedure used to obtain the final limits. Finally, the small pulls on the signal systematics indicate

Parameter	Background		Signal+Background	
	Value	Uncertainty	Value	Uncertainty
θ_HZ_Lumi	0	1	-5 $\times 10^{-4}$	1
θ_H_PDF_Scale	0	1	-7 $\times 10^{-4}$	1
θ_H_Ph_Eff	0	1	-5 $\times 10^{-4}$	1
θ_H_QCD_Scale	0	1	-1 $\times 10^{-3}$	1
θ_H_Trk_Eff	0	1	-8 $\times 10^{-4}$	1
θ_backgroundShape_DPHI_INC	0.46	0.1	0.46	0.1
θ_backgroundShape_PHOTONPT_INC	0.08	0.02	0.08	0.02
θ_backgroundShape_TILT_INC	0.20	0.06	0.02	0.06
μ_Mix_KDE_INC	1.00	0.003	1.01	0.003
μ_H	-	-	-20.1	89.5

Table 5.5: Fit parameters for background-only and signal-plus-background fits to sideband meson mass data.

Parameter	Background		Signal+Background	
	Value	Uncertainty	Value	Uncertainty
θ_HZ_Lumi	0	1	-9 $\times 10^{-6}$	1
θ_H_PDF_Scale	0	1	-2 $\times 10^{-5}$	1
θ_H_Ph_Eff	0	1	-8 $\times 10^{-6}$	1
θ_H_QCD_Scale	0	1	-8 $\times 10^{-5}$	1
θ_H_Trk_Eff	0	1	-6 $\times 10^{-7}$	1
θ_backgroundShape_DPHI_INC	0.01	0.1	0.01	0.1
θ_backgroundShape_PHOTONPT_INC	0.09	0.02	0.09	0.02
θ_backgroundShape_TILT_INC	0.02	0.06	0.02	0.06
μ_Mix_KDE_INC	1.0	0.003	1.0	0.003
μ_H	-	-	-63.1	61.8

Table 5.6: Fit parameters for background-only and signal-plus-background fits to data.

that the fit does not have the ability to constrain them, which is expected given that this search is statistics-dominated, and that the background shape systematic uncertainties are dominant.

Following this, the 95% CL upper limit can be obtained using the unblinded SR data, and the observed 95% CL upper limit on the branching ratio is 8.9×10^{-5}.

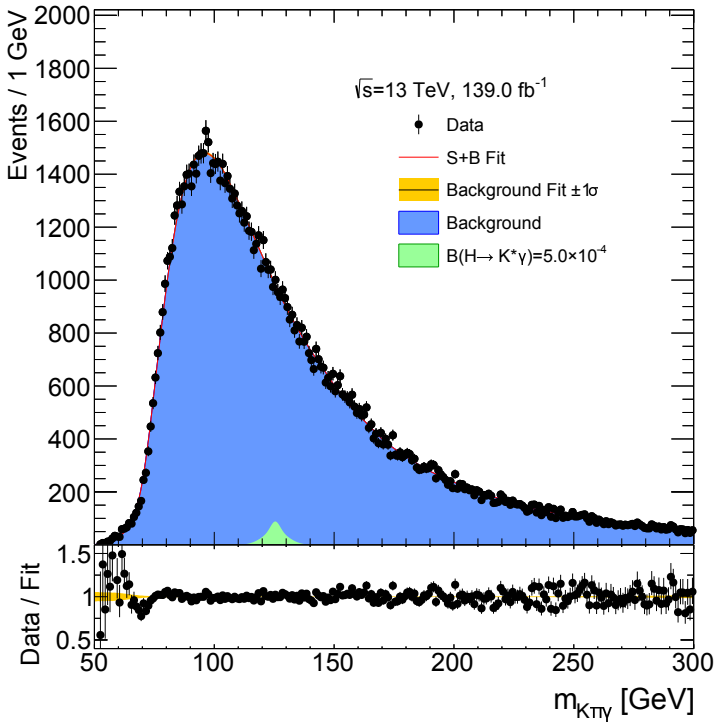

((a))

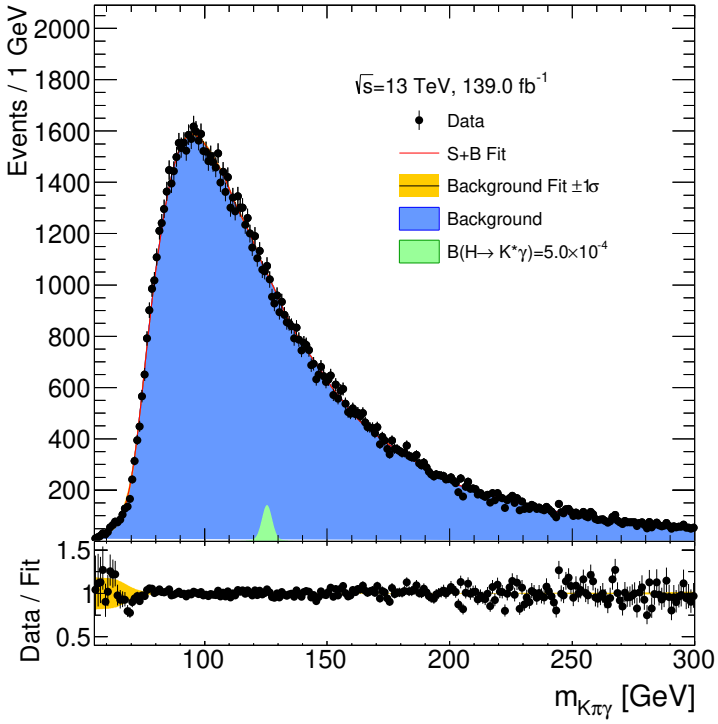

((b))

Figure 5.12: $m_{K^+\pi^-\gamma}$ fit using (a) meson mass sideband data and (b) unblinded signal region data.

CHAPTER 6

Searches for the decays $H/Z \to \omega\gamma$

The Higgs boson decay $H \to \omega\,\gamma$ offers an opportunity to access the up/down-quark Yukawa couplings [56]. Several calculations of the branching ratio for decays of $H \to \omega\,\gamma$ within the Standard Model (SM) have been developed, the most recent include $\mathcal{B}\,(H \to \omega\,\gamma) = (1.48 \pm 0.07) \times 10^{-6}$ [3] and $\mathcal{B}\,(H \to \omega\,\gamma) = (1.6 \pm 0.2) \times 10^{-6}$ [56]. New beyond the SM physics may affect the up/down quark couplings to the Higgs boson and result in modification of these branching fractions. The up/down-quark Yukawa couplings are currently unconstrained by existing measurements.

At the same time, the analogous exclusive decays of the abundantly produced Z bosons, are attracting interest [49, 2, 50], as they offer a novel and rich physics programme in precision quantum chromodynamics (QCD), electroweak physics, and physics beyond the SM. In precision QCD, these decays are a laboratory to study the QCD factorisation approach [2]. As a result, they provide a model-independent probe to the light-cone distribution amplitudes of hadrons. In electroweak physics, they provide direct sensitivity to the couplings of the Z boson to light quarks,

for which a limit was set at LEP in the ALEPH experiment [1] to a value of $\mathcal{B}(Z \to \omega\,\gamma) < 6.5 \times 10^{-4}$. The SM prediction of the branching fraction has been calculated to be $\mathcal{B}(Z \to \omega\,\gamma) = (2.82 \pm 0.40) \times 10^{-8}$, $m_\omega = 782.65 \pm 0.12$ MeV [2].

We perform a search for the decays of the Higgs and Z bosons to $\omega\,\gamma$ using the ATLAS 2016, 2017 and 2018 pp dataset collected at a centre-of-mass energy of $\sqrt{s} = 13$ TeV. The analysis is performed by reconstructing exclusively the decays $\omega \to \pi^+\pi^-\pi^0$. The branching fraction for $\omega \to \pi^+\pi^-\pi^0$ decays is $\mathcal{B}(\omega \to \pi^+\pi^-\pi^0) = (89.2 \pm 0.7)\%$ [1], whilst the rest of the ω width is largely into $\pi^0\gamma$ and $\pi^+\pi^-$. The analysis will exploit the distinctive $H \to \omega\gamma \to \pi^+\pi^-\pi^0\gamma$ topology of a pair of oppositely-charged, high p_{T} isolated tracks, with a very small opening angle ($\Delta R < 0.05$), recoiling against a hard isolated photon. A novel addition to the decay topology in this channel is the neutral pion, which requires a different selection approach taking advantage of the τ particle flow reconstruction algorithms. The $\omega \to \pi^+\pi^-$ decay mode was not considered in this search, due to the small magnitude of the branching ratio. Although it would provide a better resolution for the reconstruction of the Higgs or Z boson, the difference in kinematics is sufficient enough that the analysis strategy for this channel would be different to the $\omega \to \pi^+\pi^-\pi^0$ decay mode under consideration.

Until the analysis selection was frozen, the analysis was blinded, removing events satisfying 80 GeV $< m_H <$ 100 GeV and 115 GeV $< m_H <$ 135 GeV.

6.1 Event Selection

For the event selection optimisation, the same procedure was followed as in Section 5.2. Both p_T and p_T^γ were found to be optimised at the initial cut values given, and the meson isolation was found to be optimal at a value of 0.1.

The following dedicated triggers were activated during the 13 TeV data collection for this analysis:

- `HLT_g35_medium_L1EM24VHI_tau25_dipion3_tracktwo_60mVis10000`

These triggers are a combination of a photon and tau trigger including an invariant mass requirement where the standard tau variables have been modified to select two tracks consistent with a $\omega \to \pi^+\pi^-\pi^0$ decay, instead of the nominal 1- or 3-prong tau objects.

The following selection is in part motivated by the kinematic distributions given in Section 2.6. In this analysis, the same track selection criteria are applied as discussed in Chapter 5, namely "Loose" quality, opposite charge, $|\eta^\pi| < 2.5$, $p_{\mathrm{T}}^\pi > 15$ GeV, and one must have at least $p_{\mathrm{T}}^\pi > 20$ GeV, motivated in part by the kinematic studies detailed in Section 2.6. The invariant mass of the di-track system must satisfy $m_{\pi^+\pi^-} > 2 \times m_\pi$ and $m_{\pi^+\pi^-} < m_\omega$. The ω invariant mass must satisfy $650 < m_\omega < 850$ MeV. The sum of the p_{T} of the reconstructed ID tracks within $\Delta R < 0.2$ of the leading track candidate for tracks with $p_{\mathrm{T}} > 0.5$ GeV and $|\Delta z^0_{\mathrm{PV}}| < 1.5$mm must be less than 6% of the ω candidate p_{T}.

Finally, the best pair of tracks is selected based on proximity to the average of a toy MC distribution of the di-track mass, amounting to a value of 450 MeV. Input files produced using Powheg interfaced to Pythia8 containing samples of Higgs bosons produced via different processes (gluon-gluon fusion, Higgs-strahlung (W/Z), vector boson fusion, and top-quark associated production) are used to simulate these decays.

The same requirements are applied to photons as discussed in Chapter 5, namely: "tight" photon identification [6] $|\eta_\gamma| < 2.37$ and outside of $1.37 < |\eta_\gamma| < 1.52$, $p_T^\gamma > 35$ GeV,and "`FixedCutTight`" isolation [95].

Neutral pion candidates are expected to leave a signature of a pair of overlapping photon calorimeter clusters, typically very close in ΔR to the system. As such, algorithms designed to search for neutral pions in these topologies would be the preferred method of reconstruction. The TauPFO algorithms, optimised to search for neutral pions in τ-like decay signatures, are used to reconstruct the neutral pion

in the ω decay. The algorithm is summarised as follows. π^0 candidates constructed by clustering cells in the EM calorimeter in the core region of a tau jet candidate. Following this, π^0 energy is corrected for contamination from hadronic tracks by estimating the energy deposited by hadronic tracks in the EM calorimeter, and then subtracting this from the π^0 if the track is within $\Delta R = 0.04$. To ensure π^0 candidates are from π^0's and not hadronic remnants/pileup/other, a minimum p_{T} requirement is applied (ranging from 2.1-2.7 GeV) and then a BDT ID is finally applied to reject background. More details are provided in Ref. [100].

Tau-jets are searched for with no identification requirements within $\Delta R = 0.1$ to the system. The presence of Pi0PFOs (neutral pion particle flow objects) is then checked within the tau-jet object. The closest Pi0PFO to the ditrack system is taken to be the π^0 candidate.

$\omega \to \pi^+\pi^-\pi^0$ candidates and photons, that satisfy the criteria discussed above, are paired to form loose $\omega\gamma \to \pi^+\pi^-\pi^0\gamma$ candidates. These loose candidates are retained for further analysis if they satisfy that the difference in azimuthal angle between the $\omega \to \pi^+\pi^-\pi^0$ candidate and photon must satisfy $\Delta\phi(\omega\,\gamma) > \pi/2$

Finally, for validation and cross-checking purposes, a sideband region is defined. This dataset applies the same selection criteria listed above, but with the exception of an invariant mass requirement of $m_\omega < 650$ MeV and $850 < m_\omega < 2000$ MeV, essentially taking all events outside of the SR mass window. This provides sufficient statistics in the dataset, as well as a representative sample of the background.

As in Chapter 5, several regions are defined for this analysis, based on the selection discussed above, and these are summarised in Table 6.1. It is noted that the signal Region SR comprises all of the above requirements. Generator level distributions for the reconstructed objects required by the trigger are given in Appendix B.

The PDF in $m_{\pi\pi\pi\gamma}$ for signal events is determined using simulation. For the Higgs boson the sum of a Gaussian and a Crystal Ball function is used. The Crystal Ball function allows the low rising tail to be fitted, which is a feature of the imperfect

Region	Cut		
GR	-	-	-
VR1	ω Isolation < 0.1	-	-
VR2a	-	Photon Fixed Cut Tight (Calo)	-
VR2b	-	-	Photon Fixed Cut Tight (Track)
SR	ω Isolation < 0.1	Photon Fixed Cut Tight (Calo)	Photon Fixed Cut Tight (Track)

Table 6.1: Definition of the various regions used. The selection is defined with respect to the basic GR selection.

π^0 reconstruction. All Higgs production modes listed in the MC samples are used as events for the signal modelling, weighted by cross section. The cut flow for MC and data is given in Tables 6.3 and 6.4.

A Voigtian function is used for the Z boson signal PDF. The width of the function is taken to be the world's average for the Z boson width. This is convoluted with an efficiency function, which is essentially the efficiency of a Z boson signal passing the reco-level SR versus the true mass of the Z boson, and accounts for the dependancy of the acceptance on the mass of the ditrack system. Since the kinematic selection used gives a turn-on in the selection efficiency with the real Z mass, this function is included to account for this, and uses truth MC to avoid resolution effects. This is shown in Fig. 6.2.

Given the nature of the reconstruction of the neutral pion, it is worth checking that the energy scale reconstruction is being performed to an acceptable level. As such, simple Gaussian distribution fits are performed to the meson mass, for both signal MC samples and the data. This is shown in Fig. 6.3, and the corresponding fit parameters in Table 6.2. The results indicate that the neutral pion is being reconstructed to a sufficient standard.

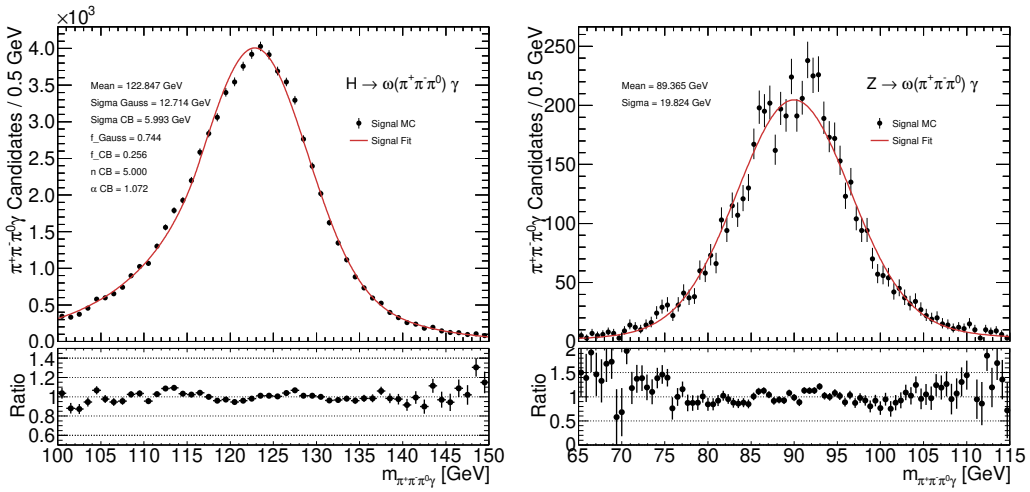

Figure 6.1: The $m_{\pi\pi\pi\gamma}$ signal model distributions for the $H \to \omega\gamma$ channel (left) and $Z \to \omega\gamma$ channel (right). The Higgs boson signal model is the sum of a Gaussian and a Crystal Ball function, where `Sigma Gauss` and `Sigma CB` are the standard deviations of the two functions and `f_gauss` is the fraction of the former. The parameter `n_CB`, corresponding to the n in the Crystal Ball function, is fixed to 5.0, and the α of the function is left free. For the Z boson signal a Voigtian, multiplied by an efficiency function to account for the effect of the event selection as a function of the mass, is used.

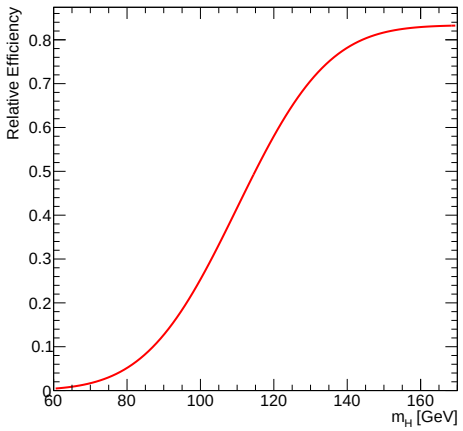

Figure 6.2: The mass dependent efficiency function derived from the truth acceptance.

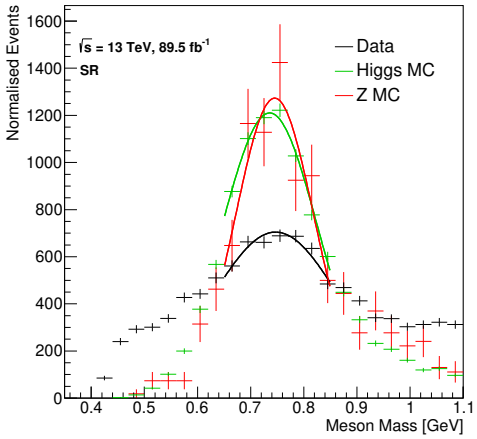

Figure 6.3: Gaussian distributions fits to the ω mass in Higgs MC, Z Boson MC and Data for the GR and SR.

	GR		SR	
	Mean [GeV]	Sigma [GeV]	Mean [GeV]	Sigma [GeV]
Data	0.754±0.002	0.132±0.005	0.747±0.004	0.121±0.009
Higgs MC	0.735±0.001	0.091±0.002	0.735±0.002	0.089±0.003
Z Boson MC	0.729±0.006	0.073±0.006	0.745±0.006	0.074±0.007

Table 6.2: Gaussian fit results to data, Higgs MC and Z Boson MC in the GR and SR.

Table 6.3: Cut Flow in signal MC and data, assuming SM values for branching ratios and production cross-sections. Event yields for all cut stages are below 0.005 for the ttH dilepton sample.

	Signal									**Data**
	ggF	VBF	W^-H	W^+H	ZH	ttH allhad	ttH semilep	ttH dilep	Z	
Starting events	4.12	0.34	0.05	0.07	0.08	0.02	0.02	0.00	5.25	1.58×10^6
Passed Trigger	4.11	0.34	0.05	0.07	0.08	0.02	0.02	0.00	5.23	1.58×10^6
γ:- tight, p_T/η req.	2.63	0.22	0.03	0.04	0.05	0.02	0.01	0.00	2.13	1.58×10^6
Trk:- loose, p_T/η req.	2.25	0.20	0.03	0.04	0.04	0.01	0.01	0.00	1.69	1.58×10^6
Photon tight quality	0.95	0.09	0.01	0.01	0.02	0.00	0.00	0.00	0.40	359 764
Lead Track p_T	0.95	0.09	0.01	0.01	0.02	0.00	0.00	0.00	0.40	359 764
ω mass window	0.33	0.03	0.00	0.01	0.01	0.00	0.00	0.00	0.13	30 147
$\Delta\phi(\omega\gamma) > \pi/2$	0.30	0.02	0.00	0.00	0.00	0.00	0.00	0.00	0.13	22 768
Pass GR	0.30	0.02	0.00	0.00	0.00	0.00	0.00	0.00	0.12	22 437
Pass SR	0.19	0.01	0.00	0.00	0.00	0.00	0.00	0.00	0.07	4231

Table 6.4: Cut Flow in signal MC and data, assuming SM values for branching ratios and production cross-sections. The percentage value is relative to the starting total number.

	Signal (%)									**Data** (%)
	ggF	VBF	W^-H	W^+H	ZH	ttH allhad	ttH semilep	ttH dilep	Z	
Starting events	100	100	100	100	100	100	100	100	100	100
Passed Trigger	99.75	99.87	99.94	99.91	99.92	100	100	100	99.72	100
γ:- tight, p_T/η req.	63.84	65.51	63.53	59.39	61.77	71.86	71.82	72.81	40.60	100
Trk:- loose, p_T/η req.	54.56	58.55	58.53	54.43	55.76	71.17	71.26	72.36	32.18	100
Photon tight quality	23.03	25.55	25.99	20.49	21.25	7.59	8.36	9.61	7.69	22.73
Lead Track p_T	23.03	25.55	25.99	20.49	21.25	7.59	8.36	9.61	7.69	22.73
ω mass window	8.08	8.92	8.98	7.32	7.15	1.98	2.27	3.02	2.55	1.90
$\Delta\phi(\rho\gamma) > \pi/2$	7.20	6.01	0.00	5.10	4.92	0.99	1.09	1.55	2.40	1.44
Pass GR	7.18	5.98	6.22	5.00	4.88	0.97	1.05	1.46	2.38	1.42
Pass SR	4.55	3.73	3.68	2.90	2.99	0.44	0.50	0.75	1.35	0.27

6.2 Background Modelling

6.2.1 Background Modelling Methods

The background modelling procedure used for the $H/Z \to \omega\gamma$ analysis is analogous to the one described in Section 5.3.

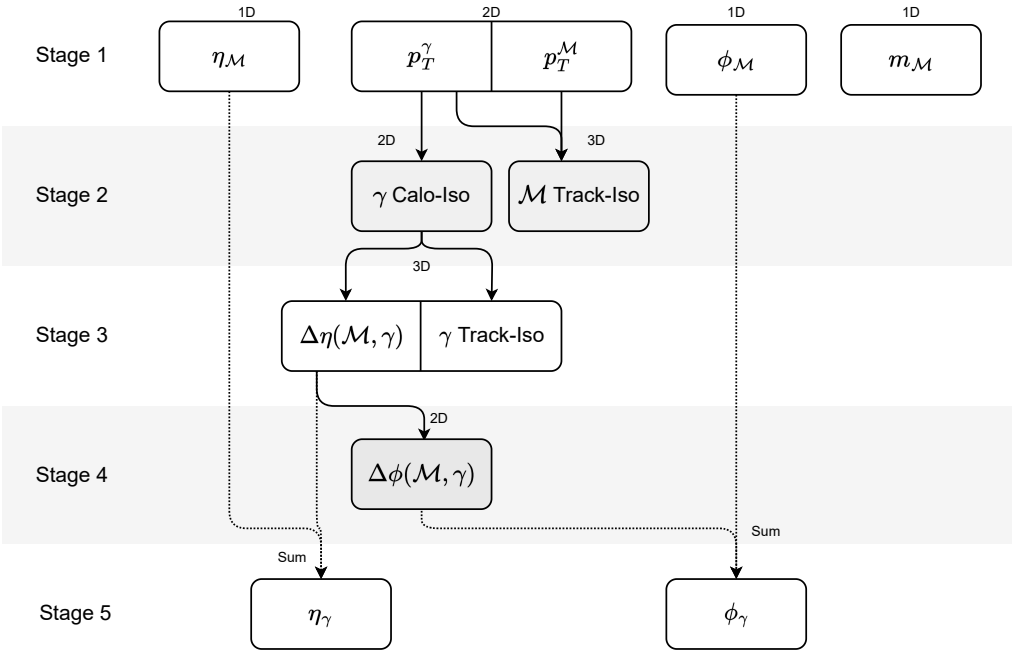

Figure 6.4: Background model procedure.

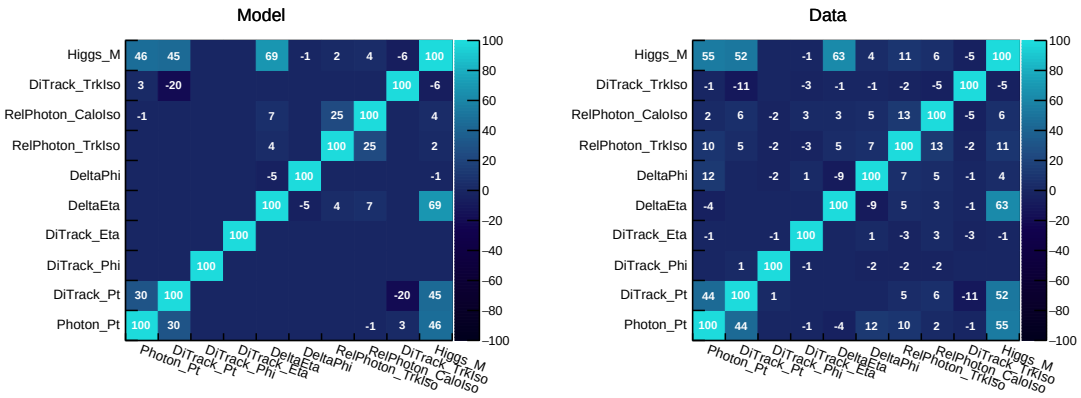

Figure 6.5: Correlation matrices showing the linear correlations between modelled variables in the background modelling, for the model (left) and the data (right), in the SR region.

The choice of the order of the sampling within the background model is based on the correlation matrices shown in Figure 6.5. For each step of the model, the decision was chosen to create histograms based on the strength of the correlation - however, it is sometimes the case that a correlation is not modelled even if a strong correlation exists between two variables, if one of those variables has multiple correlations with other variables. The binning of the histograms and the order of the sampling results in the final modelling of the SR $m_{\omega\gamma}$ distribution, which is the variable of interest in the fitting procedure.

The background model configuration is shown in Fig 6.4. The motivation for each stage is determined by the correlations shown in Fig 6.5. The procedure is as follows:

i) Initially, values for $p_{\mathrm{T}}^{\mathcal{M}}$ and p_{T}^{γ} are sampled from a 2D histogram of ($p_{\mathrm{T}}^{\mathcal{M}}$, p_{T}^{γ}) from the sample of data, since they have the largest correlation in data (44%). The values of the meson mass, $\eta_{\mathcal{M}}$ and the ϕ angle of the meson are sampled from 1D histograms of the variables from the data sample. 1D histograms are used since these variables are not considered in the correlation matrices.

ii) The $\mathcal{M}$ isolation distribution is then sampled from a 3D histogram in which the $\mathcal{M}$ isolation is distributed in bins of $p_{\mathrm{T}}^{\mathcal{M}}$ and p_{T}^{γ}, where the value chosen is based on the values of $p_{\mathrm{T}}^{\mathcal{M}}$ and p_{T}^{γ} sampled in the previous step. This is motivated by the correlation between the $\mathcal{M}$ isolation and p_{T}^{γ}, and also the physical motivation that the $\mathcal{M}$ isolation should in some way be correlated to $p_{\mathrm{T}}^{\mathcal{M}}$. Then, the relative photon calorimeter isolation variable is sampled from a 2D histogram, distributed in bins of p_{T}^{γ}.

iii) From this value of the relative photon calorimeter isolation, the values of $\Delta\eta(\mathcal{M},\gamma)$ and relative photon track isolation are sampled simultaneously from a 3D histogram, since all three variables show a correlation in the data with each other - particularly the two isolation variables.

iv) The value of $\Delta\phi(\mathcal{M},\gamma)$ is sampled from a 2D histogram, distributed in bins of $\Delta\eta(\mathcal{M},\gamma)$.

v) Given these sampled values, and the values sampled previously for $\Delta\eta(\mathcal{M}, \gamma)$ and $\Delta\phi(\mathcal{M}, \gamma)$, the values of $\eta_{\mathcal{M}}$ and ϕ_{γ} are then defined by summing.

Plots showing the distributions of relevant kinematic variables for the GR, VRs and SR are given in Figs 6.6 - 6.9. The plots demonstrate a good agreement between the data and the background model, in particular for the distribution of m_H which is the only variable used in the final fitting procedure.

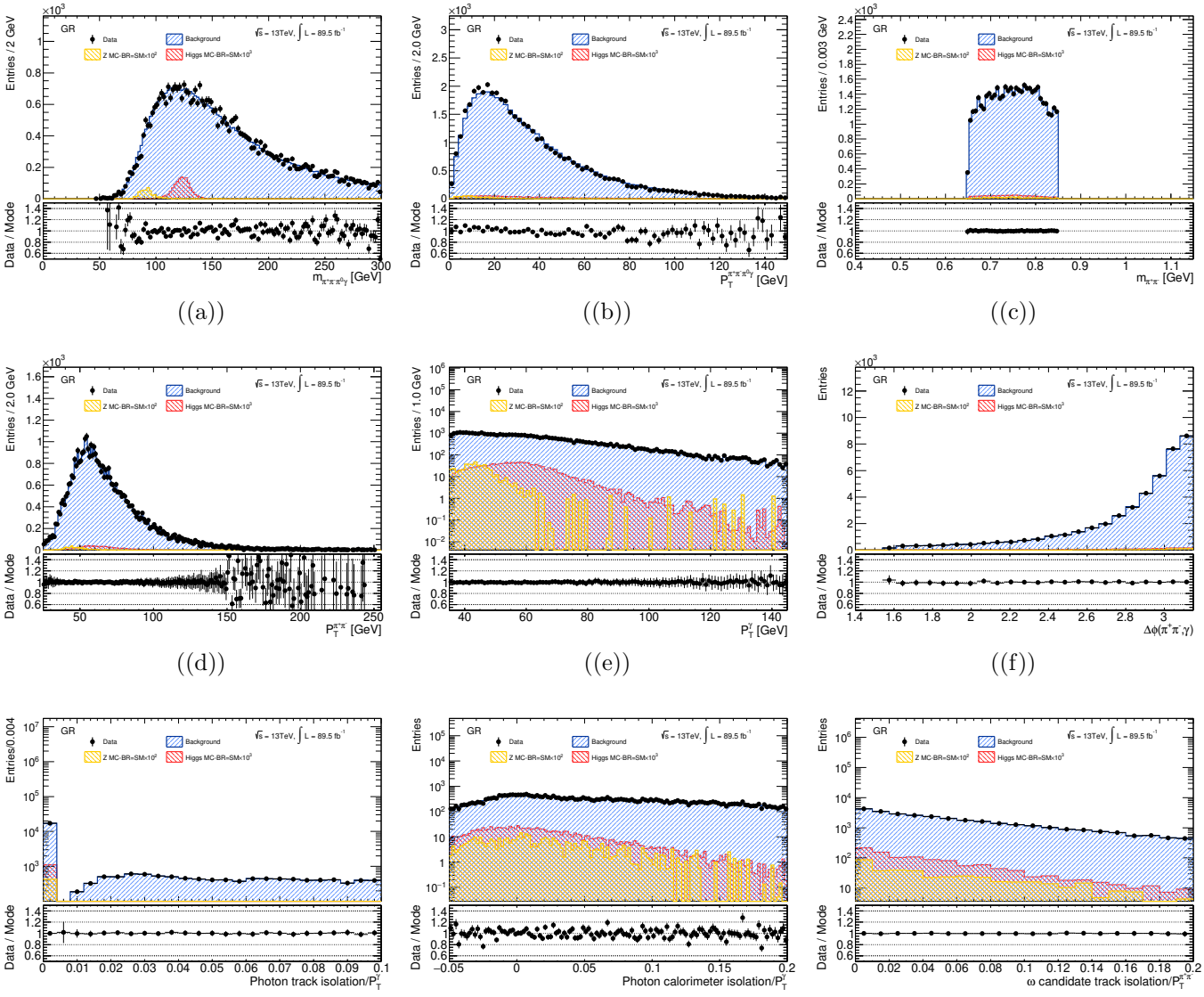

Figure 6.6: GR distributions of the background model.

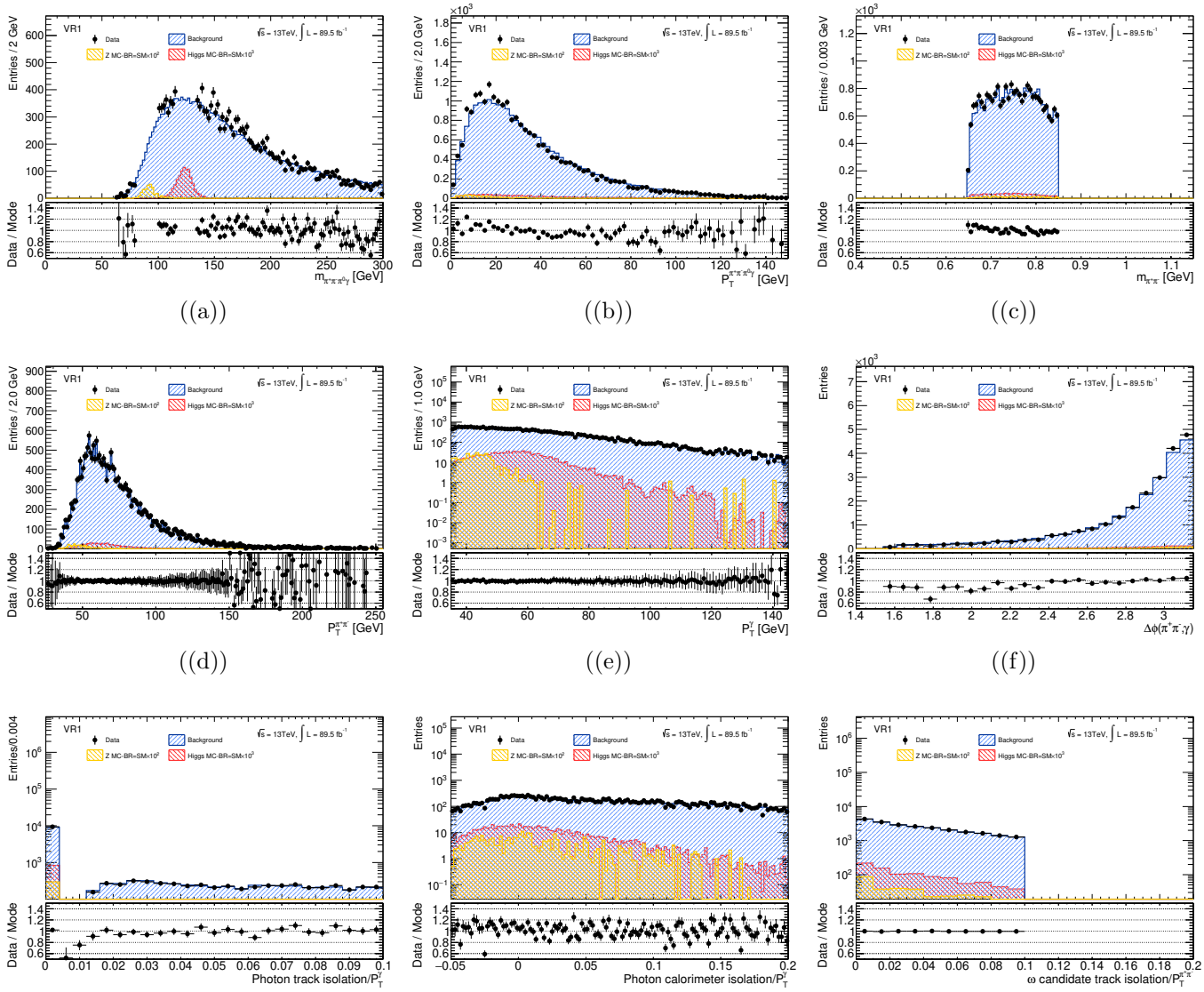

Figure 6.7: VR1 distributions of the background model, applying the meson track isolation requirement.

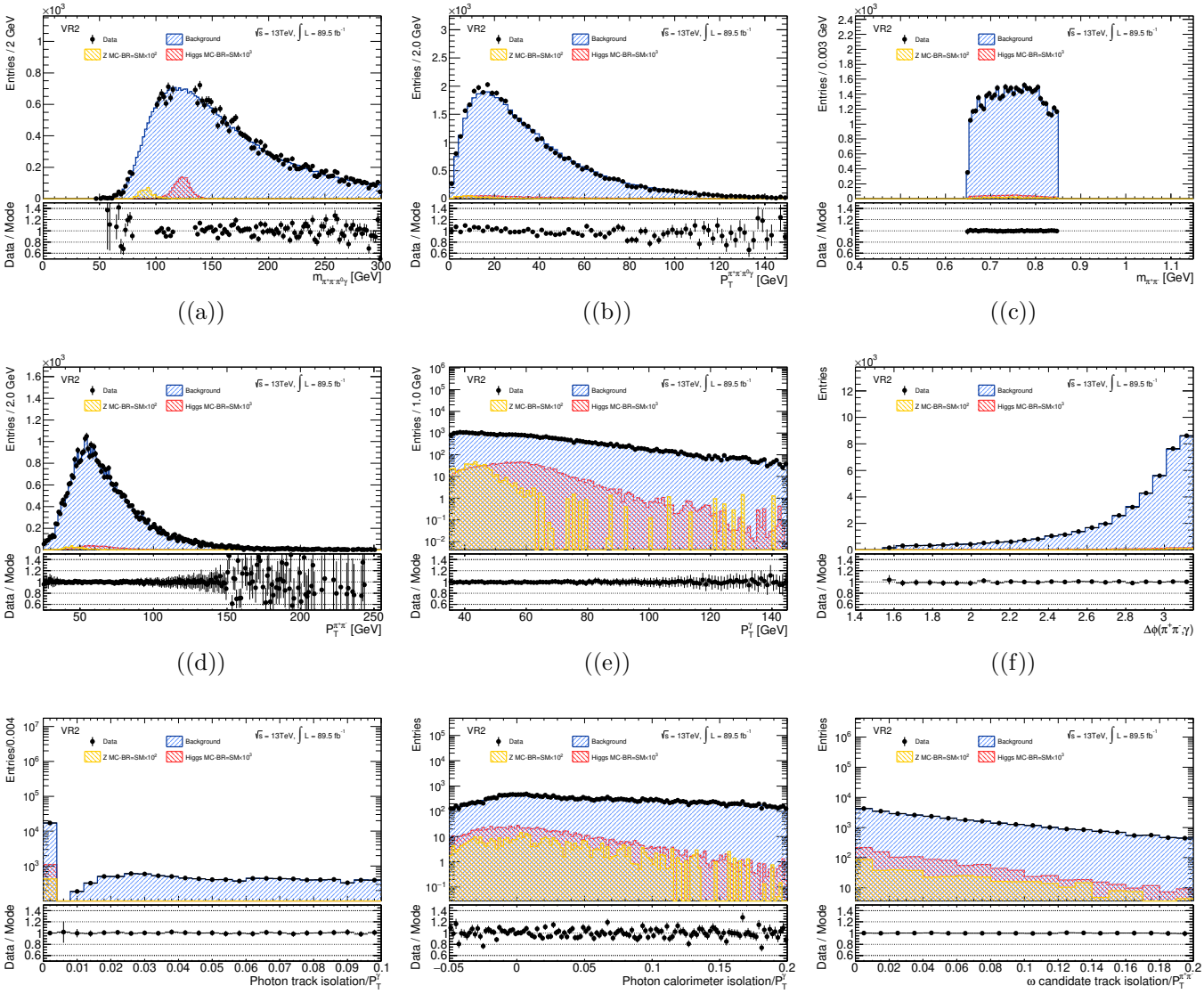

Figure 6.8: VR2 distributions of the background model, applying the photon calorimeter isolation requirement.

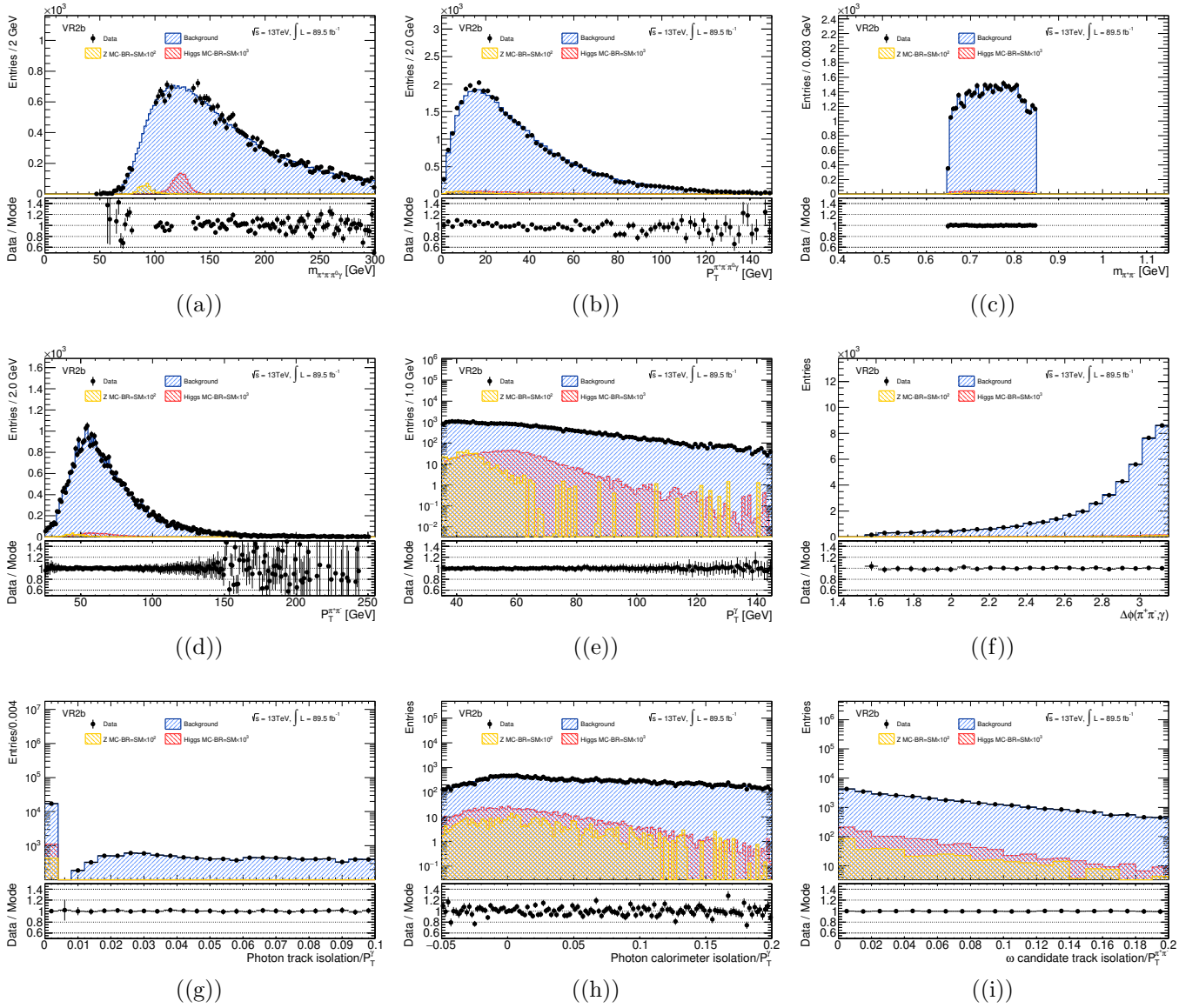

Figure 6.9: VR2b distributions of the background model, applying the photon track isolation requirement.

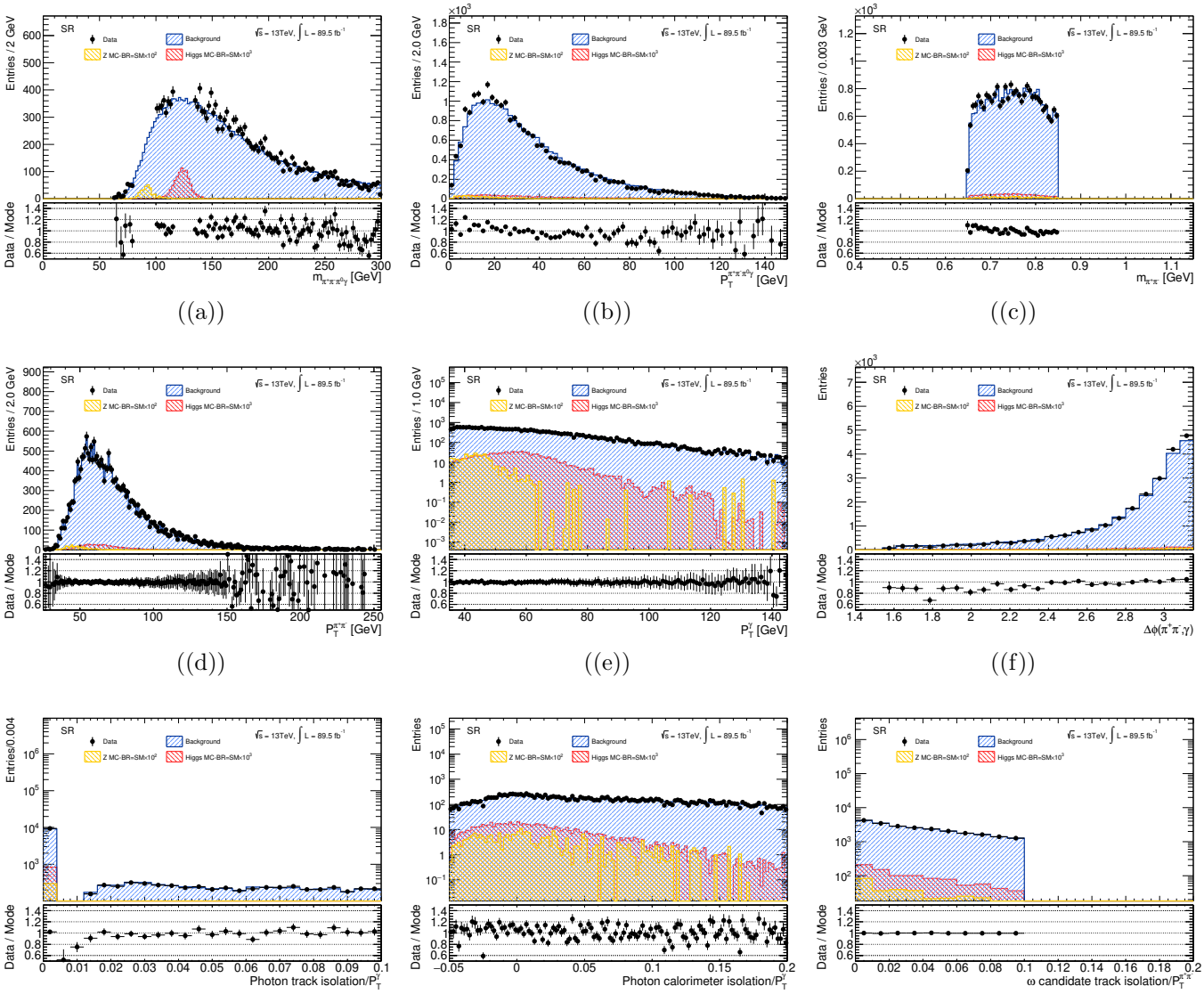

Figure 6.10: SR distributions of the background model, applying the full selection.

6.2.2 Background Model Validation with Shape Systematics

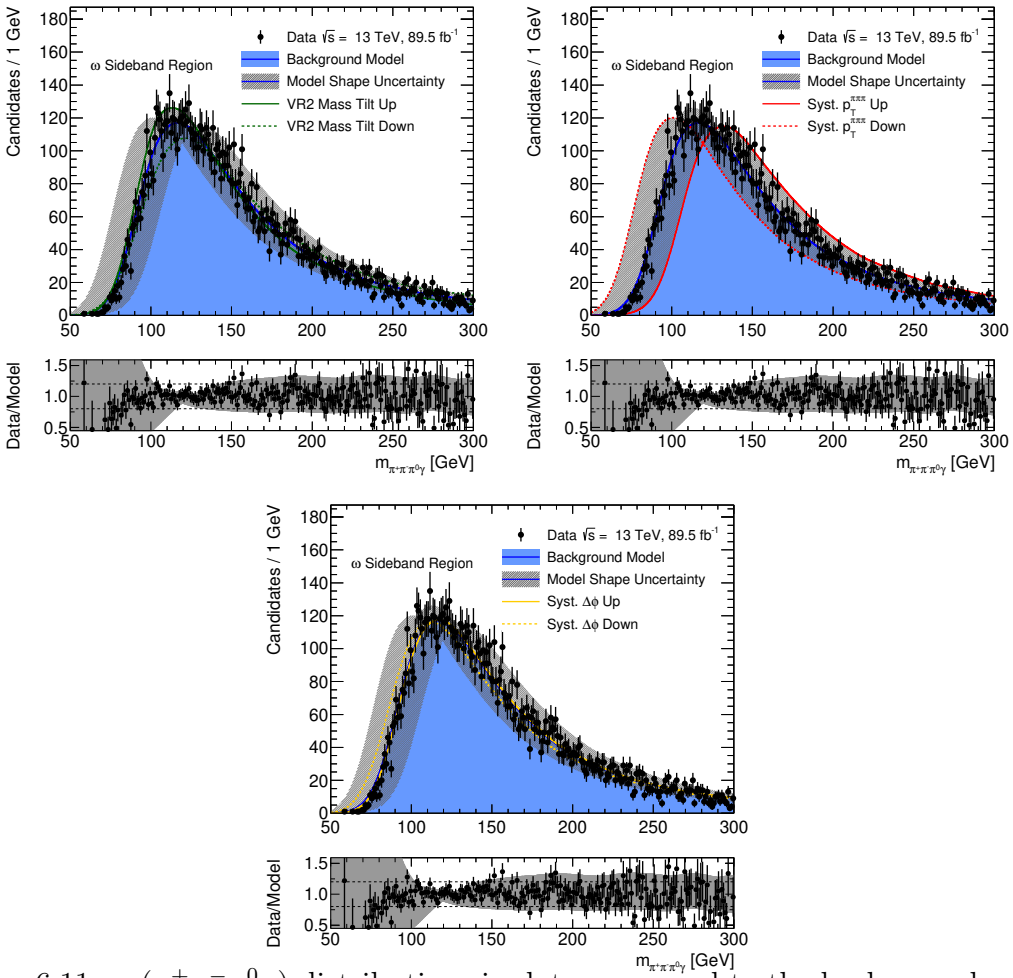

Figure 6.11: $m(\pi^+\pi^-\pi^0\gamma)$ distributions in data compared to the background model prediction. The systematic uncertainty band on the background represents the maximum deviation in the alternative background model from the nominal prediction, for each individual variation. The uncertainty on the ratio plots are not indicative of the interpolation that occurs within the fit, as they show the normalised curves of the shape variations.

To provide freedom to the inclusive background model to adjust to the observed, alternative shapes are derived, following the procedure in Section 5.4. These are shown in Figure 6.11.

6.3 Systematic Uncertainties

Systematic uncertainties are assigned as described in Section 5.5, which are input as nuisance parameters into the final fits. The theoretical systematic uncertainties have been described in Section 3.4.3.

6.3.1 Experimental systematic uncertainties

The systematic uncertainties are assigned in the same way as described in Section 6.3.1, with the only additional consideration being the uncertainty on the reconstruction of the neutral pion.

We find an efficiency to reconstruct the neutral pion in the decay using the tauPFO of approximately 65%, a plot of which is shown in Figure 6.12. The list of variables used in the BDT ID for tauPFO neutral pions is given in Table 3 in Ref. [100], where it shows that the variables are all shower variables in the EM calorimeter. Thus, in order to obtain an estimate of the modelling uncertainty, we use the corresponding photon identification efficiency uncertainties, which are given in Figure 7 of Ref [6]. The typical uncertainties range between 1-4%, so an uncertainty of 5% is applied as a signal nuisance parameter to cover the uncertainty of the neutral pion efficiency.

Due to the lack of dedicated π^0 reconstruction efficiency uncertainties in this context, we estimate the impact of this systematic on the expected limit by varying the magnitude of this systematic. We find that by increasing the systematic from 0.1% to 15% degrades the expected limit by only 4% for both the Higgs boson and Z boson channels, and since this is a statistics-dominated search, this functions sufficiently well as the systematic in this context.

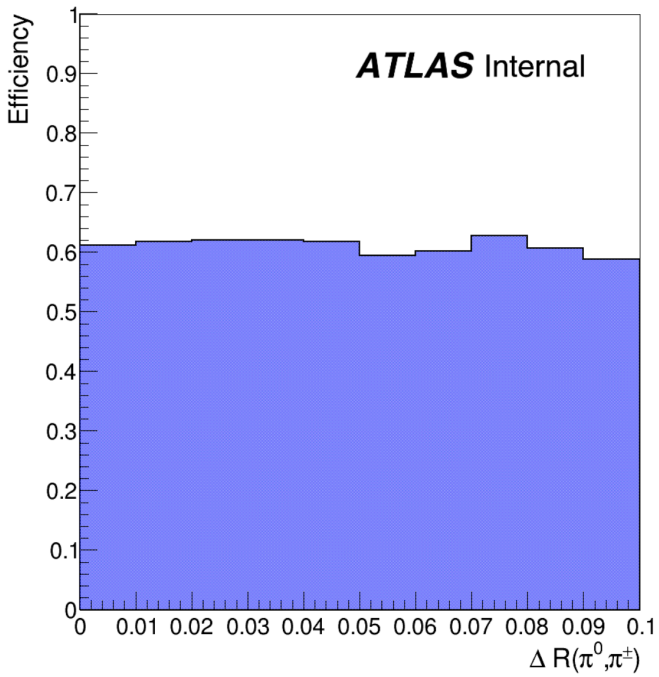

Figure 6.12: Efficiency to reconstruct the neutral pion in the $\omega \to \pi\pi\pi$ decay using the tauPFO as a function of the ΔR between the neutral pion and the closest pion track.

Experimental Systematic	Uncertainty (%)
Photon Reconstruction/Identification/Isolation	1.65
Photon Energy Scale / Resolution	0.11
Track Efficiency	2.4
Luminosity	1.7
Trigger Efficiency	0.17

Table 6.5: Experimental systematic uncertainties for the $H/Z \to \omega\gamma$ analysis.

6.4 Statistical analysis and expected sensitivity

The likelihood model, statistical interpretation, fitting procedure, and expected/obtained limits from the full unblinded dataset are presented in the following.

6.4.1 Fitting model

The fitting model is analogous to the one described in Section 5.6. The signal m_H distribution is modelled with a Gaussian + Crystal Ball, with the only discriminating variable used being $m_{\pi^+\pi^-\pi^0\gamma}$. During the fit, while one signal channel (H/Z) is being measured, the other is left free and is profiled.

The value of $\mu = 1$ corresponds to a branching ratio of 1.0×10^{-6} for the Higgs boson channel, and 1.0×10^{-9} for the Z boson channel.

6.4.2 Expected sensitivity

Expected sensitivities can be calculated for these decay channels using the same procedure as described in Section 5.6. The expected 95% CL upper limits on the branching ratios derived from the SR data, with and without systematics included, are shown in Table 6.6. The fit representing the median value of the expected limit including systematics is shown in Fig 6.13.

	Expected	$\pm1\sigma$	$\pm2\sigma$
Higgs [10^{-4}]			
No systematics	2.44	4.40/1.76	4.62/1.31
Shape+Norm	2.98	4.19/2.15	5.78/1.60
Z [10^{-7}]			
No systematics	2.96	4.12/2.13	5.63/1.59
Shape+Norm	5.42	7.87/3.90	10.61/2.91

Table 6.6: Expected branching ratio limits at the 95% CL for $H \to \omega\gamma$. The limits obtained including and excluding the systematics are compared.

6.4.3 Results

Background-only and signal-plus-background fits to data in a sideband of the ω mass have been performed with both background shape systematics and experimental signal systematics. The fit is shown in Fig 6.14, and the resulting fit parameters

are shown in Table 6.7, and demonstrate that the fitting procedure is robust and performs well.

After freezing the analysis strategy, the full dataset can be unblinded, and background-only and signal-plus-background fits can be performed. The parameter values from the final fits to data for both the background-only and also the signal-plus-background fits are shown in Table 6.8. The θ parameters correspond to the nuisance parameters for both the signal normalisation uncertainties as well as the background shape uncertainties. The μ parameters are the background and signal normalisations. No unexpected deviations are observed in the systematic uncertainties.

Following the full statistical procedure on the unblinded dataset, the observed 95% CL upper limit on the $H \to \omega\gamma$ channel is 1.0×10^{-4}. The corresponding observed 95% CL upper limit on the $Z \to \omega\gamma$ channel is 3.5×10^{-7}.

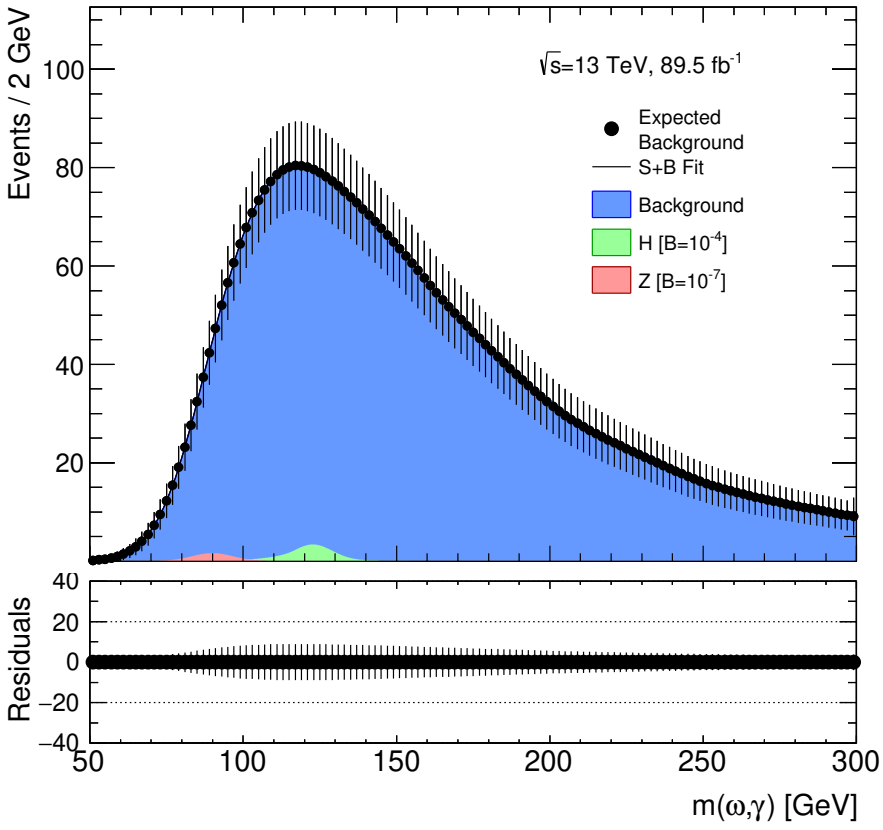

Figure 6.13: $m_{\pi^+\pi^-\pi^0\gamma}$ fit using Asimov data.

Parameter	Background		Signal+Background	
	Value	Error	Value	Error
θ_HZ_Lumi	0	1	1 $\times 10^{-4}$	1
θ_H_PDF_Scale	0	1	-2 $\times 10^{-5}$	1
θ_H_Ph_Eff	0	1	-9 $\times 10^{-6}$	1
θ_H_QCD_Scale	0	1	-3 $\times 10^{-5}$	1
θ_H_Trk_Eff	0	1	-9 $\times 10^{-5}$	1
θ_H_Tau_Unc	0	1	-1 $\times 10^{-5}$	1
θ_H_Trig_Unc	0	1	-1 $\times 10^{-6}$	1
θ_backgroundShape_DPHI_INC	2.24	0.48	2.21	0.43
θ_backgroundShape_DITRACKPT_INC	0.16	0.07	0.18	0.09
θ_backgroundShape_TILT_INC	0.76	0.22	0.91	0.23
μ_Mix_KDE_INC	0.92	0.01	0.94	0.01
μ_H	-	-	-484.0	264.0
μ_Z	-	-	-20.5	423.0

Table 6.7: Fit parameters for background-only and signal-plus-background fits to sideband meson mass data.

Parameter	Background		Signal+Background	
	Value	Error	Value	Error
θ_HZ_Lumi	0	1	-9 $\times 10^{-6}$	1
θ_H_PDF_Scale	0	1	-2 $\times 10^{-5}$	1
θ_H_Ph_Eff	0	1	-8 $\times 10^{-6}$	1
θ_H_QCD_Scale	0	1	-8 $\times 10^{-5}$	1
θ_H_Trk_Eff	0	1	-6 $\times 10^{-7}$	1
θ_H_Tau_Unc	0	1	-6 $\times 10^{-7}$	1
θ_backgroundShape_DPHI_INC	0.93	0.82	1.07	0.82
θ_backgroundShape_DITRACKPT_INC	0.23	0.13	0.19	0.17
θ_backgroundShape_TILT_INC	1.79	0.64	2.14	0.72
μ_Mix_KDE_INC	0.88	0.02	0.91	0.02
μ_H	-	-	-268.4	147.0
μ_Z	-	-	-265.9	285.0

Table 6.8: Fit parameters for background-only and signal-plus-background fits to data.

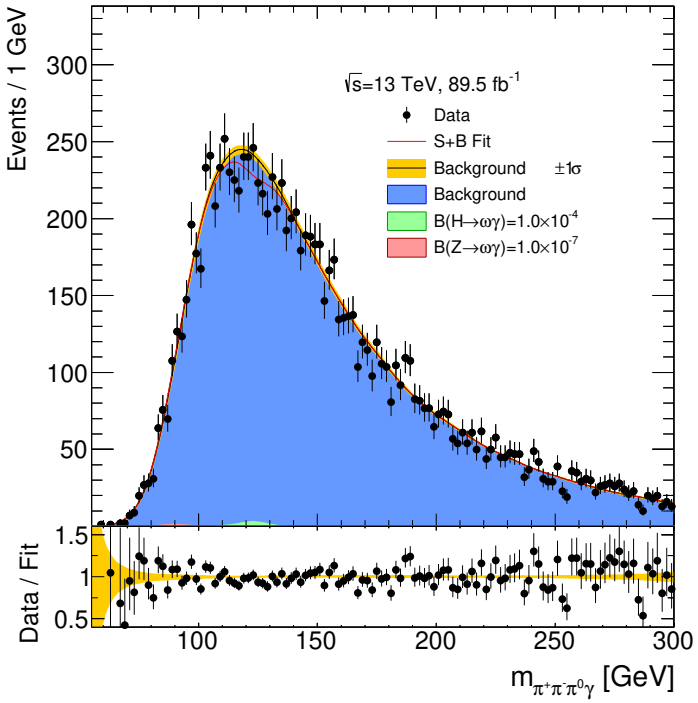

((a))

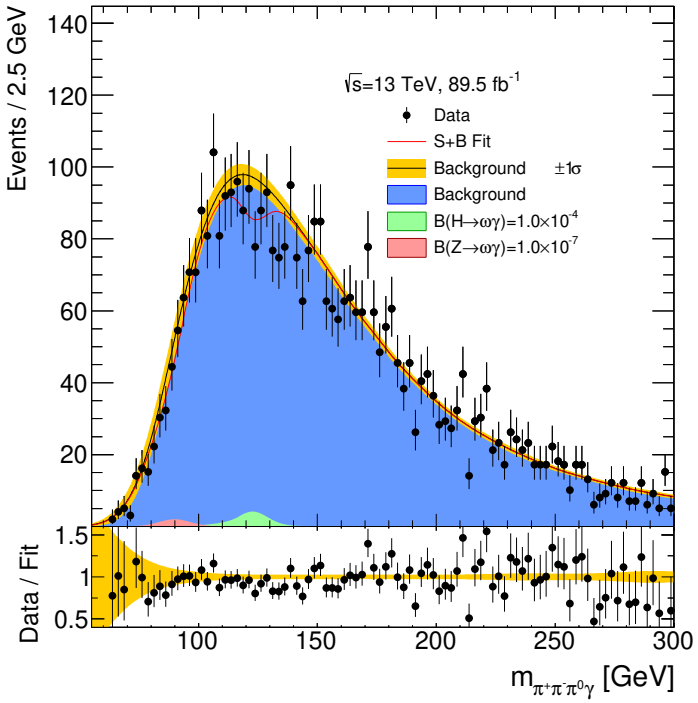

((b))

Figure 6.14: $m_{\omega\gamma}$ fit using (a) meson mass sideband data and (b) the full unblinded dataset.

CHAPTER 7

Conclusion

In this document, the status of rare Higgs boson decays to light mesons and quarkonium states within the ATLAS detector at the LHC has been presented. Constraints have been placed on the branching ratios for a number of decay channels.

The development and validation of certain τ-lepton algorithms within the ATLAS HLT has been undertaken, in particular the validation of the triggers used in 2018 data taking. The triggers have been active, and have successfully collected data for the experiment, which will feed directly into a wide range of analyses. Further improvement to these algorithms is underway in the form of the development of a Recurrent Neural Network to classify tracks from τ-lepton decays, which will be integrated into the trigger system for Run-3.

This thesis details the searches for the exclusive decays $H/Z \to \omega\gamma$ and $H \to K^*\gamma$. No significant excess of events were observed as a result of the analyses, and corresponding 95% confidence level upper limits were set on the branching fractions.

The limits for the decays $H/Z \to \omega\gamma$ were 1.01 $\times 10^{-4}$ and 3.53 $\times 10^{-7}$ respectively, assuming a SM Higgs boson production. This represents the first limit set on the Higgs boson decay channel to this final state, as well as a significant improvement over the previous result for the Z boson channel. The limit for the decay $H \to K^*\gamma$ was set at 8.91 $\times 10^{-5}$. This limit is the first limit set on flavour-violating exclusive decays of the Higgs boson to a meson and a photon.

REFERENCES

[1] J. Beringer *et al.*, "Review of Particle Physics (RPP)," *Phys. Rev.*, vol. D86, p. 010001, 2012.

[2] Y. Grossman, M. König, and M. Neubert, "Exclusive Radiative Decays of W and Z Bosons in QCD Factorization," *JHEP*, vol. 04, p. 101, 2015.

[3] M. König and M. Neubert, "Exclusive Radiative Higgs Decays as Probes of Light-Quark Yukawa Couplings," *JHEP*, vol. 08, p. 012, 2015.

[4] M. Aaboud *et al.*, "Search for exclusive Higgs and Z boson decays to $\phi\gamma$ and $\rho\gamma$ with the ATLAS detector," *JHEP*, vol. 07, p. 127, 2018.

[5] M. Aaboud *et al.*, "Searches for exclusive Higgs and Z boson decays into $J/\psi\gamma$, $\psi(2S)\gamma$, and $\Upsilon(nS)\gamma$ at $\sqrt{s} = 13$ TeV with the ATLAS detector," *Phys. Lett. B*, vol. 786, pp. 134–155, 2018.

[6] M. Aaboud *et al.*, "Measurement of the photon identification efficiencies with the ATLAS detector using LHC Run 2 data collected in 2015 and 2016," *Eur. Phys. J. C*, vol. 79, no. 3, p. 205, 2019.

[7] J. Ellis, "Higgs Physics," in *2013 European School of High-Energy Physics*, pp. 117–168, 2015.

[8] A. Djouadi, "The Anatomy of electro-weak symmetry breaking. I: The Higgs boson in the standard model," *Phys. Rept.*, vol. 457, pp. 1–216, 2008.

[9] "A combination of measurements of Higgs boson production and decay using up to 139 fb^{-1} of proton–proton collision data at $\sqrt{s} = 13$ TeV collected with the ATLAS experiment," *ATLAS-CONF-2020-027*, 8 2020.

[10] D. de Florian *et al.*, "Handbook of LHC Higgs Cross Sections: 4. Deciphering the Nature of the Higgs Sector," vol. 2/2017, 10 2016.

[11] G. F. Giudice and O. Lebedev, "Higgs-dependent Yukawa couplings," *Phys. Lett. B*, vol. 665, pp. 79–85, 2008.

[12] E. Mobs, "The CERN accelerator complex. Complexe des accélérateurs du CERN," Jul 2016. General Photo.

[13] G. Aad *et al.*, "Studies of the performance of the ATLAS detector using cosmic-ray muons," *Eur. Phys. J. C*, vol. 71, p. 1593, 2011.

[14] M. Aaboud *et al.*, "Performance of the ATLAS Track Reconstruction Algorithms in Dense Environments in LHC Run 2," *Eur. Phys. J. C*, vol. 77, no. 10, p. 673, 2017.

[15] ATLAS Collaboration, "Electron efficiency measurements in 2017 data and electron identification discriminating variables from 2016 data." `https://atlas.web.cern.ch/Atlas/GROUPS/PHYSICS/PLOTS/EGAM-2018-002/index.html`. [Accessed: 03-06-2019].

[16] ATLAS Collaboration, "Photon identification and isolation efficiency measurements in 2017 data." `https://atlas.web.cern.ch/Atlas/GROUPS/PHYSICS/PLOTS/EGAM-2018-007/index.html`. [Accessed: 03-06-2019].

[17] G. Aad *et al.*, "Muon reconstruction and identification efficiency in ATLAS using the full Run 2 *pp* collision data set at $\sqrt{s} = 13$ TeV," *Eur. Phys. J. C*, vol. 81, no. 7, p. 578, 2021.

[18] ATLAS Collaboration, "Trigger operation public results." `https://twiki.cern.ch/twiki/bin/view/AtlasPublic/TriggerOperationPublicResults`. [Accessed: 02-03-2022].

[19] J. I. Aranda, G. González-Estrada, J. Montaño, F. Ramírez-Zavaleta, and E. S. Tututi, "Revisiting the rare $h \to q_i q_j$ decays in the standard model," 2020.

[20] S. Weinberg, "A model of leptons," *Phys. Rev. Lett.*, vol. 19, pp. 1264–1266, Nov 1967.

[21] A. Salam, "Weak and Electromagnetic Interactions," *Conf. Proc.*, vol. C680519, pp. 367–377, 1968.

[22] G. Aad *et al.*, "Observation of a new particle in the search for the Standard Model Higgs boson with the ATLAS detector at the LHC," *Phys. Lett. B*, vol. 716, pp. 1–29, 2012.

[23] S. Chatrchyan *et al.*, "Observation of a New Boson at a Mass of 125 GeV with the CMS Experiment at the LHC," *Phys. Lett. B*, vol. 716, pp. 30–61, 2012.

[24] "LHC Machine," *JINST*, vol. 3, p. S08001, 2008.

[25] M. Aaboud *et al.*, "Evidence for the associated production of the Higgs boson and a top quark pair with the ATLAS detector," *Phys. Rev. D*, vol. 97, no. 7, p. 072003, 2018.

[26] A. M. Sirunyan *et al.*, "Observation of $t\bar{t}H$ production," *Phys. Rev. Lett.*, vol. 120, no. 23, p. 231801, 2018.

[27] M. Aaboud *et al.*, "Observation of $H \to b\bar{b}$ decays and VH production with the ATLAS detector," *Phys. Lett. B*, vol. 786, pp. 59–86, 2018.

[28] A. M. Sirunyan *et al.*, "Observation of Higgs boson decay to bottom quarks," *Phys. Rev. Lett.*, vol. 121, no. 12, p. 121801, 2018.

[29] M. Aaboud *et al.*, "Search for the Decay of the Higgs Boson to Charm Quarks with the ATLAS Experiment," *Phys. Rev. Lett.*, vol. 120, no. 21, p. 211802, 2018.

[30] P. W. Higgs, "Broken Symmetries and the Masses of Gauge Bosons," *Phys. Rev. Lett.*, vol. 13, pp. 508–509, 1964.

[31] F. Englert and R. Brout, "Broken Symmetry and the Mass of Gauge Vector Mesons," *Phys. Rev. Lett.*, vol. 13, pp. 321–323, 1964.

[32] R. Brout and F. Englert, "Spontaneous symmetry breaking in gauge theories: A Historical survey," in *1997 Europhysics Conference on High Energy Physics*, pp. 3–10, 2 1998.

[33] G. S. Guralnik, C. R. Hagen, and T. W. B. Kibble, "Global Conservation Laws and Massless Particles," *Phys. Rev. Lett.*, vol. 13, pp. 585–587, 1964.

[34] "Combined measurement of the total and differential cross sections in the $H \to \gamma\gamma$ and the $H \to ZZ^* \to 4\ell$ decay channels at $\sqrt{s} = 13$ TeV with the ATLAS detector," *ATLAS-CONF-2022-002*, 2022.

[35] M. Aaboud *et al.*, "Measurement of the Higgs boson mass in the $H \to ZZ^* \to 4\ell$ and $H \to \gamma\gamma$ channels with $\sqrt{s} = 13$ TeV pp collisions using the ATLAS detector," *Phys. Lett. B*, vol. 784, pp. 345–366, 2018.

[36] A. M. Sirunyan *et al.*, "Measurements of properties of the Higgs boson decaying into the four-lepton final state in pp collisions at $\sqrt{s} = 13$ TeV," *JHEP*, vol. 11, p. 047, 2017.

[37] A. M. Sirunyan *et al.*, "Measurements of Higgs boson properties in the diphoton decay channel in proton-proton collisions at $\sqrt{s} = 13$ TeV," *JHEP*, vol. 11, p. 185, 2018.

[38] G. Aad *et al.*, "Combined Measurement of the Higgs Boson Mass in pp Collisions at $\sqrt{s} = 7$ and 8 TeV with the ATLAS and CMS Experiments," *Phys. Rev. Lett.*, vol. 114, p. 191803, 2015.

[39] G. Aad *et al.*, "Evidence for the Higgs-boson Yukawa coupling to tau leptons with the ATLAS detector," *JHEP*, vol. 04, p. 117, 2015.

[40] A. M. Sirunyan *et al.*, "Observation of the Higgs boson decay to a pair of τ leptons with the CMS detector," *Phys. Lett. B*, vol. 779, pp. 283–316, 2018.

[41] G. Aad *et al.*, "A search for the dimuon decay of the Standard Model Higgs boson with the ATLAS detector," *Phys. Lett. B*, vol. 812, p. 135980, 2021.

[42] A. M. Sirunyan *et al.*, "Evidence for Higgs boson decay to a pair of muons," *JHEP*, vol. 01, p. 148, 2021.

[43] G. Aad *et al.*, "Direct constraint on the Higgs-charm coupling from a search for Higgs boson decays into charm quarks with the ATLAS detector," *Submitted to Eur. Phys. J. C*, 2022.

[44] A. M. Sirunyan *et al.*, "A search for the standard model Higgs boson decaying to charm quarks," *JHEP*, vol. 03, p. 131, 2020.

[45] L. Randall and R. Sundrum, "A Large mass hierarchy from a small extra dimension," *Phys. Rev. Lett.*, vol. 83, pp. 3370–3373, 1999.

[46] G. D'Ambrosio, G. F. Giudice, G. Isidori, and A. Strumia, "Minimal flavor violation: An Effective field theory approach," *Nucl. Phys. B*, vol. 645, pp. 155–187, 2002.

[47] C. D. Froggatt and H. B. Nielsen, "Hierarchy of Quark Masses, Cabibbo Angles and CP Violation," *Nucl. Phys. B*, vol. 147, pp. 277–298, 1979.

[48] M. J. Dugan, H. Georgi, and D. B. Kaplan, "Anatomy of a Composite Higgs Model," *Nucl. Phys. B*, vol. 254, pp. 299–326, 1985.

[49] N. N. Achasov, "The Z —> c anti-c —> gamma gamma*, Z —> b anti-b —> gamma gamma* triangle diagrams and the Z —> gamma psi, Z —> gamma Ypsilon decays," *Theor. Math. Phys.*, vol. 170, pp. 39–51, 2012.

[50] T.-C. Huang and F. Petriello, "Rare exclusive decays of the Z-boson revisited," *Phys. Rev. D*, vol. 92, no. 1, p. 014007, 2015.

[51] I. Brivio, F. Goertz, and G. Isidori, "Probing the Charm Quark Yukawa Coupling in Higgs+Charm Production," *Phys. Rev. Lett.*, vol. 115, no. 21, p. 211801, 2015.

[52] F. Yu, "Phenomenology of Enhanced Light Quark Yukawa Couplings and the $W^{\pm}h$ Charge Asymmetry," *JHEP*, vol. 02, p. 083, 2017.

[53] Y. Soreq, H. X. Zhu, and J. Zupan, "Light quark Yukawa couplings from Higgs kinematics," *JHEP*, vol. 12, p. 045, 2016.

[54] F. Bishara, U. Haisch, P. F. Monni, and E. Re, "Constraining Light-Quark Yukawa Couplings from Higgs Distributions," *Phys. Rev. Lett.*, vol. 118, no. 12, p. 121801, 2017.

[55] G. T. Bodwin, F. Petriello, S. Stoynev, and M. Velasco, "Higgs boson decays to quarkonia and the $H\bar{c}c$ coupling," *Phys. Rev. D*, vol. 88, no. 5, p. 053003, 2013.

[56] A. L. Kagan, G. Perez, F. Petriello, Y. Soreq, S. Stoynev, and J. Zupan, "Exclusive Window onto Higgs Yukawa Couplings," *Phys. Rev. Lett.*, vol. 114, no. 10, p. 101802, 2015.

[57] Y. Grossman, M. König, and M. Neubert, "Exclusive Radiative Decays of W and Z Bosons in QCD Factorization," *JHEP*, vol. 04, p. 101, 2015.

[58] G. T. Bodwin, H. S. Chung, J.-H. Ee, and J. Lee, "Z-boson decays to a vector quarkonium plus a photon," *Phys. Rev. D*, vol. 97, no. 1, p. 016009, 2018.

[59] G. T. Bodwin, H. S. Chung, J.-H. Ee, and J. Lee, "Addendum: New approach to the resummation of logarithms in Higgs-boson decays to a vector quarkonium plus a photon [Phys. Rev. D 95, 054018 (2017)]," *Phys. Rev. D*, vol. 96, p. 116014, 2017.

[60] G. T. Bodwin, H. S. Chung, J.-H. Ee, J. Lee, and F. Petriello, "Relativistic corrections to Higgs boson decays to quarkonia," *Phys. Rev. D*, vol. 90, no. 11, p. 113010, 2014.

[61] A. M. Sirunyan *et al.*, "Search for rare decays of Z and Higgs bosons to J/ψ and a photon in proton-proton collisions at $\sqrt{s} = 13$ TeV," *Eur. Phys. J. C*, vol. 79, no. 2, p. 94, 2019.

[62] A. M. Sirunyan *et al.*, "Search for decays of the 125 GeV Higgs boson into a Z boson and a ρ or ϕ meson," *JHEP*, vol. 11, p. 039, 2020.

[63] G. Aad *et al.*, "Search for Higgs and Z Boson Decays to J/$\psi\gamma$ and $\Upsilon(nS)\gamma$ with the ATLAS Detector," *Phys. Rev. Lett.*, vol. 114, no. 12, p. 121801, 2015.

[64] M. Aaboud *et al.*, "Search for Higgs and Z Boson Decays to $\phi\,\gamma$ with the ATLAS Detector," *Phys. Rev. Lett.*, vol. 117, no. 11, p. 111802, 2016.

[65] C. Oleari, "The POWHEG-BOX," *Nucl. Phys. B Proc. Suppl.*, vol. 205-206, pp. 36–41, 2010.

[66] T. Sjostrand, S. Mrenna, and P. Z. Skands, "A Brief Introduction to PYTHIA 8.1," *Comput. Phys. Commun.*, vol. 178, pp. 852–867, 2008.

[67] R. Kutschke, "An Angular Distribution Cookbook," 1996.

[68] *LEP design report.* Geneva: CERN, 1984. Copies shelved as reports in LEP, PS and SPS libraries.

[69] G. Aad *et al.*, "The ATLAS Experiment at the CERN Large Hadron Collider," *JINST*, vol. 3, p. S08003, 2008.

[70] M. Capeans, G. Darbo, K. Einsweiler, M. Elsing, T. Flick, M. Garcia-Sciveres, C. Gemme, H. Pernegger, O. Rohne, and R. Vuillermet, "ATLAS Insertable B-Layer Technical Design Report," 9 2010.

[71] "Electron efficiency measurements with the ATLAS detector using the 2015 LHC proton-proton collision data," 6 2016.

[72] M. Aaboud *et al.*, "Measurement of the photon identification efficiencies with the ATLAS detector using LHC Run-1 data," *Eur. Phys. J. C*, vol. 76, no. 12, p. 666, 2016.

[73] A. R. Martínez, "The Run-2 ATLAS Trigger System," *J. Phys. Conf. Ser.*, vol. 762, no. 1, p. 012003, 2016.

[74] S. Alioli, P. Nason, C. Oleari, and E. Re, "NLO Higgs boson production via gluon fusion matched with shower in POWHEG," *JHEP*, vol. 04, p. 002, 2009.

[75] P. Nason and C. Oleari, "NLO Higgs boson production via vector-boson fusion matched with shower in POWHEG," *JHEP*, vol. 02, p. 037, 2010.

[76] T. Sjostrand, S. Mrenna, and P. Z. Skands, "PYTHIA 6.4 Physics and Manual," *JHEP*, vol. 05, p. 026, 2006.

[77] H.-L. Lai, M. Guzzi, J. Huston, Z. Li, P. M. Nadolsky, J. Pumplin, and C. P. Yuan, "New parton distributions for collider physics," *Phys. Rev. D*, vol. 82, p. 074024, 2010.

[78] S. Dittmaier *et al.*, "Handbook of LHC Higgs Cross Sections: 1. Inclusive Observables," *CERN-2011-002*, 1 2011.

[79] S. Dittmaier *et al.*, "Handbook of LHC Higgs Cross Sections: 2. Differential Distributions," *CERN-2012-002*, 1 2012.

[80] J. R. Andersen *et al.*, "Handbook of LHC Higgs Cross Sections: 3. Higgs Properties," *CERN-2013-004*, 7 2013.

[81] G. Aad *et al.*, "Measurement of $W^{\pm}$ and Z-boson production cross sections in pp collisions at $\sqrt{s} = 13$ TeV with the ATLAS detector," *Phys. Lett. B*, vol. 759, pp. 601–621, 2016.

[82] "Search for Minimal Supersymmetric Standard Model Higgs Bosons H/A in the $\tau\tau$ final state in up to 13.3 fb^1 of pp collisions at $\sqrt{s}$= 13 TeV with the ATLAS Detector," 8 2016.

[83] M. Aaboud *et al.*, "Search for charged Higgs bosons produced in association with a top quark and decaying via $H^{\pm} \to \tau\nu$ using pp collision data recorded at $\sqrt{s} = 13$ TeV by the ATLAS detector," *Phys. Lett. B*, vol. 759, pp. 555–574, 2016.

[84] M. Aaboud *et al.*, "Search for squarks and gluinos in events with hadronically decaying tau leptons, jets and missing transverse momentum in proton–proton collisions at $\sqrt{s} = 13$ TeV recorded with the ATLAS detector," *Eur. Phys. J. C*, vol. 76, no. 12, p. 683, 2016.

[85] ATLAS Collaboration, "The ATLAS Tau Trigger in Run 2," Tech. Rep. ATLAS-CONF-2017-061, CERN, Geneva, Jul 2017.

[86] A. Sherstinsky, "Fundamentals of recurrent neural network (RNN) and long short-term memory (LSTM) network," *CoRR*, vol. abs/1808.03314, 2018.

[87] S. Hochreiter and J. Schmidhuber, "Long short-term memory," *Neural computation*, vol. 9, pp. 1735–80, 12 1997.

[88] A. Graves, A. Mohamed, and G. E. Hinton, "Speech recognition with deep recurrent neural networks," *CoRR*, vol. abs/1303.5778, 2013.

[89] J. T. Connor, R. D. Martin, and L. E. Atlas, "Recurrent neural networks and robust time series prediction," *IEEE Transactions on Neural Networks*, vol. 5, pp. 240–254, March 1994.

[90] K. Cho, B. van Merrienboer, Ç. Gülçehre, F. Bougares, H. Schwenk, and Y. Bengio, "Learning phrase representations using RNN encoder-decoder for statistical machine translation," *CoRR*, vol. abs/1406.1078, 2014.

[91] F. Chollet *et al.*, "Keras." `https://keras.io`, 2015.

[92] Theano Development Team, "Theano: A Python framework for fast computation of mathematical expressions," *arXiv e-prints*, vol. abs/1605.02688, May 2016.

[93] M. Abadi *et al.*, "TensorFlow: Large-scale machine learning on heterogeneous systems," 2015. Software available from tensorflow.org.

[94] J. I. Aranda, G. González-Estrada, J. Montaño, F. Ramírez-Zavaleta, and E. S. Tututi, "Revisiting the rare $H \to q_i q_j$ decays in the standard model," *J. Phys. G*, vol. 47, no. 12, p. 125001, 2020.

[95] G. Aad *et al.*, "Electron and photon performance measurements with the ATLAS detector using the 2015–2017 LHC proton-proton collision data," *JINST*, vol. 14, no. 12, p. P12006, 2019.

[96] M. Baak, S. Gadatsch, R. Harrington, and W. Verkerke, "Interpolation between multi-dimensional histograms using a new non-linear moment morphing method," *Nucl. Instrum. Meth. A*, vol. 771, pp. 39–48, 2015.

[97] A. L. Read, "Presentation of search results: The CL(s) technique," *J. Phys. G*, vol. 28, pp. 2693–2704, 2002.

[98] J. Neyman and E. S. Pearson, "On the Problem of the Most Efficient Tests of Statistical Hypotheses," *Phil. Trans. Roy. Soc. Lond. A*, vol. 231, no. 694-706, pp. 289–337, 1933.

[99] G. Cowan, K. Cranmer, E. Gross, and O. Vitells, "Asymptotic formulae for likelihood-based tests of new physics," *Eur. Phys. J. C*, vol. 71, p. 1554, 2011. [Erratum: Eur.Phys.J.C 73, 2501 (2013)].

[100] G. Aad *et al.*, "Reconstruction of hadronic decay products of tau leptons with the ATLAS experiment," *Eur. Phys. J. C*, vol. 76, no. 5, p. 295, 2016.

APPENDIX A

Background Model Validation

A.1 Sideband Data Validation

To validate the background model, the $m_{\mathcal{M}\gamma}$ distributions in validation regions, defined by kinematic and isolation requirements looser than the nominal signal requirements, are used to compare the prediction of the background model with the data. Three validation regions are defined, each based on the GR selection and adding one of the following: the meson isolation requirement (VR1), the calorimeter component of the photon isolation requirements (VR2a), or the track component of the photon isolation requirements (VR2b). The $m_{\mathcal{M}\gamma}$ distributions in these validation regions are shown in Figure A.1. The background model is found to describe the data in all regions within uncertainties.

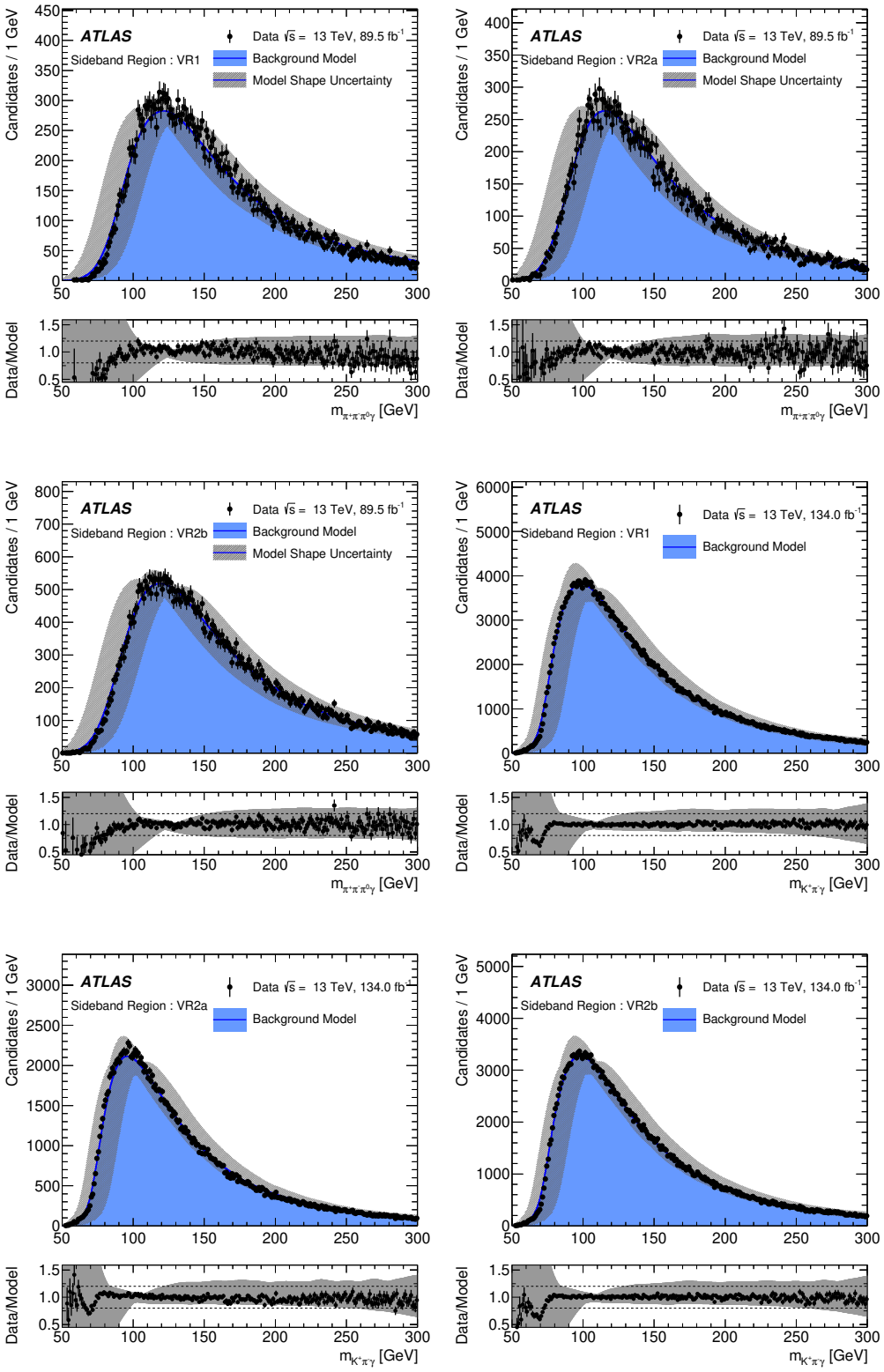

Figure A.1: Distributions of $m_{K\pi\gamma}$ and $m_{\pi\pi\pi\gamma}$ in data compared to the prediction of the background model for the VR1, VR2a and VR2b validation regions. The background model is normalised to the observed number of events within the region shown. The uncertainty band corresponds to the uncertainty envelope derived from variations in the background modelling procedure, described in Section 5.3. The ratio of the data to the background model is shown below the distributions.

APPENDIX B

Generator level distributions

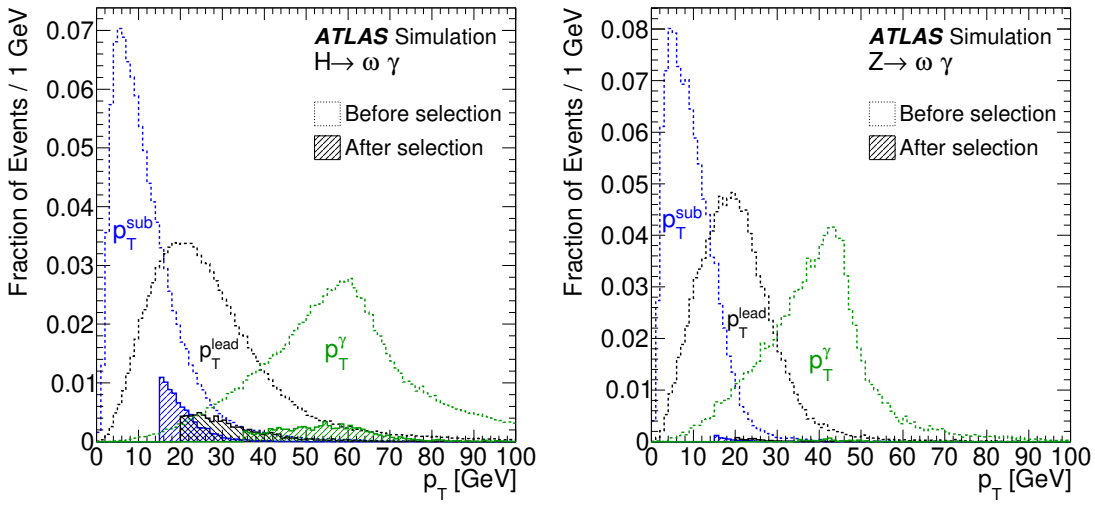

(a)

(b)

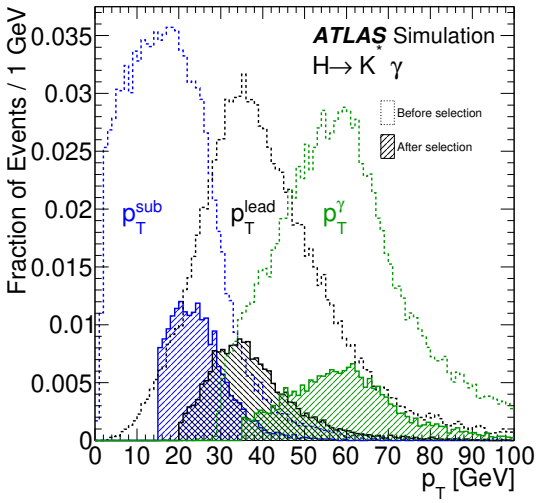

(c)

Figure B.1: Generator-level transverse momentum (p_{T}) distributions of the photon and charged-hadron candidates for (a) $H \to \omega\gamma$, (b) $Z \to \omega\gamma$ and (c) $H \to K^{*}\gamma$ simulated events, respectively. The dashed-line distributions with a clear fill show the events at generator level which fall within the analysis geometric acceptance (both charged-hadron candidates are required to have $|\eta| < 2.5$, while the photon is required to have $|\eta| < 2.37$, excluding the region $1.37 < |\eta| < 1.52$, and are each normalised to unity. The solid-line distributions with a hatched fill show the fraction of these events which pass the full analysis event selection. The relative difference between the two sets of distributions corresponds to the effects of reconstruction, trigger, and event selection efficiencies.

APPENDIX C

K^* Signal Systematics

Systematic name	Normalisation	Mean	Std Dev
EG_RESOLUTION_AF2__1down	0.0086%	0.0021%	0.4545%
EG_RESOLUTION_AF2__1up	0.0947%	0.0038%	1.1815%
EG_RESOLUTION_MATERIALCALO__1down	0.0043%	0.0004%	0.0526%
EG_RESOLUTION_MATERIALCALO__1up	0.0000%	0.0000%	0.0228%
EG_RESOLUTION_MATERIALCRYO__1down	0.0086%	0.0008%	0.1385%
EG_RESOLUTION_MATERIALCRYO__1up	0.0215%	0.0006%	0.1637%
EG_RESOLUTION_MATERIALGAP__1down	0.0000%	0.0000%	0.1741%
EG_RESOLUTION_MATERIALGAP__1up	0.0000%	0.0000%	0.1350%
EG_RESOLUTION_MATERIALIBL__1down	0.0043%	0.0007%	0.0982%
EG_RESOLUTION_MATERIALIBL__1up	0.0086%	0.0005%	0.0914%
EG_RESOLUTION_MATERIALID__1down	0.0043%	0.0014%	0.4780%
EG_RESOLUTION_MATERIALID__1up	0.0560%	0.0020%	0.4714%
EG_RESOLUTION_MATERIALPP0__1down	0.0043%	0.0020%	0.3179%
EG_RESOLUTION_MATERIALPP0__1up	0.0215%	0.0008%	0.4707%
EG_RESOLUTION_PILEUP__1down	0.0172%	0.0016%	0.2349%
EG_RESOLUTION_PILEUP__1up	0.0172%	0.0017%	0.2368%
EG_RESOLUTION_SAMPLINGTERM__1down	0.0129%	0.0004%	0.1270%
EG_RESOLUTION_SAMPLINGTERM__1up	0.0043%	0.0009%	0.2332%
EG_RESOLUTION_ZSMEARING__1down	0.0043%	0.0014%	0.3074%
EG_RESOLUTION_ZSMEARING__1up	0.0258%	0.0017%	0.3735%

Table C.1: E/gamma resolution systematics

Systematic name	Normalisation	Mean	Std Dev
EG_SCALE_AF2__1down	0.0689%	0.0487%	0.0501%
EG_SCALE_AF2__1up	0.0301%	0.0478%	0.0098%
EG_SCALE_E4SCINTILLATOR__1down	0.0043%	0.0019%	0.0028%
EG_SCALE_E4SCINTILLATOR__1up	0.0043%	0.0021%	0.0151%
EG_SCALE_G4__1down	0.0129%	0.0066%	0.0063%
EG_SCALE_G4__1up	0.0086%	0.0070%	0.0101%
EG_SCALE_L1GAIN__1down	0.0431%	0.0237%	0.0386%
EG_SCALE_L1GAIN__1up	0.0129%	0.0232%	0.0783%
EG_SCALE_L2GAIN__1down	0.0086%	0.0471%	0.0261%
EG_SCALE_L2GAIN__1up	0.0215%	0.0463%	0.0999%
EG_SCALE_LARCALIB__1down	0.0172%	0.0448%	0.1242%
EG_SCALE_LARCALIB__1up	0.0603%	0.0468%	0.0908%
EG_SCALE_LARELECCALIB__1down	0.0086%	0.0029%	0.0040%
EG_SCALE_LARELECCALIB__1up	0.0000%	0.0028%	0.0018%
EG_SCALE_LARELECUNCONV__1down	0.0129%	0.0594%	0.0326%
EG_SCALE_LARELECUNCONV__1up	0.0388%	0.0603%	0.0031%
EG_SCALE_LARUNCONVCALIB__1down	0.0129%	0.0178%	0.0095%
EG_SCALE_LARUNCONVCALIB__1up	0.0000%	0.0190%	0.0358%
EG_SCALE_MATCALO__1down	0.0344%	0.0189%	0.0184%
EG_SCALE_MATCALO__1up	0.0000%	0.0198%	0.0508%
EG_SCALE_MATCRYO__1down	0.0431%	0.0325%	0.0376%
EG_SCALE_MATCRYO__1up	0.0000%	0.0328%	0.0161%
EG_SCALE_MATID__1down	0.0431%	0.0234%	0.1222%
EG_SCALE_MATID__1up	0.0129%	0.0232%	0.0856%
EG_SCALE_MATPP0__1down	0.0258%	0.0133%	0.1075%
EG_SCALE_MATPP0__1up	0.0129%	0.0131%	0.0730%
EG_SCALE_PEDESTAL__1down	0.0043%	0.0040%	0.0075%
EG_SCALE_PEDESTAL__1up	0.0086%	0.0039%	0.0015%
EG_SCALE_PS__1down	0.0086%	0.0584%	0.0735%
EG_SCALE_PS__1up	0.0603%	0.0593%	0.2508%
EG_SCALE_PS_BARREL_B12__1down	0.0043%	0.0290%	0.0372%
EG_SCALE_PS_BARREL_B12__1up	0.0258%	0.0291%	0.0787%
EG_SCALE_S12__1down	0.0043%	0.0443%	0.1011%
EG_SCALE_S12__1up	0.0517%	0.0457%	0.0787%
EG_SCALE_TOPOCLUSTER_THRES__1down	0.0000%	0.0000%	0.0000%
EG_SCALE_TOPOCLUSTER_THRES__1up	0.0043%	0.0040%	0.0075%
EG_SCALE_WTOTS1__1down	0.0258%	0.0170%	0.0088%
EG_SCALE_WTOTS1__1up	0.0086%	0.0158%	0.1083%
EG_SCALE_ZEESTAT__1down	0.0172%	0.0058%	0.0389%
EG_SCALE_ZEESTAT__1up	0.0043%	0.0064%	0.0156%
EG_SCALE_ZEESYST__1down	0.0431%	0.0307%	0.1031%
EG_SCALE_ZEESYST__1up	0.0043%	0.0304%	0.0627%

Table C.2: E/gamma scale systematics

Systematic name	Normalisation	Mean	Std Dev
PH_SCALE_CONVFAKERATE__1down	0.0086%	0.0063%	0.0231%
PH_SCALE_CONVFAKERATE__1up	0.0043%	0.0072%	0.0195%
PH_SCALE_CONVRADIUS__1down	0.0043%	0.0108%	0.1000%
PH_SCALE_CONVRADIUS__1up	0.0172%	0.0100%	0.0673%
PH_SCALE_LEAKAGECONV__1down	0.0172%	0.0211%	0.0000%
PH_SCALE_LEAKAGECONV__1up	0.0129%	0.0218%	0.0922%
PH_SCALE_LEAKAGEUNCONV__1down	0.0344%	0.0309%	0.0533%
PH_SCALE_LEAKAGEUNCONV__1up	0.0129%	0.0304%	0.0722%

Table C.3: Photon scale systematics

Systematic name	Normalisation	Mean	Std Dev
TRK_BIAS_D0_WM	0.0000%	0.0000%	0.0000%
TRK_BIAS_QOVERP_SAGITTA_WM	0.0000%	0.0000%	0.0000%
TRK_BIAS_Z0_WM	0.0000%	0.0000%	0.0000%
TRK_EFF_LOOSE_GLOBAL	1.1195%	0.0004%	0.1652%
TRK_EFF_LOOSE_IBL	0.7837%	0.0002%	0.0175%
TRK_EFF_LOOSE_PHYSMODEL	0.6976%	0.0022%	0.0444%
TRK_EFF_LOOSE_PP0	0.2713%	0.0004%	0.1389%
TRK_EFF_TIGHT_GLOBAL	1.7137%	0.0015%	0.2057%
TRK_EFF_TIGHT_IBL	0.9688%	0.0023%	0.0608%
TRK_EFF_TIGHT_PHYSMODEL	1.0291%	0.0016%	0.0105%
TRK_EFF_TIGHT_PP0	0.3531%	0.0005%	0.1675%
TRK_FAKE_RATE_LOOSE	0.1292%	0.0006%	0.2093%
TRK_FAKE_RATE_LOOSE_ROBUST	0.1765%	0.0004%	0.0189%
TRK_FAKE_RATE_TIGHT	1.1970%	0.0036%	1.2540%
TRK_RES_D0_DEAD	0.0000%	0.0000%	0.0000%
TRK_RES_D0_MEAS	0.0000%	0.0000%	0.0000%
TRK_RES_Z0_DEAD	0.0000%	0.0000%	0.0000%
TRK_RES_Z0_MEAS	0.0000%	0.0000%	0.0000%

Table C.4: Track systematics

APPENDIX D

ω Signal Systematics

Systematic name	Normalisation	Mean	Std Dev
EG_RESOLUTION_AF2__1down	0.000000%	0.000000%	0.000000%
EG_RESOLUTION_AF2__1up	0.000000%	0.000000%	0.000000%
EG_RESOLUTION_MATERIALCALO__1down	0.000000%	0.000144%	0.014513%
EG_RESOLUTION_MATERIALCALO__1up	0.005468%	0.000258%	0.012682%
EG_RESOLUTION_MATERIALCRYO__1down	0.000000%	0.001045%	0.072474%
EG_RESOLUTION_MATERIALCRYO__1up	0.010936%	0.000563%	0.029039%
EG_RESOLUTION_MATERIALGAP__1down	0.000000%	0.000458%	0.015553%
EG_RESOLUTION_MATERIALGAP__1up	0.016403%	0.001065%	0.002271%
EG_RESOLUTION_MATERIALIBL__1down	0.021871%	0.003816%	0.014015%
EG_RESOLUTION_MATERIALIBL__1up	0.005468%	0.000141%	0.040349%
EG_RESOLUTION_MATERIALID__1down	0.032807%	0.004657%	0.067840%
EG_RESOLUTION_MATERIALID__1up	0.032807%	0.001381%	0.119461%
EG_RESOLUTION_MATERIALPP0__1down	0.010936%	0.000568%	0.099856%
EG_RESOLUTION_MATERIALPP0__1up	0.021871%	0.000191%	0.052563%
EG_RESOLUTION_PILEUP__1down	0.010936%	0.000881%	0.068697%
EG_RESOLUTION_PILEUP__1up	0.010936%	0.004688%	0.007086%
EG_RESOLUTION_SAMPLINGTERM__1down	0.010936%	0.000621%	0.038230%
EG_RESOLUTION_SAMPLINGTERM__1up	0.010936%	0.003715%	0.034695%
EG_RESOLUTION_ZSMEARING__1down	0.021871%	0.003679%	0.007707%
EG_RESOLUTION_ZSMEARING__1up	0.032807%	0.000641%	0.117474%

Table D.1: E/gamma resolution systematics

Systematic name	Normalisation	Mean	Std Dev
EG_SCALE_AF2__1down	0.000000%	0.000000%	0.000000%
EG_SCALE_AF2__1up	0.000000%	0.000000%	0.000000%
EG_SCALE_E4SCINTILLATOR__1down	0.000000%	0.001905%	0.002985%
EG_SCALE_E4SCINTILLATOR__1up	0.000000%	0.001907%	0.002385%
EG_SCALE_G4__1down	0.005468%	0.006447%	0.011139%
EG_SCALE_G4__1up	0.000000%	0.006422%	0.008498%
EG_SCALE_L1GAIN__1down	0.005468%	0.018496%	0.009812%
EG_SCALE_L1GAIN__1up	0.010936%	0.017263%	0.006639%
EG_SCALE_L2GAIN__1down	0.016403%	0.034366%	0.062545%
EG_SCALE_L2GAIN__1up	0.016403%	0.036827%	0.144641%
EG_SCALE_LARCALIB__1down	0.038274%	0.043965%	0.086311%
EG_SCALE_LARCALIB__1up	0.016403%	0.042536%	0.050666%
EG_SCALE_LARELECCALIB__1down	0.005468%	0.002392%	0.001265%
EG_SCALE_LARELECCALIB__1up	0.000000%	0.002151%	0.000513%
EG_SCALE_LARELECUNCONV__1down	0.027339%	0.058213%	0.094535%
EG_SCALE_LARELECUNCONV__1up	0.032807%	0.052886%	0.018479%
EG_SCALE_LARUNCONVCALIB__1down	0.000000%	0.015602%	0.012018%
EG_SCALE_LARUNCONVCALIB__1up	0.010936%	0.017387%	0.044366%
EG_SCALE_MATCALO__1down	0.005468%	0.017421%	0.007392%
EG_SCALE_MATCALO__1up	0.010936%	0.019001%	0.047023%
EG_SCALE_MATCRYO__1down	0.010936%	0.030289%	0.039868%
EG_SCALE_MATCRYO__1up	0.010936%	0.032054%	0.059821%
EG_SCALE_MATID__1down	0.021871%	0.020451%	0.006371%
EG_SCALE_MATID__1up	0.027339%	0.021736%	0.051489%
EG_SCALE_MATPP0__1down	0.010936%	0.011202%	0.017649%
EG_SCALE_MATPP0__1up	0.005468%	0.011721%	0.004373%
EG_SCALE_PEDESTAL__1down	0.000000%	0.003408%	0.008311%
EG_SCALE_PEDESTAL__1up	0.000000%	0.003409%	0.008298%
EG_SCALE_PS__1down	0.027339%	0.056428%	0.132131%
EG_SCALE_PS__1up	0.027339%	0.052920%	0.067966%
EG_SCALE_PS_BARREL_B12__1down	0.027339%	0.029568%	0.074807%
EG_SCALE_PS_BARREL_B12__1up	0.005468%	0.026108%	0.001886%
EG_SCALE_S12__1down	0.032807%	0.041533%	0.079174%
EG_SCALE_S12__1up	0.010936%	0.040319%	0.037389%
EG_SCALE_TOPOCLUSTER_THRES__1down	0.000000%	0.000000%	0.000000%
EG_SCALE_TOPOCLUSTER_THRES__1up	0.000000%	0.003408%	0.008311%
EG_SCALE_WTOTS1__1down	0.021871%	0.011503%	0.012350%
EG_SCALE_WTOTS1__1up	0.000000%	0.012562%	0.059710%
EG_SCALE_ZEESTAT__1down	0.000000%	0.006685%	0.005840%
EG_SCALE_ZEESTAT__1up	0.005468%	0.006660%	0.003144%
EG_SCALE_ZEESYST__1down	0.010936%	0.029746%	0.037141%
EG_SCALE_ZEESYST__1up	0.032807%	0.029842%	0.055282%

Table D.2: E/gamma scale systematics

Systematic name	Normalisation	Mean	Std Dev
PH_SCALE_CONVFAKERATE__1down	0.000000%	0.007135%	0.009353%
PH_SCALE_CONVFAKERATE__1up	0.005468%	0.007109%	0.007336%
PH_SCALE_CONVRADIUS__1down	0.010936%	0.010018%	0.001370%
PH_SCALE_CONVRADIUS__1up	0.005468%	0.009541%	0.017515%
PH_SCALE_LEAKAGECONV__1down	0.005468%	0.020751%	0.033903%
PH_SCALE_LEAKAGECONV__1up	0.016403%	0.020656%	0.028454%
PH_SCALE_LEAKAGEUNCONV__1down	0.016403%	0.028487%	0.010460%
PH_SCALE_LEAKAGEUNCONV__1up	0.027339%	0.031851%	0.063253%

Table D.3: Photon scale systematics

Systematic name	Normalisation	Mean	Std Dev
TRK_BIAS_D0_WM	0.000000%	0.000000%	0.000000%
TRK_BIAS_QOVERP_SAGITTA_WM	0.000000%	0.000000%	0.000000%
TRK_BIAS_Z0_WM	0.000000%	0.000000%	0.000000%
TRK_EFF_LOOSE_GLOBAL	0.869375%	0.002412%	0.003884%
TRK_EFF_LOOSE_IBL	0.787359%	0.010431%	0.025224%
TRK_EFF_LOOSE_PHYSMODEL	0.475696%	0.001073%	0.021353%
TRK_EFF_LOOSE_PP0	0.142162%	0.002445%	0.001276%
TRK_EFF_TIGHT_GLOBAL	1.356010%	0.004727%	0.024931%
TRK_EFF_TIGHT_IBL	0.929520%	0.009439%	0.007494%
TRK_EFF_TIGHT_PHYSMODEL	0.847504%	0.000909%	0.015814%
TRK_EFF_TIGHT_PP0	0.180436%	0.001894%	0.021038%
TRK_FAKE_RATE_LOOSE	0.054678%	0.001605%	0.026458%
TRK_FAKE_RATE_LOOSE_ROBUST	0.016403%	0.000532%	0.016196%
TRK_FAKE_RATE_TIGHT	0.732681%	0.011144%	0.311736%
TRK_RES_D0_DEAD	0.000000%	0.000000%	0.000000%
TRK_RES_D0_MEAS	0.000000%	0.000000%	0.000000%
TRK_RES_Z0_DEAD	0.000000%	0.000000%	0.000000%
TRK_RES_Z0_MEAS	0.000000%	0.000000%	0.000000%

Table D.4: Track systematics

APPENDIX E

Signal Injection Studies

E.1 Background Model Signal Injection

To investigate any possibility of signal contamination in the GR of the background model, an injection of 500 Higgs signal events into the data sample is used to build the background model. The size of this injection is chosen such that it would be visible in the GR $m_{\pi\pi\pi\gamma}$ distribution, and corresponds to a BR orders of magnitude higher than the SM expected value.

Figure E.1 shows the effect of this signal injection in the GR, as well as for the SR. Given this substantial signal, the effect is negligible on the performance of the background model, and there are no peaks or structures present in the background model after injection.

E.2 Fitting Procedure Signal Injection

In order to test the robustness of the fitting procedure in the context of the $H/Z \rightarrow \omega\gamma$ channel, which provides a novel final state for this fitting procedure compared to previous $H/Z \rightarrow \mathcal{M}\gamma$ analyses, we inject signals corresponding to varying input branching ratios into an Asimov dataset constructed from the expected backgrounds in the SR. The fit is able to accurately return the injected signals, and the results are presented in table E.1.

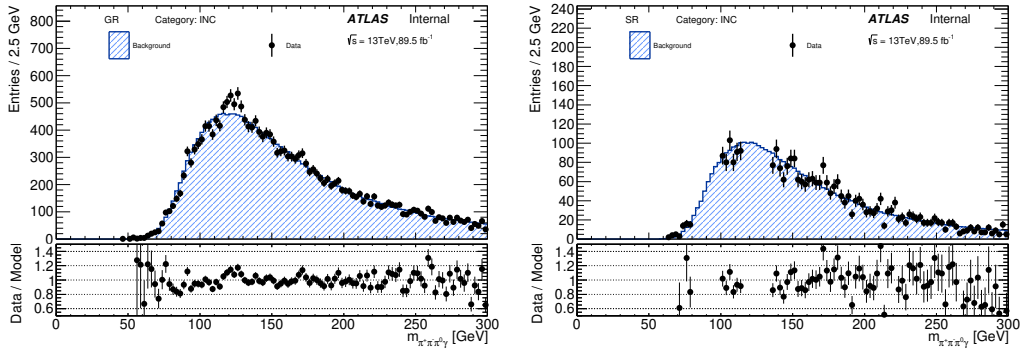

(a) GR (b) SR

Figure E.1: The background model performance after the injection of 500 Higgs signal events in to the data sample used to build the background model.

Branching ratio	Injected μ value	Fit μ value $\pm$ Hesse error	Minos error +	Minos error -
$H \to \omega\gamma$				
5×10^{-5}	50	49.93 $\pm$ 157.0	162.4	-156.2
1×10^{-4}	100	99.95 $\pm$ 157.0	162.4	-156.2
5×10^{-4}	500	499.96 $\pm$ 168.0	174.2	-166.0
1×10^{-3}	1000	999.79 $\pm$ 168.0	174.2	-166.0
5×10^{-3}	5000	4998.9 $\pm$ 190.0	195.2	-169.2
$Z \to \omega\gamma$				
5×10^{-8}	50	50.08 $\pm$ 309.0	314.6	-265.2
1×10^{-7}	100	99.98 $\pm$ 252.0	317.7	-265.1
5×10^{-7}	500	500.02 $\pm$ 262.0	331.3	-276.2
1×10^{-6}	1000	999.82 $\pm$ 262.0	331.3	-276.2
5×10^{-6}	5000	5000.20 $\pm$ 262.0	331.3	-276.2

Table E.1: Signal injection results for the $H/Z \to \omega\gamma$ Asimov fits.